

## University of Southampton Research Repository ePrints Soton

Copyright © and Moral Rights for this thesis are retained by the author and/or other copyright owners. A copy can be downloaded for personal non-commercial research or study, without prior permission or charge. This thesis cannot be reproduced or quoted extensively from without first obtaining permission in writing from the copyright holder/s. The content must not be changed in any way or sold commercially in any format or medium without the formal permission of the copyright holders.

When referring to this work, full bibliographic details including the author, title, awarding institution and date of the thesis must be given e.g.

AUTHOR (year of submission) "Full thesis title", University of Southampton, name of the University School or Department, PhD Thesis, pagination

# **UNIVERSITY OF SOUTHAMPTON**

FACULTY OF PHYSICAL SCIENCES AND ENGINEERING

School of Electronic and Computer Science

**Blood Vessel Shape Description for Detection of Alzheimer's Disease**

by

**Musab Sahrim**

Thesis for the degree of Doctor of Philosophy

December 2014 (Revised January 2016)

Thesis for the degree of Doctor of Philosophy

December 2014 (Revised January 2016)

UNIVERSITY OF SOUTHAMPTON

## **ABSTRACT**

FACULTY OF PHYSICAL SCIENCES AND ENGINEERING

School of Electronics and Computer Science

Doctor of Philosophy

### **BLOOD VESSEL SHAPE DESCRIPTION FOR DETECTION OF ALZHEIMER'S DISEASE**

by Musab Sahrim

Alzheimer's disease (AD) is the most common form of dementia and is characterised by the deposition of aggregated proteins in neurofibrillary tangles or amyloid plaques within the vascular structure of the brain. Amyloid plaques consist of amyloid-beta ( $A\beta$ ) in the extracellular spaces of the brain or in the walls of blood vessels, reflecting a failure to eliminate  $A\beta$  from the ageing brain. The failure to remove  $A\beta$  is potentially reflected in the vessels' shape: vessel shape can improve or reduce fluid flow and thus drainage, according to tortuosity and other shape factors.

Neuropathological studies on post-mortem human tissue have described that the small vessels of aged brains are more tortuous compared to Young brains and tortuosity increases with the presence of Alzheimer pathology[1-4]. There is currently much interest in the diagnosis of AD, especially at the early stages where therapy could be better directed (or even deployed). The central aim of this thesis is to determine whether diagnosis is possible from image data, of brain tissue and MRI scans of the brain. We propose that the capillaries can be analysed as a branching structure, which appears to be a new analysis for medical images. The approach includes new measurements of the branching structure which are enriched by analysis of the vessels' tortuosity and density. The introduction of measures of shape by compactness and Fourier descriptors further enriches this study.

The branching structures are detected by evidence gathering approaches and described by their structure. This allows recognition to be achieved; the structure of those samples derived from patients with AD differs from that for normal subjects. The descriptions

can be classified using machine learning techniques, as such, achieving an automated process from image to recognition. We analysed the structure of the blood vessels in a database of brain tissue images collected from control, age-matched and patients with severe AD. The database comprises five subjects of each of the three types imaged in controlled conditions, and five MRI images of a normal brain from the Brain Tissue Resource of Newcastle UK. We show that by automated image analysis we are able to discriminate between brain tissue samples from patients presenting AD and from the normal samples.

We also show discriminative capability between posterior and anterior regions of the brain imaged in 3D by MRI. The branching structure is the description that is most suited for classification purposes. On this initial dataset, statistically significant differences ( $p=0.04$ ) were seen between anterior and posterior and we can achieve 90% correct classification from a combination of these descriptions.

We are thus confident that these approaches are well suited to further investigation aiming for a diagnostic tool for clinical use in the assessment of possibility of Alzheimer's disease.

# Contents

<b>ABSTRACT.....</b>	<b>ii</b>
<b>Contents .....</b>	<b>iv</b>
<b>List of abbreviation.....</b>	<b>vii</b>
<b>List of tables .....</b>	<b>viii</b>
<b>List of figures .....</b>	<b>ix</b>
<b>Declaration of Authorship .....</b>	<b>xi</b>
<b>Acknowledgements.....</b>	<b>xii</b>
<b>1. Context and Contributions .....</b>	<b>1</b>
1.1 Context.....	1
1.2 Aim and Objectives .....	1
1.3 Contributions .....	3
1.4 Publications.....	4
<b>2. Alzheimer’s disease.....</b>	<b>5</b>
2.1 Basis.....	5
2.2 Diagnosis of Alzheimer’s disease .....	6
2.3 Data acquisition and preparation.....	8
2.3.1 Introduction .....	8
2.3.2 Human Tissue Images .....	9
2.3.3 MRI Imaging .....	11
2.3.4 Pre-processing .....	12
2.3.4.1 Colour Segmentation .....	12
2.3.4.2 Morphology.....	15
2.3.5 Classification.....	18
2.3.5.1 K-Nearest Neighbour .....	18
2.3.5.2 Distance measure .....	18
2.3.6 Cross validation .....	19

2.3.7	Feature Assessment .....	20
<b>3.</b>	<b>Branching Structure.....</b>	<b>21</b>
3.1	Introduction .....	21
3.2	State of the art .....	22
3.3	Model Description .....	24
3.3.1	Branching Point.....	24
3.3.2	The Concept.....	24
3.4	Properties .....	26
3.4.1	Rotation, scale and position invariance .....	26
3.4.2	Model verification for invariance .....	26
3.5	Methodology and Experimentation .....	30
3.5.1	Real World Images .....	30
3.6	Conclusions.....	36
<b>4.</b>	<b>Capillary Structure Analysis .....</b>	<b>37</b>
4.1	Overview.....	37
4.2	Branch Density .....	37
4.2.1	Introduction .....	37
4.2.2	Density .....	37
4.3	Tortuosity.....	38
4.3.1	Introduction .....	38
4.3.2	Extraction of tortuosity from curvature .....	40
4.4	Compactness .....	43
4.5	Planar Fourier Descriptors .....	47
4.6	Analysis of Extracted Features .....	50
4.6.1	Analysis of Density measurement .....	50
4.6.2	Analysis of Tortuosity measurement .....	52
4.6.3	Analysis of Compactness .....	54
4.6.4	Analysis of Fourier Descriptors .....	57
4.7	Results and Discussion .....	59
4.8	Conclusions.....	64

<b>5. MRI Image Analysis.....</b>	<b>66</b>
5.1 Introduction .....	66
5.1.1 Why posterior and anterior? .....	66
5.1.2 Pre-processing .....	67
5.2 3D Model-based Branching Structures.....	71
5.2.1 Angle description .....	71
5.2.2 Model Description .....	73
5.3 3D Feature Detection .....	74
5.3.1 3D Tortuosity .....	74
5.3.2 3D Compactness.....	76
5.3.3 3D Fourier Descriptors .....	78
5.4 Analysis of 3D Features .....	80
5.4.1 Analysis of 3D Model-based Branching Structure .....	80
5.4.2 Analysis of 3D Tortuosity .....	82
5.4.3 Analysis of 3D Compactness .....	83
5.4.4 Analysis of 3D Fourier Descriptor .....	85
5.5 Results and Discussion .....	87
5.6 Conclusion .....	89
<b>6. Conclusions and Future Work.....</b>	<b>90</b>
6.1 Overall Conclusions.....	90
6.2 Future Work.....	93
<b>Appendix A.....</b>	<b>95</b>
Human tissue images.....	95
<b>Appendix B.....</b>	<b>104</b>
MRI montage images .....	104
<b>References.....</b>	<b>109</b>

# List of abbreviation

<b>AD</b>	<b>Alzheimer's disease</b>
<b>Old</b>	<b>Age-matched control</b>
<b>2D</b>	<b>Two Dimensional</b>
<b>3D</b>	<b>Three Dimensional</b>
<b>CCR</b>	<b>Correct Classification Rate</b>
<b>LOOCV</b>	<b>Leave One Out Cross Validation</b>
<b>ANOVA</b>	<b>Analysis of Variance</b>
<b>MRI</b>	<b>Magnetic resonance imaging</b>
<b><i>k</i>-NN</b>	<b><i>k</i> Nearest Neighbours</b>
<b>SFFS</b>	<b>Sequential Floating Forward Selection</b>



# List of tables

Table 3-1 ANOVA table for comparison between Cosine and Degree based Branching Structure .....	31
Table 3-2. Tukey HSD test results for Cosine-based Branching Structure. ....	32
Table 4-1. The measurements of invariants in FDs .....	48
Table 4-2 ANOVA table for analysis of density .....	50
Table 4-3 Multiple comparisons table for Tukey HSD test for density between groups	51
Table 4-4. ANOVA table for various measurement of Tortuosity .....	52
Table 4-5. Tukey HSD Post Hoc test for logT measurement of Tortuosity. ....	53
Table 4-6. ANOVA table for various measurement of Compactness .....	54
Table 4-7. Post Hoc Test for measurements of compactness .....	55
Table 4-8. Contrast coefficients of ANOVA .....	59
Table 4-9. Test of Homogeneity of Variances of all 2D features .....	60
Table 4-10. Results of Contrast Analysis of all 2D features .....	61
Table 4-11. ANOVA table for feature fusion. ....	61
Table 4-12. Post Hoc result using Tukey HSD for feature fusion .....	62
Table 5-1. Result of Independent Sample $t$ -test of different measurement of 3D Branching Structure .....	80
Table 5-2. Result of Independent Sample $t$ -test for 3D Tortuosity .....	82
Table 5-3. Result of Independent Sample $t$ -test of different measurement of 3D Compactness .....	84
Table 5-4 Result of SFFS for Fourier descriptors .....	85

# List of figures

Figure 2-1. Sample images from different categories.....	10
Figure 2-2. RGB images of Young brains .....	13
Figure 2-3. Colour segmentation process using <i>k</i> -means clustering .....	14
Figure 2-4. Thinning Process in sample images.....	17
Figure 3-1. Branching structure .....	21
Figure 3-2. The window used to detect the branching point .....	24
Figure 3-3. Synthetic branching structure for 3 branches .....	25
Figure 3-4. Examples of synthetic branching structure value with rotation invariance ..	27
Figure 3-5. Synthetic branching value with degrees of rotation .....	27
Figure 3-6. Examples of synthetic branching value structure with scale invariant.....	28
Figure 3-7. Synthetic branching value with scaling percentage .....	29
Figure 3-8. Synthetic branching structure value with position invariance .....	29
Figure 3-9. Flowchart for Branching Structure analysis .....	30
Figure 3-10. CCR for different numbers of <i>k</i> .....	33
Figure 3-11. CCR using Cosine-based Branching Structure with different groups .....	34
Figure 3-12. Confusion Matrices of different group combinations for <i>k</i> =1 .....	34
Figure 3-13. Confusion matrices between two groups for <i>k</i> =1 .....	35
Figure 4-1. Normal tortuosity measurement .....	38
Figure 4-2. Extracting branch points.....	41
Figure 4-3. The tortuosity measurement by Equation (4-2).....	41
Figure 4-4. Boundary extraction from binary image .....	42
Figure 4-5. The curvature graph of the object in Figure 4-4 .....	42

Figure 4-6. The variety of objects with their compactness.....	43
Figure 4-7. Comparison between the perimeter and the contact perimeter .....	45
Figure 4-8. Variety of shapes and their contact perimeter .....	46
Figure 4-9. Vessels for FDs analysis.....	47
Figure 4-10. Comparison between classical and discrete compactness by increasing the number of $k$ in $k$ -NN classification technique.....	56
Figure 4-11. CCR using different number of FD coefficient. ....	57
Figure 4-12. CCR using Complex and Elliptic FD .....	58
Figure 4-13. CCR of $k$ for each features between three groups.....	63
Figure 5-1. Example of 3D MRI montage of a normal brain .....	68
Figure 5-2. Comparison between original image and segmented image .....	68
Figure 5-3. 3D view for 3D MRI images.....	69
Figure 5-4. 3D Skeletonisation process in normal brain.....	70
Figure 5-5. 3D Branching Structure for whole brain .....	71
Figure 5-6. Comparison between Azimuth and Elevation angle .....	72
Figure 5-7. Preprocessing of 3D anterior artery .....	74
Figure 5-8. Preprocessing of 3D posterior artery .....	75
Figure 5-9. The understanding of contact surface area.....	77
Figure 5-10. 3D anterior arteries represented as a mesh of 2D triangles.....	78
Figure 5-11. Flowchart of 3D FDs Algorithm .....	79
Figure 5-12. CCR using 3D Branching Structure measures .....	81
Figure 5-13. Recognition of Anterior vs Posterior Vessels by Tortuosity.....	83
Figure 5-14. CCR using 3D compactness measures .....	84
Figure 5-15. CCR using 3D Fourier Descriptor .....	85
Figure 5-16. CCR for different features of 3D .....	87

# Declaration of Authorship

I, Musab Sahrim, declare that this thesis entitled *Blood Vessel Shape Description for Detection of Alzheimer's Disease* and the work presented in it are my own and has been generated by me as the result of my own original research. I confirm that:

1. This work was done wholly or mainly while in candidature for a research degree at this University;
2. Where any part of this thesis has previously been submitted for a degree or any other qualification at this University or any other institution, this has been clearly stated;
3. Where I have consulted the published work of others, this is always clearly attributed;
4. Where I have quoted from the work of others, the source is always given. With the exception of such quotations, this thesis is entirely my own work;
5. I have acknowledged all main sources of help;
6. Where the thesis is based on work done by myself jointly with others, I have made clear exactly what was done by others and what I have contributed myself;
7. Either none of this work has been published before submission, or parts of this work have been published as listed in Section Publications of the thesis:

Signed:.....

Date: .....

# Acknowledgements

First of all, I would like to acknowledge the contributions of all those who helped me throughout this time; firstly to Allah Almighty for giving me this opportunity to explore the new world of research with a new environment and people.

I want to acknowledge my supervisors, Professor Mark S Nixon and Dr Roxanna O Carare for showing confidence in my abilities and encouraging me despite my failures and weaknesses. They continually and convincingly conveyed a spirit of adventure in regard to research and strengthened my passion towards completing this research. Without their guidance and persistent help this thesis would not have been possible.

I would also like to acknowledge my family, particularly my parents, Dr Sahrim Hj Ahmad and Hjh Faridah Hj Ali, my beloved wife, Lily Hanefarezan binti Asbullah, my parents in law, Encik Asbullah bin Ajak, Maimunah binti Hj Omar, Ramnah binti Yahdi and my siblings Khawlah, Sumayyah, 'Ammar, 'Asma and Muhammad who remained extremely supportive and positive regardless of the problems that I experienced.

Finally, I am also grateful to all my friends in the University of Southampton who always assisted me in the best possible way whenever the need arose.

*To my beloved parents, my sweetheart Lily Hanefarezan  
and my siblings*

# 1. Context and Contributions

## 1.1 Context

Alzheimer's disease (AD) is the commonest form of dementia, affecting nearly one million people in the UK and with no effective treatment. Diagnosis is difficult, as many neurodegenerative conditions present with similar features [5]. Amyloid beta ( $A\beta$ ) is a normal product of metabolism, cleaved from an amyloid precursor protein (APP) [6]. Young brains are equipped with different mechanisms to break down and eliminate  $A\beta$ , but, with ageing, and the background of different genotypes, the elimination of  $A\beta$  fails leading to its accumulation and to onset of AD [7]. The accumulation of  $A\beta$  in the walls of the blood vessels of the brain reflects the failure of its elimination along the walls of the blood vessels[8].

In recent years, researchers have tried to detect AD in the human brain using image processing techniques. Most have used MRI and CT scans to detect the abnormalities in the human brain including texture and shape abnormalities. For example, Li detected the shape changes of the corpus callosum in AD [9]. In addition, Freeborough evaluated a texture feature vector to discriminate the AD with the normal brain [10], while Fischl introduced a new method to measure the thickness of the human cerebral cortex by considering the white and the grey matter [11].

## 1.2 Aim and Objectives

Although the methods using computer vision have demonstrated some detection capability, little attention has been given to analysing the abnormalities of specific components in the brain that are affected by  $A\beta$ , such as blood vessels, cells and tissues. The concept of early onset detection of AD has yet to receive more research attention. Naturally, any approach that can detect AD at its onset or early in its progression could be invaluable to medical treatment planning. Many researchers have aimed to extract blood vessels in the fundus of the eye to recognize the possibility of diabetic disease and to try to find the feature of blood vessels that may contribute to the disease. Similarly, the main aim of this research is to develop fully automated framework of an algorithm that could assist the diagnosis of AD for clinicians by determining the structure of the blood vessels that may contribute to the discrimination of images of a brain with AD from those derived from a normal brain. For this purpose, description of a blood vessel through definition of its features is developed, including a novel concept of branching structure and other existing measures such as compactness, Fourier

descriptors, density and tortuosity. These features will be validated using statistical approaches such as ANOVA, *t*-test and contrast and machine learning techniques such as *k*-NN classification and leave-one-out cross validation.

The above aims will be accomplished by fulfilling the following research objectives:

1. To approach the novel concept in definition of a vessel's branching structure as part of feature description.
2. To apply existing techniques that can be used for extracting features for feature description of blood vessels.
3. To develop a 2D-based system using those features for the discrimination of AD brain tissue from age-matched control brain and Young brain tissue and to verify its accuracy and reliability using cross validation, ANOVA and Contrast analysis.
4. To extend the 2D-based feature description to a 3D-based system and to verify its reliability and accuracy using cross validation and independent *t*-test.
5. To perform a comparative study for identifying the most distinguishable features for optimum classification.

In this thesis we test the following hypotheses:

- 1) that the geometrical profiles of small vessels and of the brain change with age and disease profile; and
- 2) the computer visual characteristics of large arteries are different for arteries in the posterior circulation (frequently affected by AD), compared with the anterior circulation.

In order to test the first hypothesis, we used sections of human brains from Young, age matched control and AD brains, where the small blood vessels were imaged after a process named immunocytochemistry that shows the profile of blood vessels. For testing the second hypothesis, images from magnetic-resonance angiograms showing the large arteries of the posterior and the anterior circulation, as well as their branches were used.



## 1.3 Contributions

One novel concept within this thesis concerns the definition of branching structures. Deploying this as a basis was inspired by the branching structures that are common in nature, such as in the path of forked lightning or the roots and branches of trees. To date, there has been little study describing the branching pattern in such structures. It is intuitive that trees differ in their branching structure, and as yet, no mechanism exists to quantify or discriminate between them on the basis of their structure (branching). There appears to be as yet no explicit mention of branching structure analysis in computer vision. As branching structures in brain tissue have yet to be widely studied, it is important to find the abnormalities in the branching structure of AD in human brains for the early detection of AD. Here we demonstrate a new measure as a novel approach for the classification of AD brain images and normal brain images by focusing on the branching structures of the blood vessel within the images. In this study, we define the branching structure of blood vessels by the parameters of angle and branch length, in that we can detect the signs of AD at an earlier stage by focusing on the objects that have been most affected by this disease in early onset detection.

Another contribution concerns the use of density, tortuosity and compactness to analyse the shape of blood vessels. We analyse a discrete measure of compactness that has as yet seen little application in automated image analysis. There are established links between shape and disease and we are the first to study this linkage by using automated image analysis. Our analysis also proposes a deeper understanding of tortuosity than is often available since tortuosity itself is not commonly used in image analysis.

In this study, we also introduce the application of Fourier descriptors for the shape classification of AD. Fourier descriptors are well known for their invariance to rotation, position and scaling. The descriptors are normally used in object retrieval, but in our study we use them as one of the shape features for classification.

Our final area of contribution is to define the posterior and anterior brain vessels by these features. The features are studied in 3D, in MRI-scanned volumetric images. We shall describe how the posterior part of the brain has a connection with the accumulation of  $A\beta$  and thus with AD.

We describe the nature of AD in the next chapter, before we describe the data acquisition and preparation in the next section. In Chapter 3, we address the new measurement for the branching structure. In Chapter 4, we describe analysis of the capillary structure using these features for feature description of vessels for discrimination of AD. In Chapter 5, we address the extension of the features to 3D for classification, showing the performance capability that these new measures can achieve, before conclusions and plans for future work in Chapter 6.

## 1.4 Publications

- 1) Sahrim, Musab, Mark S. Nixon, and Roxana O. Carare. "Analysing morphological patterns of blood vessels for detection of Alzheimer's disease." *IEEE Nuclear Science Symposium and Medical Imaging Conference (NSS/MIC)*, Seoul, South Korea, 27 October – 2 November 2013.
- 2) Sahrim, Musab, Mark S. Nixon, and Roxana O. Carare. "On bloodvessel branching analysis for the detection of Alzheimer's disease." *18<sup>th</sup> Medical Image Understanding and Analysis Conference (MIUA)*, Egham, United Kingdom, 9 – 11 July 2014.
- 3) Sahrim, Musab, Mark S. Nixon, and Roxana O. Carare. "Blood Vessel Feature description for detection of Alzheimer's Disease" *International Conference on Control, Automation, Robotics and Vision (ICARCV)*, Singapore, 10 – 12 December 2014
- 4) Sahrim, Musab, Mark S. Nixon, and Roxana O. Carare. "Describing Blood Vessels by Computer Vision for the detection of Alzheimer's Disease"– In preparation for submission

## 2. Alzheimer's disease

### 2.1 Basis

Alzheimer's disease (AD) is the commonest form of dementia, a disease affecting over 850,000 people in the UK, with no effective cure, no sensitive accurate diagnosis in vivo and posing a huge burden on society [12]. The term 'dementia' defines a set of symptoms that can include loss of memory and other cognitive functions, such as communication and reasoning that affect daily life [13]. In 1906, the disease was first identified and diagnosed by Prof Alois Alzheimer, who was a psychiatrist and neuropathologist, and the disease was named eponymously [14]. AD is characterised by the accumulation of protein 'plaques' and 'tangles' within the structure of the brain, leading to the death of brain cells. In sporadic non-familial AD that represents 95% of all AD cases, these plaques and tangles are a result of the failure of efficient clearance of proteins from the brain and not an overproduction of these proteins. In particular, the plaques appear as a result of the failure of elimination of  $A\beta$ , a normal by-product derived from the Amyloid Precursor Protein (APP) [15].

Accumulation of  $A\beta$  in the brain as plaques and in the walls of blood vessels as Cerebral Amyloid Angiopathy (CAA) is a major feature of AD [16]. The plaques distributed randomly in the brain do not correlate with the degree of dementia and appear in normal ageing. CAA (the accumulation of  $A\beta$  in the walls of capillaries and arteries) does correlate with the degree of dementia and the clinical picture. CAA reflects an age-related failure of the elimination of  $A\beta$  from the brain along perivascular drainage pathways. Solutes similar to  $A\beta$  drain from the extracellular space of the brain along the basement membranes of cerebral capillaries and arteries and  $A\beta$  is deposited in these pathways as CAA in AD[8]. Failure to eliminate  $A\beta$  along the perivascular pathways in CAA coincides with the age-related stiffening of artery walls. Although the cerebrovascular basement membranes are key elements of the perivascular pathways for the elimination of  $A\beta$  from the brain, the changes that occur in association with age and disease are still largely unknown.

## 2.2 Diagnosis of Alzheimer's disease

The most common way to detect AD is by using a neuropsychological test, such as the mini-mental state examination for evaluating cognitive impairment [17]. However, psychiatric examination in early AD will usually provide normal results that show only mild cognitive impairment, and which may not differ from other diseases, including other causes of dementia. Thus, the development of new markers that are sensitive and specific to AD is crucial to differentiate AD from other diseases [18].

Currently, although the neuropsychiatric examination is improving the detection of AD in moderate stages. AD can only be diagnosed with certainty post-mortem, using A $\beta$  or tau protein as markers [19]. A $\beta$  is the major contributor in the discrimination of AD from other diseases. Geert De Meyer *et al.* classified AD patients and normal patients by analysing the cerebrospinal fluid from A $\beta$  with a sensitivity of 94% [20]. The problem with analysing the cerebrospinal fluid is that lumbar puncture for obtaining cerebrospinal fluid is invasive, posing risks to the patient (including infection and headaches) Rusinek *et al.* discovered the possibility of using regional brain atrophy to predict AD with 87% overall accuracy. They suggested that increasing brain atrophy could increase future memory loss [21]. However, an atrophic brain is not specific to AD, as it is a feature of many neurodegenerative diseases, hydrocephalus and other forms of dementia.

More recently, Mapstone *et al.* have suggested that AD can be detected using a blood test [22]. The researchers analysed 126 blood samples from patients over 70 years Old, with 18 of them are detected by 10 lipids (fats) in the blood that could develop AD within two to three years, with 90 percent accuracy. Clearly, to detect AD via a blood test would be extremely convenient. However, fats in the bloodstream vary with diet, ethnicity, and socio-economic status and this signature could be shared with other degenerative brain diseases. There is also evidence that indicates AD is associated with abnormal levels of certain blood biomarkers [23, 24]. As such, the notion that AD can be detected via a blood test appears to need further evaluation and on large datasets.

Computational methods are novel and show promise: the approaches can be grouped into medical image processing and bio-signal processing. Hassainia *et al.* [25] used Significance Probability Mapping (SPM) to quantify and localize Electroencephalography (EEG) in AD. The *t*-statistic mapping was used to highlight

the common changes and z-statistic mapping was used to show the diversity of impairment in an AD brain.

Another method is by using image processing via two types of image – microscopic and macroscopic images. Lawrence *et al.* diagnosed AD patients by calculating the features of pyramidal neurons, dentate neurons and amyloid plaques in the hippocampus [26]. Some time ago now, Bartoo [27] considered detecting and counting the senile plaques using the morphological operation of closing for clustering small objects, with a detection accuracy of 81%. These methods are also assessing changes post-mortem and not in vivo.

Freeborough and Fox evaluated a texture feature vector over MR brain images and succeeded in extracting some features for designing a linear classifier; however, they did not eliminate irrelevant elements, such as texture changes associated with motion artefacts of the images. Their results were also influenced by the large-scale of the image resulting in co-occurrence features being selected in the discriminant function [10].

Another strategy was developed by Zhi-Wen *et al.* by extracting blood vessels using a skeleton feature and shape curve matching [28]. The shape and branching patterns of blood vessels have been correlated with diabetes, hypertension and cancer.

## 2.3 Data acquisition and preparation

### 2.3.1 Introduction

Our analysis involves two main environments, which are human tissue brain images acquired by microscope and human brain 3D volumes acquired by Magnetic Resonance Imaging (MRI). Ethical approval was necessary and obtained for all studies involving humans. Images from post-mortem material were obtained through the Newcastle and Edinburgh Brain Banks and we were dependent on the number of cases received. The 3D images from living subjects were obtained from the Centre for Neurology in Magdeburg, Germany and due to the expensive technique and the risks involved, the number of samples is low. Even though the number of subjects is lower than the average number of subjects required in a standard analysis by computer vision, the number is considered standard in medical research where a pilot study is required first to validate the technique. That is the case for the studies in this thesis.

Furthermore, this pilot study of branching structure description of AD by using a small number of subjects has to be done prior to analysing more subjects to improve the reliability, stability and accuracy of our model and method. To analyse the *in-vivo* characteristics of the large arteries of the brain, a simple magnetic resonance imaging is not sufficient, as this method does not resolve the vasculature. Visualising the cerebral arteries is possible using angiograms and these are invasive, requiring the intravascular injection of a contrast agent. Employing Magnetic resonance angiograms for the brain is relatively recent, with only 87 publications reported in Pub-Med in the period 1990-2015.

Recently, 7 Tesla (7T) MRI has yielded good results for visualizing the cerebral vasculature non-invasively, but this technique is extremely expensive and only available in a few European centers. The number of patients undergoing this technique is usually small, with fewer than 10 patients studied at one time [29]. Through our collaborators in the DZNE Magdeburg (Centre for Study of Neurodegenerative diseases), we have had access to 7T MRI for five patients for this study. As this study is a proof of principle for developing the appropriate computer vision techniques that can be combined with 7T MR-Angiograms, the number of five patients was considered appropriate. Recent studies using patients with cerebral amyloid angiopathy (the feature of AD of interest for this study), employed conventional magnetic resonance imaging with a total number of 24 patients [30]. Over 100 patients are employed in conventional MR studies but not using 7T MRI or 7T MR-Angiograms [31].

### 2.3.2 Human Tissue Images

Slides with human tissue from the Brain Tissue Resource in Newcastle were used, ethical approval number 08/H0906/136 (<http://www.ncl.ac.uk/iah/campus/facilities/nbtr/>). Immunocytochemistry was performed on five sections of brains with AD five age matched controls (Old) and five Young brains. The sections were taken from the frontal and occipital cortices. Tissue sections were blocked in 3% hydrogen peroxide, treated for two minutes at 37°C with pepsin from porcine gastric mucosa (1 mg/mL in 0.2N HCl, Sigma-Aldrich, Dorset, UK), followed by 15% normal goat serum and incubated overnight with anti-collagen IV (1:500, AbCam, Cambridge, UK) antibodies. Sections were washed with PBS, incubated with anti-rat or anti-rabbit horseradish peroxidase conjugates (1:400; Vector Labs, Peterborough, UK) and developed with nickel-enhanced diaminobenzidine as chromogen.

Images were captured at x10 and x20 magnification, using a Nikon Eclipse E600 microscope fitted with a digital camera Nikon Coolpix 950. Images of cortical grey matter were captured in a zig-zag sequence to ensure that all cortical layers were represented in the quantification. The camera resolution allowed capture of images of the size 1600 by 1200 pixels, which corresponded to 0.9 mm<sup>2</sup> of tissue per image.

In Figure 2-1, three samples of images from different categories are shown as an example of description. These groups are:

- a. Elderly subjects who were diagnosed as having AD (AD);
- b. Age-matched elderly subjects not diagnosed as having AD (Old); and
- c. Younger subjects not diagnosed as having AD (Young).

These three groups will be those analysed later.

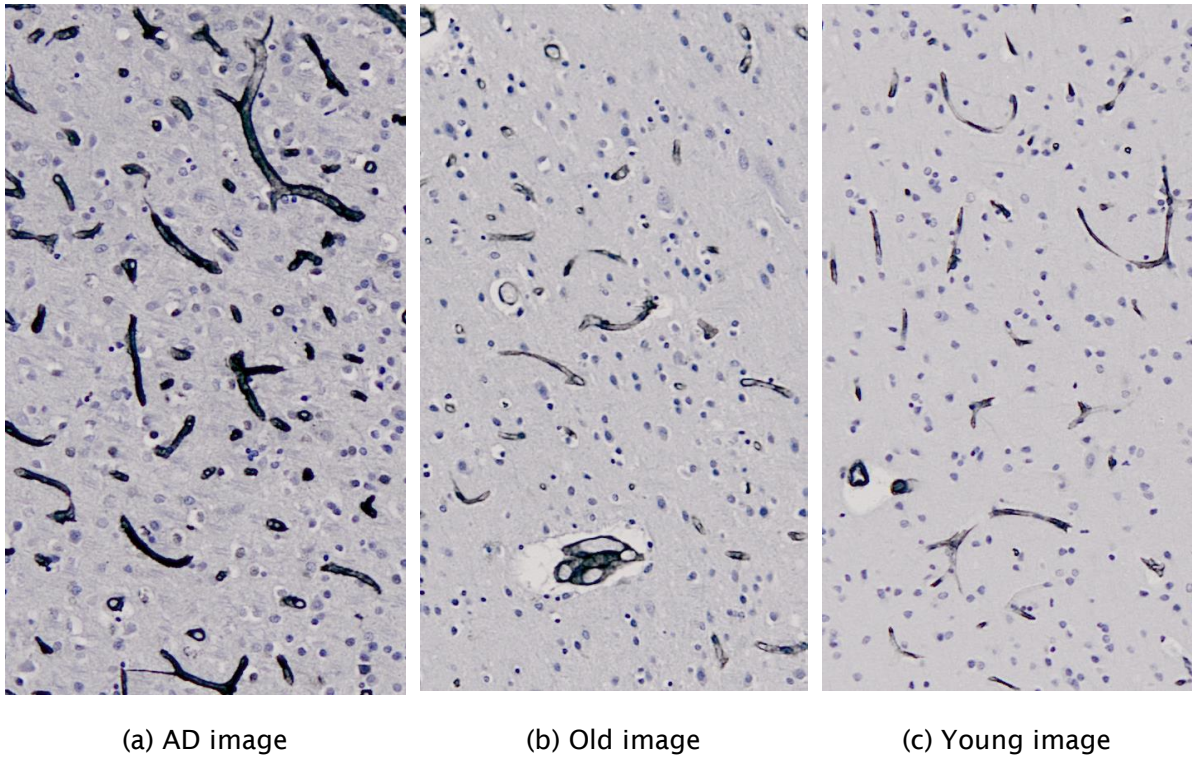


Figure 2-1. Sample images from different categories

Many branches can be seen in the AD sample in Figure 2-1(a) compared to other Old and Young images in Figure 2-1(b-c) and the branches are quite distinguishable from the background by human vision. It is these images that are studied to determine the possibility of automatically determining structures related to the presence of AD, in Chapter 4.



### 2.3.3 MRI Imaging

MRI is a non-invasive technique that provides good soft tissue contrast and is widely available in medical studies. It is used in combination with other imaging modalities, such as Computed Tomography (CT), Positron Emission Tomography (PET) and Magnetic Resonance Spectroscopy (MRS) to provide the most exact information about certain diseases, such as brain tumour, stroke, AD and Multiple Sclerosis. This technology uses a magnetic field and pulses of radio wave energy to acquire the images of the brain that cannot be seen with other imaging modalities, such as X-ray, ultrasound or computed tomography (CT) scans. Contrast dye may be used in some cases to improve the ability to see certain structures.

An MRI scan can lead to early detection and treatment of certain diseases. It can provide a large amount of information quickly, and may reduce the need for diagnostic surgery. Current diagnoses of AD using MRI are considered as a preferred examination made by clinical, neuropsychological and neuroimaging assessments. The evaluation is based on nonspecific features such as atrophy which is considered a late feature in the progression of AD. Fox *et al.* found that the median atrophy was greater in AD compared to the control group [32]. However, the variability of atrophy in the normal aging process makes it difficult to use MRI as the diagnostic technique.

Accumulation of A $\beta$  in the walls of arteries predominantly affects the arteries at the posterior aspect of the brain (vertebrobasilar, or posterior circulation) compared to the arteries at the anterior part of the base of the brain (carotid, or anterior circulation) [33, 34]. Furthermore, in a subset of patients, problems with vision precede any cognitive problems (Young Onset Dementia Assessment, UK) [35]. Vision is processed and represented in the occipital cortex, supplied by the posterior circulation. The exact reasons why the posterior circulation is affected more compared to the anterior circulation are not known. In this project, using magnetic resonance imaging angiograms we address the question whether the characteristics of the arteries of the posterior circulation of normal individuals are different to those of the anterior circulation. If the characteristics differ, we can use the same types of characteristics in people with mild cognitive impairment and/or other risk factors for AD, to assess whether they are at risk of progressing to AD or not.

These images are three dimensional volumes. To study shape, the arteries have been manually segmented from the MRI scans and are presented as binary volumes containing the posterior and anterior cerebral arteries extracted up to the third bifurcation. These are used for 3D assessment of arterial shape, in Chapter 5.

## 2.3.4 Pre-processing

### 2.3.4.1 Colour Segmentation

Improving the discrimination capability of a feature extraction process when colour information is used for pre-processing is based on the fact that the colour contains extra information concerning an object. However, in real situations the colour information always depends on light sources, such as the illumination from a flash camera or an outdoor light. In addition, it is important to define colour perception in terms of psychophysical dimensions, such as chromaticity, purity or brightness. As such, the detection of the branches will be parallel to the perception of the specialist. Thus, in order to be able to extract the objects that are the branches for feature extraction, we introduced a pre-processing technique by using CIELAB clustering-based pre-processing, implemented using the CIELAB colour space, which is robust to the changes in illumination and chrominance.

Different from any colour space like RGB and XYZ, CIELAB has the capability to tolerate illumination changes and has the capability to match human perception. CIELAB allows the description of colour perception as a three-dimensional space. This includes the  $L^*$  axis, which is known as the lightness and extends from 0 (black) to 100 (white), and the other two coordinates,  $a^*$  and  $b^*$ , represent redness-greenness and yellowness-blueness, respectively. Samples for which  $a^* = b^* = 0$  are achromatic and thus the  $L^*$  axis represents the achromatic scale of grey from black to white. Therefore, by eliminating the  $L^*$  axis, we can use the other two coordinates for the segmentation of branches. In the microscopic images analysed here, the blood vessels (represented by branches), the cells (represented by blobs) and the background are visually separated by colour. Therefore, a new means to derive the blood vessels is achieved by combining the two axes  $a^*$  and  $b^*$  and  $k$ -means clustering. Clustering is chosen given its ability to gather the information into distinct groups by specifying the number of clusters and a distance metric (which quantifies how close two objects are to each other [36]).

The first stage in segmenting the branches in medical images is the conversion of the RGB images to CIELAB (also known as  $L^*a^*b^*$ ) colour space [37] as shown in Figure 2-3(a-b). We can segment an image by grouping them with separation by colour, by ignoring the brightness (luminosity). Since the colour information only exists in the ' $a^*b^*$ ' space, the objects are pixels with ' $a^*$ ' and ' $b^*$ ' values. We use the  $k$ -means algorithm to cluster the objects into three clusters using the Euclidean distance metric. For every object in an input image,  $k$ -means returns an index corresponding to a cluster. The image can be segmented by these index values into various segments or clusters.

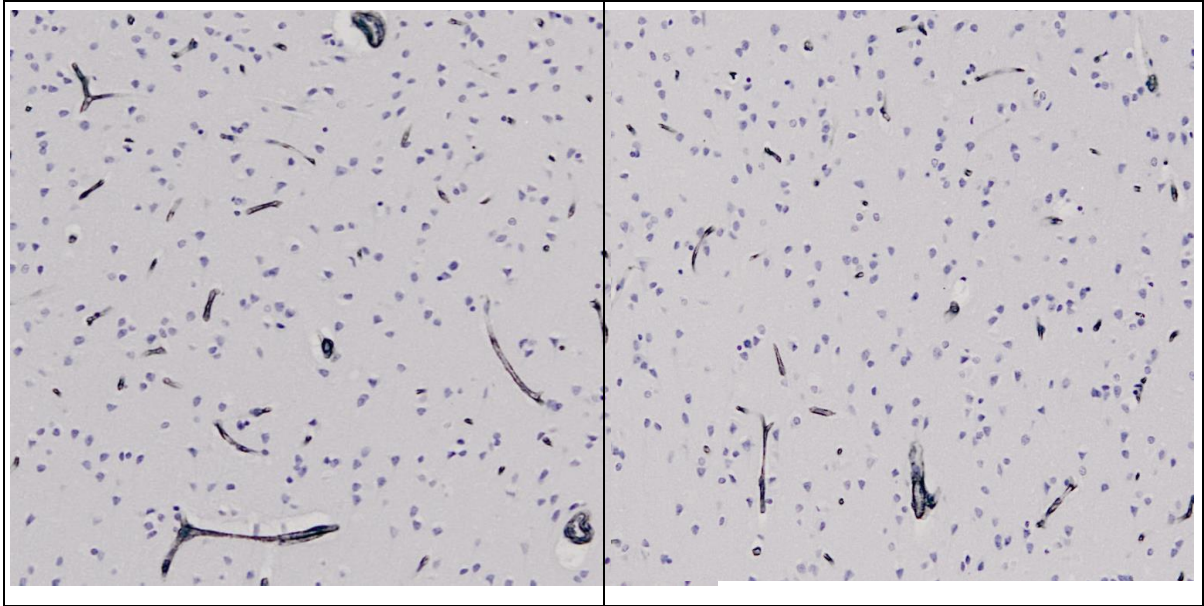


Figure 2-2. RGB images of Young brains

As we can see in the images Figure 2-2, there are three components in this image – the blood vessel branches (represented by the branches), the cells (represented by blobs) and the background. By defining them into three classes, we specify  $k=3$  as  $k$ -means clustering requires the number of clusters to be partitioned using the Euclidean distance metric as it can be directly related to the computation of the cluster means [36]. Since the use of the Euclidean distance as a uniform measure assumes that the colour space is isotropic, the clusters defined by this distance will be invariant to translations and rotations [38].

Every pixel is labelled in the images using the cluster index from  $k$ -means analysis. Using pixel labels, the objects in the brain will be separated by colour, which result in three images, as Fig 2b-d shown are objects in cluster 1, objects in cluster 2 and the final segmentation.

By experimental analysis, we conclude that the blobs have the highest mean value since the blobs are brighter than the background and the branches. For this reason, we find the mean of each cluster images to obtain the values of the three images. We then sort the mean value of 3 clusters of images and choose the brightest one which is the cluster with blobs as shown in Figure 2-3(c).

Then the clustered image containing only the blobs will be converted into a binary image for purpose of masking as shown in Figure 2-3(d). Addition will be used to overlay the output on top of the original image after suitable masking has been carried out (Figure 2-3(e)). As depicted in Figure 2-3(f), after the morphology have been done, finally the image has been turned into a connected set of binary sets that can be used for analysis in the next chapter. The same processes are applied to each of the 15 2D images used in this study.

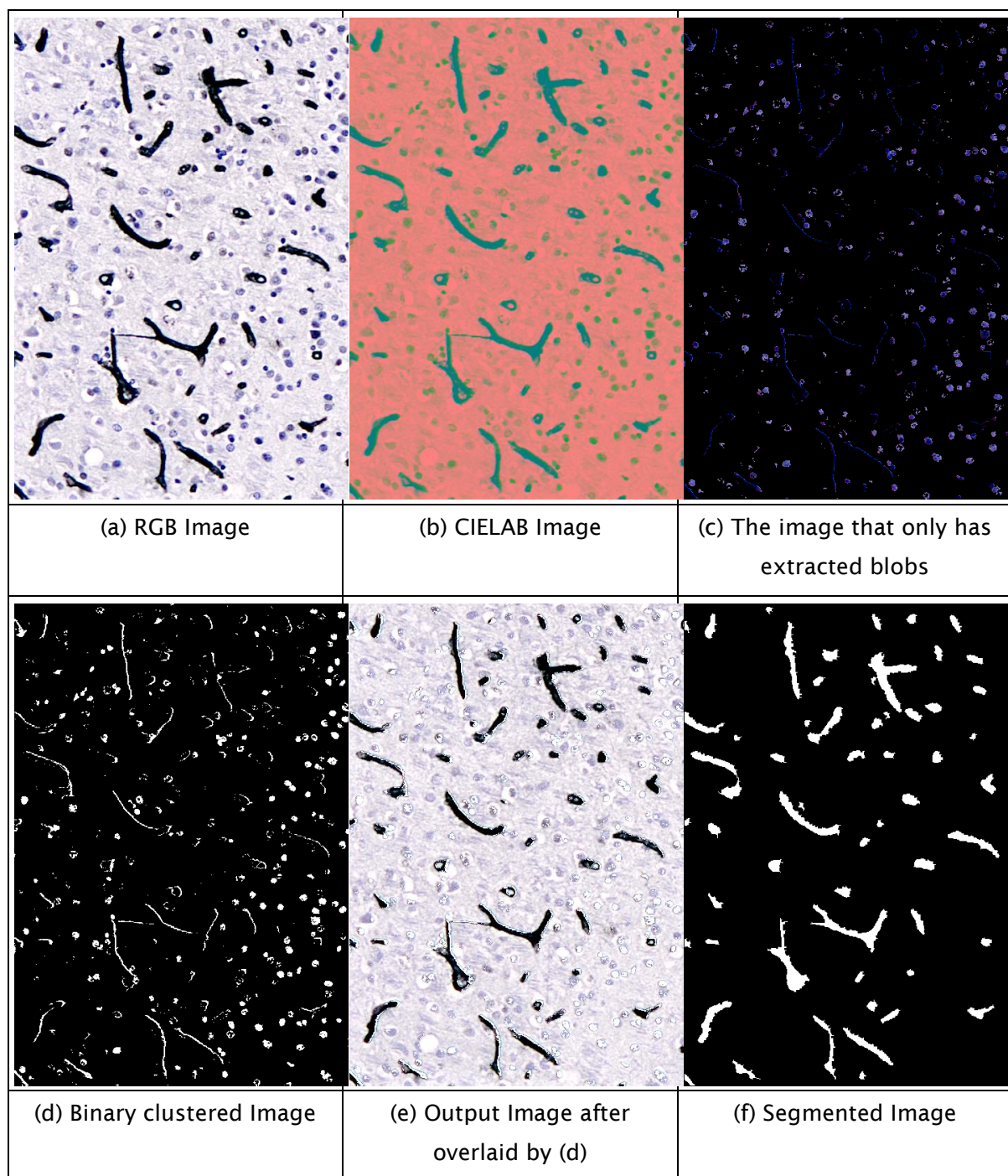


Figure 2-3. Colour segmentation process using  $k$ -means clustering

### 2.3.4.2 Morphology

Morphology operations derive from ‘Morphing’ in biology, which means ‘changing a shape’[39]. Thus, morphology is the part of bioscience dealing with the study of the form and structure of a creature and their specific structural features. Furthermore, specific aspects of the outward appearance like shape, structure, colour and pattern are studied. Encouraged by that, Morphology has been used in mathematics for the analysis and processing of geometrical structures. It was introduced by G.Matheron and J.Serra in 1964. At that time, mathematical morphology was developed for binary images.

In general, mathematical morphology uses a structuring element as a probe to an input image, creating an output image of the same size. It is tool for investigating geometric structures in images using the language of set theory. In Mathematical Morphology, the basic operators are related to Minkowski addition and subtraction, which is defined by:

$$X \oplus T = \{a + b: a \in X, b \in T\} = \bigcup_{b \in T} X_b \quad (2-1)$$

and:

$$X \ominus T = (X^c \oplus T)^c = \bigcap_{b \in T} X_b \quad (2-2)$$

Using this method, we can simplify image data by preserving essential shape characteristics and eliminating noise. It can also be used to recognise and extract the underlying shape and reconstruct it from its distorted and noisy form.

The primary morphological operations that implement Minkowski addition and subtraction are dilation and erosion. More complicated morphological operators can be derived by combining erosion and dilation techniques. Usually, dilation is used to enlarge and expand and enlarge the boundaries of regions around the foreground pixels, and erosion is used to reduce and delete the foreground pixels.

In this section, we will only discuss three parts of mathematical morphology, as these will be applied in this project. These are dilation, erosion and thinning.

## Dilation

Dilation is an operation that combines two sets using vector addition of set elements [40]. Let A and B be subsets in 2-D space. A: image undergoing analysis, B: Structuring element,  $\oplus$  denotes dilation:

$$A \oplus B = \{c \in Z^2 \mid c = a + b \text{ for some } a \in A, b \in B\} \quad (2-3)$$

Let A be a Subset of  $Z^2$  and  $x \in Z^2$ . The translation of A by x is defined as:

$$(A)_x = \{c \in Z^2 \mid c = a + x, \text{ for some } a \in A\} \quad (2-4)$$

The dilation of A by B can be computed as the union of translation of A by the elements of B:

$$A \oplus B = \bigcup_{b \in B} (A)_b = \bigcup_{a \in A} (B)_a \quad (2-5)$$

The dilation operation is commutative, associative and translation invariant, and, therefore, a suitable operator for our purposes.

## Erosion

Erosion is the morphological dual to dilation. It combines two sets of dilation using the vector subtraction [40]. To understand the definition of erosion, let us say that erosion A by B is defined by denoting  $A \ominus B$ . So:

$$A \ominus B = \{x \in Z^2 \mid \text{for every } b \in B, \text{ there exists an } a \in A \text{ such that } x = a - b\} \quad (2-6)$$

Erosion can be expanded for use in many ways by expressing it in different forms. Erosion can also be defined in terms of translation:

$$A \ominus B = \{x \in Z^2 \mid (B)_x \subseteq A\} \quad (2-7)$$

In terms of intersection;

$$A \ominus B = \bigcap_{b \in B} (A)_{-b} \quad (2-8)$$

Erosion has always been used to shrink the object to remove noise in the binary image.

## Thinning Algorithm

The thinning or skeletonisation algorithm is a process that shrinks an object into a skeleton. It is one of the morphological operations that is used to remove selected foreground pixels from binary images. It preserves the topology (extent and connectivity) of the original region while discarding most of the original foreground pixels. Figure 2-4 shows the results of a thinning operation on a simple binary image.

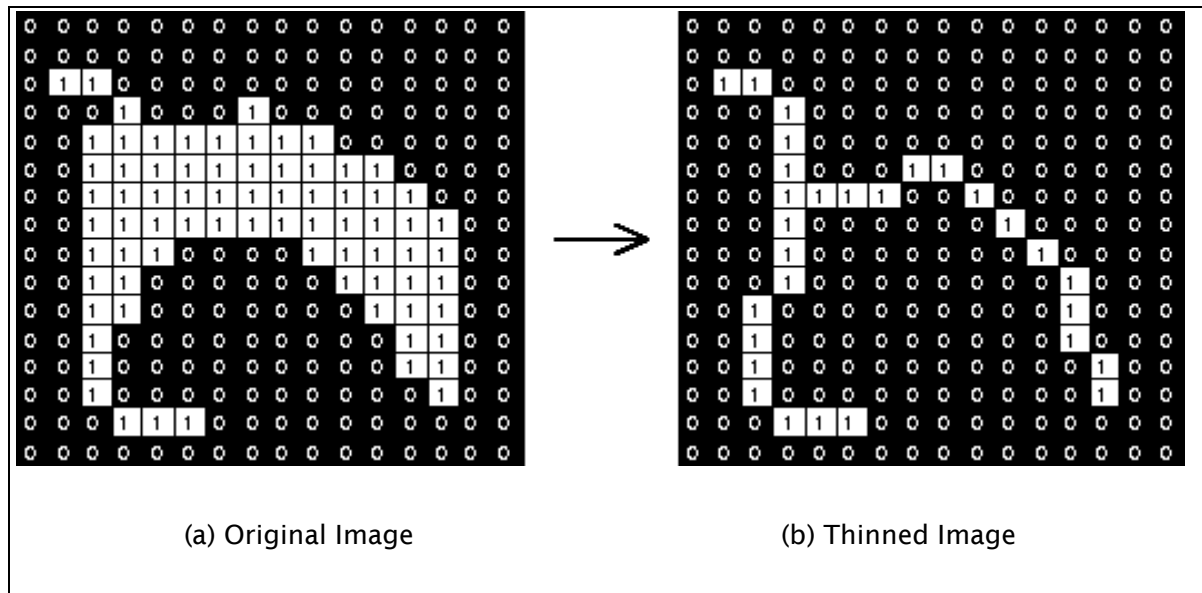


Figure 2-4. Thinning Process in sample images.

Like other morphological operators, thinning operators take two pieces of data as input. One is the input image, which may be either binary or greyscale. The other is the structuring element, which determines the precise details of the effect of the operator on the image[41].

In skeletonisation, there are two basic methods for extracting the skeleton of the image: using medial axis transform or a thinning algorithm. While the medial axis transform uses the distance transformation for skeletonisation, the thinning algorithm iteratively deletes the border points of an object satisfying topological and geometrical limitations until a smaller set of connected points is obtained. Due to the instability of the medial axis transform, we are only using the thinning algorithm for this process.

### 2.3.5 Classification

We shall later describe techniques that can be used to derive feature vectors that describe the capillary structures within these images. One analysis is the new study of branching structures, and another is the use of established shape measures. These provide feature vectors that are used with  $k$  Nearest Neighbour analysis which we shall describe here as the approaches are routine in computer vision.

#### 2.3.5.1 K-Nearest Neighbour

We use the  $k$  Nearest Neighbour ( $k$ -NN) approach for classification and choose the value of  $k$  in the range 1 to 5 to encompass the whole data set. We deploy feature selection to choose the best tortuosity features. For this, we chose Sequential Floating Forward Selection (SFFS) as a standard and proven approach. For validation one can use either internal validation where the model is validated on the current data set or external validation where the model is validated on a completely new dataset. We employ Leave-One-Out Cross Validation (LOOCV) for maximal use of the available dataset.

#### 2.3.5.2 Distance measure

The Mahalanobis distance is a measure used to obtain a distance between clusters, where the measure reflects not only the cluster spacing but also the cluster spread. On the other hand, the Euclidean distance between the means will remain the same whatever the cluster spread because it only measures distance between the centres of mass and not the spread. The Mahalanobis distance includes the variance and is therefore a more perceptive measure of distance.

The Mahalanobis distance is calculated as:

$$d_{MAH} = \sqrt{(p - \mu)^T \Sigma (p - \mu)} \quad (2-9)$$

Where the data samples  $\mathbf{p}_i = (\mathbf{m}_{1i}, \mathbf{m}_{2i}, \mathbf{m}_{3i} \dots, \mathbf{m}_{Ni})^T$ , have mean values  $\mu = (\mu_1, \mu_2, \mu_3, \dots, \mu_N)^T$  and a covariance matrix  $\Sigma$  which is formed of elements that express the variance as:

$$\Sigma_{ij} = E[(\mathbf{p}_i - \mu_i)(\mathbf{p}_j - \mu_j)] \quad (2-10)$$



This way, the distance is scaled by the variance. Therefore, the distance measure reflects the distributions of the data, which are ignored in the Euclidean distance formulation. The formulation does rather depend on the structure used for the data.

### **2.3.6 Cross validation**

Validation should be done in order to evaluate the classifier's performance by reducing errors on the training data. Errors are not a good indicator of the performance on data as new data will probably not be exactly the same as the training data. Furthermore, overfitting will occur when the fitting of the training data is too precise and will cause poor results on the new data.

There are two ways to perform the validation:

- 1) Internal Validation: to validate a model on the current data set (cross validation); and
- 2) External Validation: to validate a model on a completely new dataset.

For eliminating the effect of overfitting, Cross Validation is introduced[42]. Cross Validation is a machine learning method of evaluation by dividing data into two classes: one is used to train a model and the other is used to validate the model. In typical cross validation, the training and validation sets must be exchanged in successive rounds so that each data point has a chance of being validated again.

#### **Holdout Validation**

Holdout Validation is a way to validate the model by fitting the model on half of the dataset as the training set and testing it on the remaining half of the dataset. The test data is held out and not looked at during training. Holdout validation avoids the overlap between training data and test data, producing more accurate results. The disadvantage of this method is that half of the data is not being utilised, compromising volume.

#### **K-Fold Cross Validation**

In  $k$ -fold cross-validation, the data is first partitioned into  $k$  sized segments or folds. Consequently,  $k$  iterations of training and validation are performed, such that within each iteration a different fold of the data is held-out for validation while the remaining  $k-1$  folds are used for training. Often the subsets are stratified before the cross validation is performed. The true errors are estimated from the average error rate.

## Leave-one-out Cross Validation (LOOCV)

LOOCV is a special case of  $k$ -fold cross-validation where  $k$  equals the number of instances in the data. For each iteration, nearly all the data except for a single observation are used for training and the model is tested on that single observation. An estimated accuracy obtained using LOOCV is known to be almost unbiased but has high variance, leading to an unreliable estimate. Nevertheless, it is still widely used for its reliability to solve the problem of overfitting as the available data are very rare, especially when only dozens of data samples are available. In this thesis we employ LOOCV accuracy for performance evaluation referred to as Correct Classification Rate (CCR).

### 2.3.7 Feature Assessment

One of the methods to assess the features is to use hypothesis testing such as  $t$ -test or ANOVA which can be performed using statistical package such as SPSS Statistics [43]. By assessing the features, we can choose the best feature to be used for classification. Liu *et al.* has recorded great accuracy improvement in their classification algorithms by first determining discriminatory features using statistical approaches such as chi squared and  $t$ -statistic[44]. A hypothesis test such as the  $t$ -test has been used for identifying protein markers in tumour[45]. In pattern recognition, ANOVA is used as one of the methods for feature selection [46, 47].

By running the test according to normality of the data, we can obtain the  $p$ -value that indicates the significant differences between classes. For example we could use independent sample  $t$ -test for measuring the significance test between two class groups and ANOVA for multiple class groups. These assessments are valuable to select and evaluate which features are good for classification. If the  $p$ -value is smaller than a previously selected threshold value, we could interpret that by using this feature all the groups are significantly different. Traditionally the threshold values (called significance levels) of the test are chosen as 0.1, 0.05 and 0.01. The null hypothesis is defined as a general statement or default position that there is no significant difference in features between classes. As the  $p$ -value is smaller than the significance level (in this analysis we choose the significance level as 0.1), we can reject the null hypothesis and we could define that there is difference of features between classes.

Furthermore, the Contrast analysis and the Post Hoc test are useful for deeper analysis. The contrast analysis or planned test is used to answer specific questions regarding the hypothesis. The Post Hoc test or unplanned test is a test used after ANOVA to explore the differences between the means and to provide specific information on which means are significant different from each other.

## 3. Branching Structure

### 3.1 Introduction

Branching patterns can be seen all around us, from tree branches, brain, sea fans to blood vessels (Figure 3-1). They are often nature's preferred method of growth for many organisms because they spread out to cover a large area smoothly and efficiently. For example, the branched structure of the tree allows the leaves to obtain an even and plentiful amount of sunlight whilst also giving it a strong, firm construction. The branching of blood vessels allows the body to pump blood to all areas of the body quickly and evenly. Despite their separate domains, they still produce what appear to human vision to be similar branching structures. However, regardless of the recurrence of this structure in multiple species and level of organization, we do not clearly know how these structures form and evolve, nor how to differentiate them in terms of their branching structure.

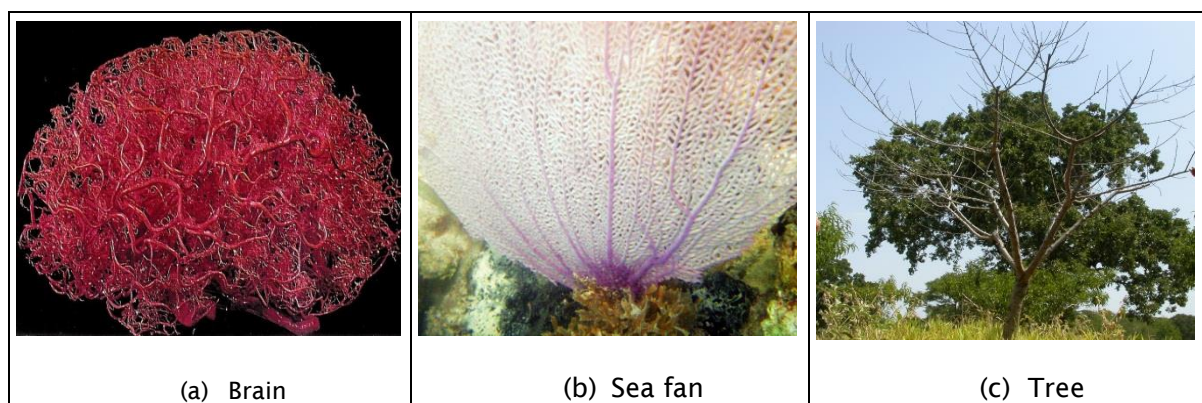


Figure 3-1. Branching structure

We describe a new approach to explore the pattern of the branching structure in blood vessels, focussing on the brain vessels. This is because branching structures evolve, grow and form to survive and adapt within an environment that can change due to instability of the health system in the brain or the body itself. For example, a disease like diabetes which occurs in the brain can putatively affect the branching structure in the retina. Alternatively, irregularity of the branching structure could disrupt the system in the normal brain, affecting blood flow and might create a variety of diseases like AD and Downs syndrome. Goldberger explained that fractal anatomic structures may show degradation in their branching structure, such as loss of dendritic arbor in aging cortical neurons and vascular “pruning” in primary pulmonary hypertension [48]. Thus, development of an algorithm to detect the branching structure for

feature description may be a novel approach towards the recognition of AD in its early stages and help medical practitioners and researchers find the best solution.

### 3.2 State of the art

Blood vessels have previously been analysed in the diagnosis of diabetes, hypertension, cancer and atherosclerosis [49]. In recent years, detecting abnormalities of the blood vessels has been an important marker for early detection or progression of disease. For example, the arterioles, capillaries and venules have been found to be irregular in their shape, and unusual in their tortuosity and with abnormal hierarchical arrangement in blood vessels affected by tumors [50]. Peter *et al.* mentioned that angiogenesis (the formation of new blood vessels) is a distinctive feature to detect a tumor. As such, angiogenesis is stimulated by hypoxia in asthma, diabetes and AD which are triggered by the extracellular matrix or vascular congestion damaging the supply of oxygen [51]. In particular, on the subject of AD, Berislav suggested a need for neurovascular repair in AD as there is a strong connection between cognitive decline in AD and cerebrovascular disorder. It is explained by the reduced density of the microvascular structure, and a higher number of fragmented vessels with less intact branches. AD is also characterised by highly irregular capillary surfaces and marked changes of vessel diameter [52]. There is also evidence that the efficiency of the drainage of A $\beta$  depends on different parts of the brain [53] and the accumulation of A $\beta$  appears more in the posterior circulation (derived from the vertebral arteries) compared to the anterior circulation (derived from carotid arteries).

Current approaches to analysing branching structure can be divided into non-medical and medical approaches. In non-medical images, the branching structure has been used as a new feature in biometrics for security purposes. Vein structure is used as a feature for hand authentication utilising the structural similarity by using Delaunay triangulation [54]. In medical approaches, there are many analyses of blood vessels in the detection of structural abnormalities. Diego *et al.* evaluated the angiostatic activity based on topological and fractal parameters[55]. Hashizume measured manually the abnormalities of the tumour vessels by their leakiness, which is described as consistent with increasing vessel size [56]. Patients with Barrett's Oesophagus (BE) present vascular abnormality which is detected by investigations based on correlation with histology [57]. Stanton *et al.* have discovered that the bifurcation angles in the retina are lower with hypertensives

than normal and the angles decline further with increasing age [58]. Kiani *et al.* found that the capillary density increases when the mean angle of bifurcation increases [59]. Elizabeth *et al.* classified tumours as benign or malignant on the basis of vessel tortuosity [60].

Given that previous researchers have found many features that could be indicators to help diagnosis, this research will focus on individual branches rather than on a region structure [61, 62] by finding the relationship of branching vessels and bifurcation angle. This measure could then be used as one of the features to detect the abnormalities in AD. This is the first approach to use branching structure analysis of blood vessels, especially in relation to detection of AD. If successful this could lead to a more detailed investigation.

### 3.3 Model Description

#### 3.3.1 Branching Point

In a manner similar to Calvo *et al.* [63], a potential branching point obtained from a measure  $I(V)$  is calculated for each point  $V$  of the output of the thinning operator where  $N_i(V)$  are the neighbours of the analysed point  $V$ , named clockwise consecutively, as in Figure 3-2. First, the number of points connected to  $V$  is counted as  $I(V)$  in Equation (3-1),

$$I(V) = \frac{1}{2} \left( \sum_{i=1}^8 |N_i(V) - N_{(i+1) \bmod 8}(V)| \right) \quad (3-1)$$

$N_1$	$N_2$	$N_3$
$N_8$	$V$	$N_4$
$N_7$	$N_6$	$N_5$

Figure 3-2. The window used to detect the branching point

If the measure  $I(V)$  calculated in Equation (3-1) exceeds two then the point  $V$  is classified as a branching point  $I_{bp}$  as described in Equation (3-2).

$$I_{bp} = \begin{cases} 1 & I(V) > 2 \\ 0 & otherwise \end{cases} \quad (3-2)$$

#### 3.3.2 The Concept

A basic branching structure has three branches and can be described by a combination of the length of the branches and the angle between them.

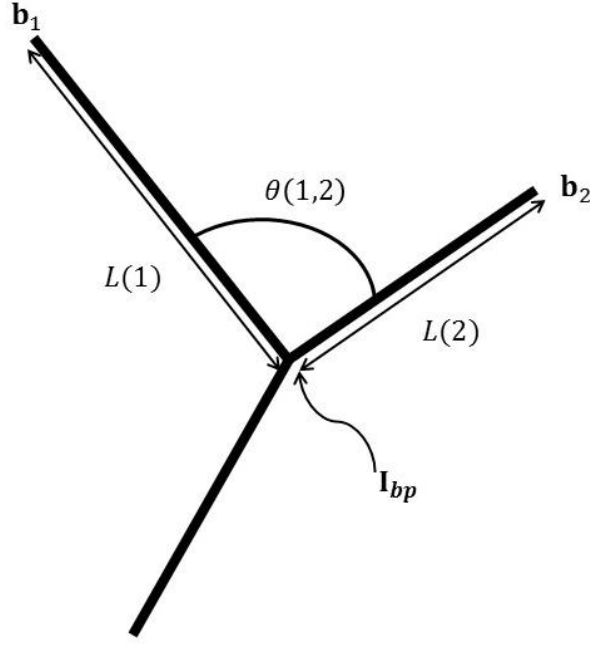


Figure 3-3. Synthetic branching structure for 3 branches

Essentially, we have segments of blood vessels that are at different inclinations to the branching point. For a branching point  $B$  with  $N$  branches each of length  $L(n)$ , the branching structure, as shown in Figure 3-3, can be described by a composite measure, which is derived from the branch length and the relative inclination of the vessels. The average vector product of pairs of branches and the angle between them, gives the measure  $B_{cos}$ , as

$$B_{cos} = \frac{\sum_{i=1, N, j=1, N} [L(i) + L(j)] \times \cos(\theta(i, j))}{\sum_N L_N} \quad i \neq j \quad (3-3)$$

In the results section, this is termed the Cosine-based Branching Structure. There might be alternative descriptions and this is a natural starting point as it offers a description of any branching structure and one that fits with usual computer vision objectives. The basis can be extended to networks of branching points; its description can be extended to more branches than three. As this equation appears to favour smaller angles, a version without the cosine function was also deployed,  $B_\theta$  in Equation (3-4). In the results section, this is termed the Degree-based Branching Structure.

$$B_\theta = \frac{\sum_{i=1, N, j=1, N} [L(i) + L(j)] \times \theta(i, j)}{\sum_N L_N} \quad i \neq j \quad (3-4)$$

## 3.4 Properties

### 3.4.1 Rotation, scale and position invariance

Feature descriptions should have robustness (invariance) so that their descriptions do not vary with change in conditions. Every object model should have the same value for any condition, such as when rotated, transformed (translated) or scaled. For rotation, this model should be robust to any overall orientation of the branches. Thus, the value of branching structure is not affected by measurements of branch length and angle in a rotated version. The model should also be position invariant, as every value of the branching structure is the same for every position of the branches. As the zoom factor of the images is not usually fixed, the model should offer scale invariance, as the description should not change by the zooming factor. In this way, this model can adapt automatically to the unknown scale variations that may occur because of objects and substructures of varying physical size as well as objects with varying distances to the camera [64]. Accordingly, this measure was formulated to ensure the description is invariant to rotation, scale and position. The formula contains the normalised length of the branches, hence it will be scale invariant and because it also involves the angle between two branches, it is rotation-invariant. It is also position invariant and mandates that the branching point has to be detected in a pre-processing stage.

### 3.4.2 Model verification for invariance

Our method has been tested using a synthetic image containing branches in several conditions to demonstrate it is rotation, scale and position invariant. Firstly, for rotation-invariance, the whole shape is rotated by 0 to 360 degrees. Then, the length is changed from ratios of 10% to 400% of an original size to verify that our method is scale-invariant. Finally, the branching structure is moved to different positions to analyse position-invariance.



### Rotation Invariant Verification

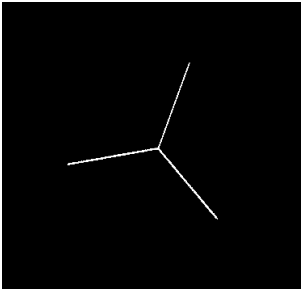
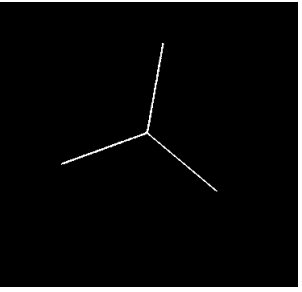
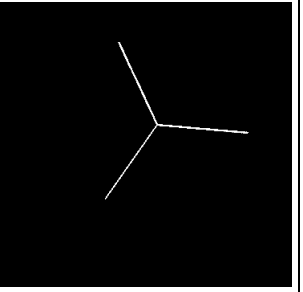
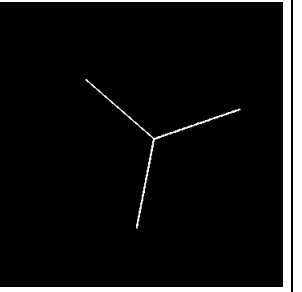
			
$B_{cos} = 1$ Degree=20°	$B_{cos} = 1$ Degree=130°	$B_{cos} = 1$ Degree=215°	$B_{cos} = 1$ Degree=311°

Figure 3-4. Examples of synthetic branching structure value with rotation invariance

In the first experiment, the branching structure model is shown to have rotation invariance by using synthetic images with degrees of rotation from 0° to 360°. As the examples in Figure 3-4 show, the same values of  $B_{cos}$  are obtained for all the objects hence the measure appears to be to rotation invariant. The graph in Figure 3-5 concludes the experimental analysis showing the measure  $B_{cos}$  versus the amount of rotation.

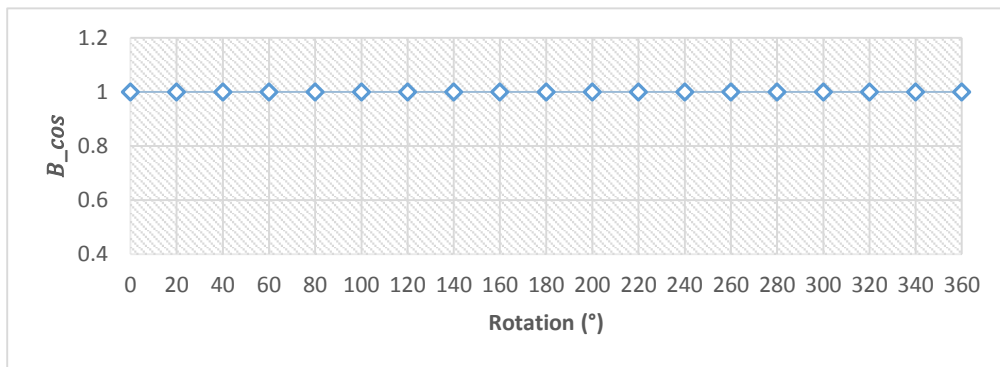


Figure 3-5. Synthetic branching value with degrees of rotation

### Scale Invariant Verification

In order to justify that the model is invariant to scaling, a mathematical proof for theoretical justification together with synthetic image analysis for experimental justification have been performed. The scale invariant ( $n \times \text{scale}$ ) will be substituted into Equation (3-4) and will be justified as in Equation (3-5), and the result shows that the measure remains unchanged. This analysis applies to both the Cosine- and the Degree-based Branching Structures.

$$\begin{aligned}
 & \frac{[(L_i + L_j) \times \cos \theta_{i,j}] + [(L_j + L_k) \times \cos \theta_{j,k}] + [(L_k + L_i) \times \cos \theta_{k,i}]}{\sum L_N} \\
 &= \frac{[(nL_i + nL_j) \times \cos \theta_{i,j}] + [(nL_j + nL_k) \times \cos \theta_{j,k}] + [(nL_k + nL_i) \times \cos \theta_{k,i}]}{n \sum L_N} \\
 &= \frac{[n(L_i + L_j) \times \cos \theta_{i,j}] + [n(L_j + L_k) \times \cos \theta_{j,k}] + [n(L_k + L_i) \times \cos \theta_{k,i}]}{n \sum L_N} \\
 &= \frac{n\{[(L_i + L_j) \times \cos \theta_{i,j}] + [(L_j + L_k) \times \cos \theta_{j,k}] + [(L_k + L_i) \times \cos \theta_{k,i}]\}}{n \sum L_N} \\
 &= \frac{[(L_i + L_j) \times \cos \theta_{i,j}] + [(L_j + L_k) \times \cos \theta_{j,k}] + [(L_k + L_i) \times \cos \theta_{k,i}]}{\sum L_N}
 \end{aligned} \tag{3-5}$$

Next, the experimental proof will use synthetic images and scale factors from 10% to 400%. As the examples in Figure 3-6 show that the same values are obtained for each object ( $B_{cos} = 1$ ) for all scales, hence the measure appears to be scale invariant. The graph in Figure 3-7 concludes the experimental analysis, showing the feature values versus scaling percentage.

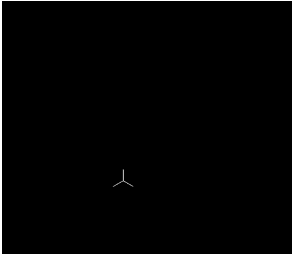
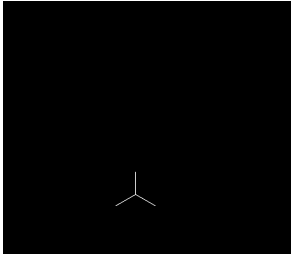
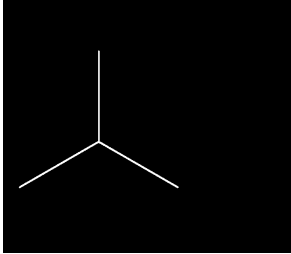
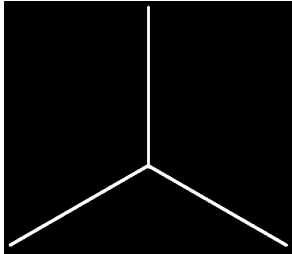
			
$B_{cos} = 1$ Scale Factor= 0.25	$B_{cos} = 1$ Scale Factor = 0.5	$B_{cos} = 1$ Scale Factor = 2	$B_{cos} = 1$ Scale Factor = 3.5

Figure 3-6. Examples of synthetic branching value structure with scale invariant

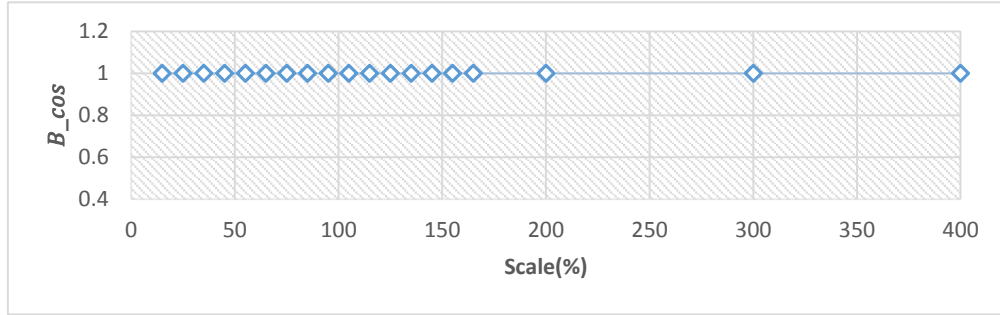


Figure 3-7. Synthetic branching value with scaling percentage

### Position Invariant Verification

Finally, we test this measurement for position invariance. From the results shown in Figure 3-8, our model tested on the synthetic image is confirmed to be position invariant as the same value of  $B_{cos} = 1$  is obtained for all positions. Thus for the summary, our model appears, by the synthetic images to be rotation, scaling and position invariant as in Figure 3-4, Figure 3-6 and Figure 3-8 show the consistency of the branching structure value with 0% error rate. Furthermore, this technique could find shapes reliably and robustly, irrespective of the value of any parameter that can control the appearance of a shape.

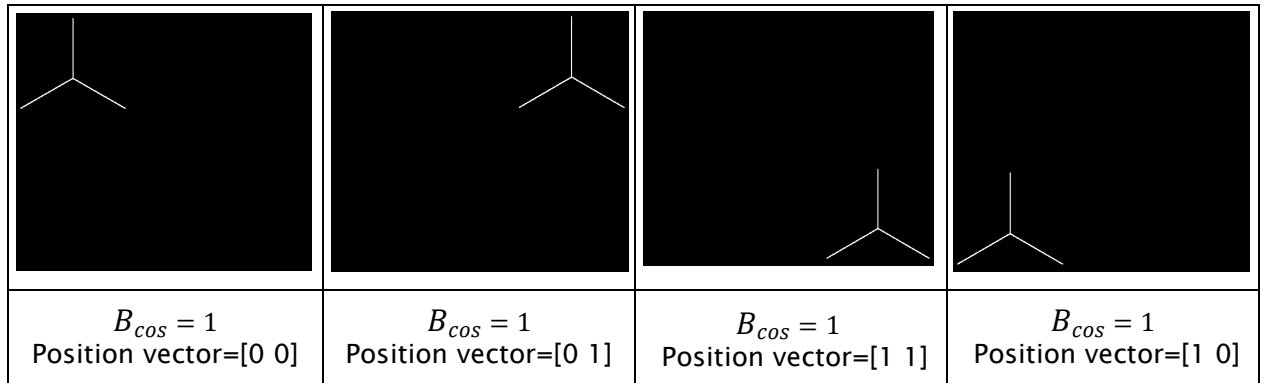


Figure 3-8. Synthetic branching structure value with position invariance

## 3.5 Methodology and Experimentation

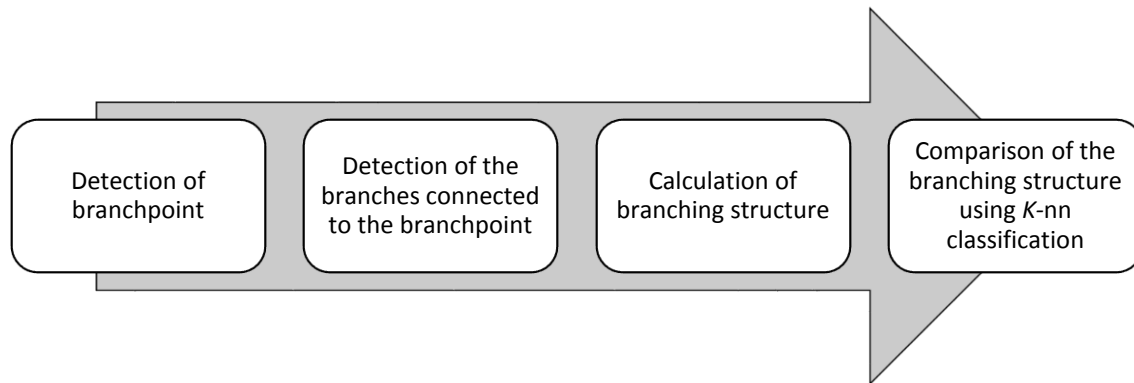


Figure 3-9. Flowchart for Branching Structure analysis

We will analyse the branching structure by first detecting the branch point and the branches of the blood vessels. Then the branching structure will be measured using Equations **Error! Reference source not found.** and (3-4). The results of the branching structure will be classified using *k*-NN classification. This algorithm is shown in Figure 3-9. We will test this model on real world images.

### 3.5.1 Real World Images

Based on the previous section, this next experiment was conducted to translate this measurement to real-world images especially to analyse the images of subjects' brain samples. Five images of brains from each of the three groups, AD, Old and Young images are segmented by pre-processing and then each segmented image had to undergo the morphological operation, thinning, to extract the branches. These thinned-extracted branches that are associated with branching points are separated and labelled for the following process. In real-world images, the branches are not straight, therefore, the angle cannot be determined. Thus, polynomial fitting is required to determine the angle between the branches. The algorithm is applied to the branches to find their linear position (best fitting straight line by least squares) in the images and then the branching structures are calculated.

Every branching structure will be defined as having three legs with their angles ( $\theta$ ) between them (total 3 angles). The branch length ( $L$ ) and angles ( $\theta$ ) will then be used as variables in Equation (3-5). There are multiple branching structures in each image: the maximum number of branching points is 77 and the minimum is 10. The extracted measures for every images will be averaged and named as Branching Structure and will be assessed using ANOVA and Tukey HSD as multiple comparison to analyse statistical significance, and then will be classified using  $k$ -NN classification technique. The CCR for  $k$ -NN will be obtained using LOOCV.

		ANOVA				
		Sum of Squares	df	Mean Square	F	Sig.
Cosine-based	Between Groups	.134	2	.067	3.225	.076
	Within Groups	.249	12	.021		
	Total	.383	14			
Degree-based	Between Groups	.001	2	.000	.556	.587
	Within Groups	.007	12	.001		
	Total	.008	14			

Table 3-1 ANOVA table for comparison between Cosine and Degree based Branching Structure

In order to find which branching measure is most suitable for our feature description of AD, Cosine-based and Degree-based branching structures are examined using ANOVA for significance testing and their comparison is shown in Table 3-1. ANOVA was conducted to explore the impact of branching structure of different groups (Old, Young and AD). There is a statistically significant difference at the  $p < 0.1$  level in Branching Structure using the Cosine based method for the three groups [ $F(2, 12) = 3.22, p = 0.076$ ].

The results of Cosine-based Branching Structure provided clear evidence to support the claim that there are some differences in the feature extracted among the group means. Under the null hypothesis the Branching Structures for all groups are the same. However, contrary to the cosine-based measure, ANOVA shows no significant differences for degree-based branching structure at the significant level of 0.1 [ $F(2, 12) = 0.556, p = 0.587$ ]. Thus, the three groups are indistinguishable using the Degree-based Branching Structure feature on the basis of the obtained data.

## Post Hoc Tests

### Multiple Comparisons

Tukey HSD

(I) Grouping	(J) Grouping	Mean Difference (I-J)	Std. Error	Sig.	90% Confidence Interval	
					Lower Bound	Upper Bound
Old	Young	-.1337	.0911	.3402	-.3401	.0728
	Alzheimer's Disease	-.2304*	.0911	.0637	-.4368	-.0240
Young	Old	.1337	.0911	.3402	-.0728	.3401
	Alzheimer's Disease	-.0968	.0911	.5542	-.3032	.1097
Alzheimer's Disease	Old	.2304*	.0911	.0637	.0240	.4368
	Young	.0968	.0911	.5542	-.1097	.3032

\*. The mean difference is significant at the 0.10 level.

Table 3-2. Tukey HSD test results for Cosine-based Branching Structure.

Post Hoc analysis is done to measure the difference among the means after ANOVA. In this analysis, the Tukey test is chosen as the groups have the same sample size. From the results shown in Table 3-2, there is no evidence that the means for the Young data are statistically different from those of the Old and the AD data, and there is evidence that the means of the Old and the Young are statistically different. In the other words, by using only this Branching Structure feature, we could only differentiate AD from Old. A further and alternative feature is needed to differentiate between Young and AD and between Young and Old. This also means that the angle and branching length that are associated with the branching structure algorithm both contribute to differentiating AD from Old.

The data from the Branching Structures are then classified using  $k$ -NN classification to investigate their capabilities for classification. Leave-one out cross validation is used to measure the CCR and the result is shown in Figure 3-10. It is evident from the results that overall, there were higher CCRs for Cosine-based Branching Structure compared to Degree-based Branching Structure, as expected from the previous statistical analysis.

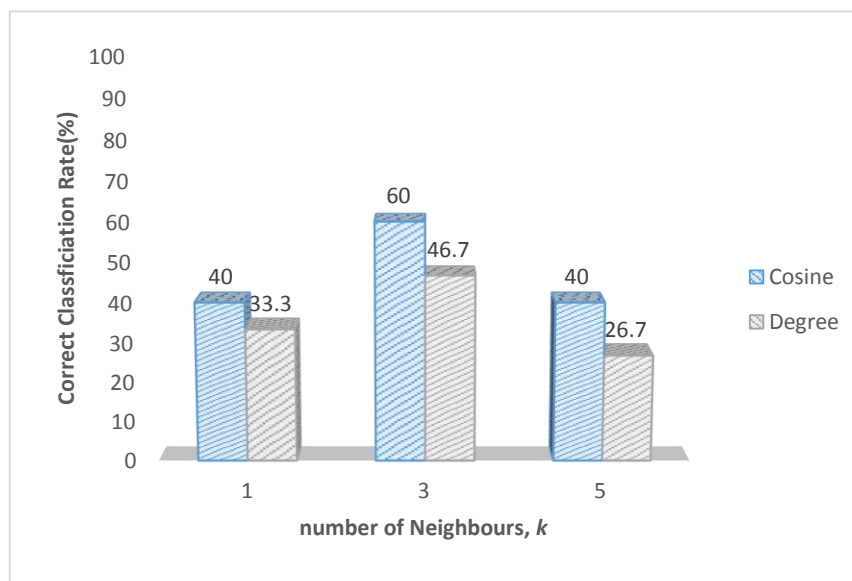


Figure 3-10. CCR for different numbers of  $k$

We extend our investigation into different comparison of AD vs Old, AD vs Young and Old vs Young to see which comparison will have high classification capabilities. Clearly, as proved in multiple comparison in Table 3-2, the comparison between AD vs Old are highest from other comparisons (70% for  $k=1$  and 5, 60% for  $k=3$ ) as shown in Figure 3-11. Conversely, the comparison between Old and Young are the lowest of all comparisons. The comparison between AD and Young in the other hand has CCR of 70% for  $k=1$  but drops to 10% for  $k=5$ .

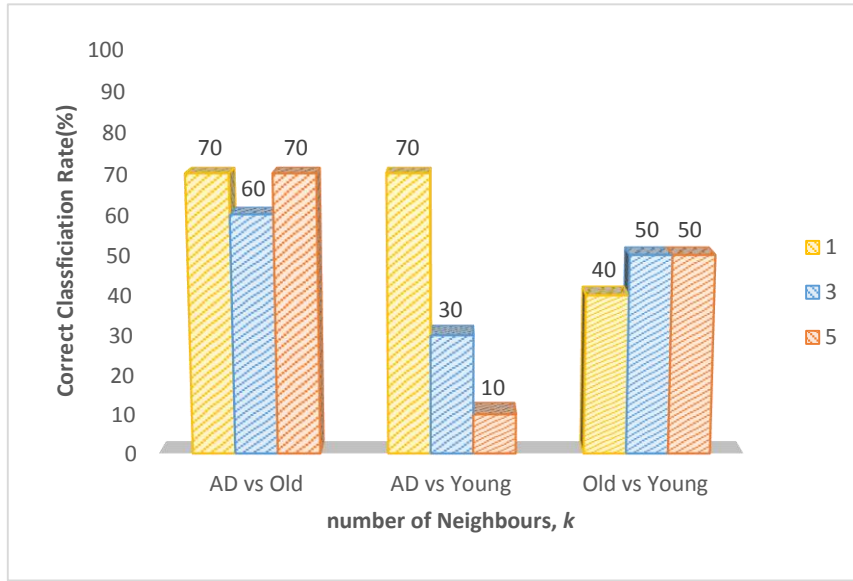


Figure 3-11. CCR using Cosine-based Branching Structure with different groups

Finally, confusion matrices for all the combinations are generated as shown in Figure 3-12 and Figure 3-13. Confusion matrices between AD, Old and Young are compared using cosine-based branching structure and degree-based Branching Structure are shown Figure 3-12(a) and Figure 3-12(b). The true positive rate for the Cosine-based Branching Structure are 60% CCR which is higher than for the Degree based Branching Structure which obtained only 20%. The precision for AD is by the Cosine measure is also higher than by the Degree measure, with 60% compared to 16.7% CCR.

		Target Class			
		AD	Old	Young	
Output Class	AD	3 20.0%	1 6.7%	1 6.7%	60.0% 40.0%
	Old	1 6.7%	1 6.7%	2 13.3%	25.0% 75.0%
	Young	1 6.7%	3 20.0%	2 13.3%	33.3% 66.7%
		60.0% 40.0%	20.0% 80.0%	40.0% 60.0%	40.0% 60.0%
(a) Confusion Matrix of Cosine Branching Structure					
		Target Class			
		AD	Old	Young	
Output Class	AD	1 6.7%	2 13.3%	3 20.0%	16.7% 83.3%
	Old	2 13.3%	3 20.0%	1 6.7%	50.0% 50.0%
	Young	2 13.3%	0 0.0%	1 6.7%	33.3% 66.7%
		20.0% 80.0%	60.0% 40.0%	20.0% 80.0%	33.3% 66.7%
(b) Confusion Matrix of Degree Branching Structure					

Figure 3-12. Confusion Matrices of different group combinations for  $k=1$



The precision between AD vs Old is 75% and higher than other combination as for the AD vs Young. However the recall for AD vs Young is 80% and higher than the other combination (AD vs Old=60% and Old vs Young=20%).

		Target Class		
		AD	Old	
Output Class	AD	3 30.0%	1 10.0%	75.0% 25.0%
	Old	2 20.0%	4 40.0%	66.7% 33.3%
		60.0% 40.0%	80.0% 20.0%	70.0% 30.0%
(a) Confusion Matrix of Cosine Branching Structure for AD vs Old				

		Target Class		
		AD	Young	
Output Class	AD	4 40.0%	2 20.0%	66.7% 33.3%
	Young	1 10.0%	3 30.0%	75.0% 25.0%
		80.0% 20.0%	60.0% 40.0%	70.0% 30.0%
(c) Confusion Matrix of Cosine Branching Structure for AD vs Young				

		Target Class		
		Old	Young	
Output Class	Old	1 10.0%	2 20.0%	33.3% 66.7%
	Young	4 40.0%	3 30.0%	42.9% 57.1%
		20.0% 80.0%	60.0% 40.0%	40.0% 60.0%
(c) Confusion Matrix of Cosine Branching Structure for Old vs Young				

Figure 3-13. Confusion matrices between two groups for  $k=1$

### 3.6 Conclusions

The branching structure model has shown the capability to differentiate the samples with AD (from Old subjects) from the samples derived from the Young subjects. This model that depends on angle and branch length of the branches is improved by using cosine-based branching structure description which shows a lower  $p$ -value compared with a degree-based branching measure which fails to reject the null hypothesis and the feature was not statistically significant. Higher CCR of 40% were achieved compared to degree-based branching structure measure which could only reach 33.3% CCR.

Interestingly, when images from AD subjects are compared between Young and Old, a higher classification rate is achieved (CCR=70%) compared with analysis between Old vs Young, even though when using statistical method only Old can has significant difference from the subjects with AD. This model has limitations, as it is just the initial stage of developing the algorithm and offers a basic description. Nonetheless, clearly the results show that this model has sufficient performance to justify extension into a three-dimensional environment such as CT, PET or MRI for the reason that in 2D environment, the branching structures are limited to the slices of the brain and do not describe the whole brain. The analysis of branching structures could also be extended by including diameter, density and known measurements that could improve the classification rate as well as increasing the sample size. Deeper analysis could also be done such as feature fusion to improve the reliability and robustness by focusing on the bifurcation ratio.

With the new establishment of this model, we then analyse other well-known features such as tortuosity, FDs, compactness and new description of branching density to find the capability for feature description of AD in the following chapter. The following chapter concludes by combining the branching structure model with other features in order to find better classification rate and higher differentiation capabilities of AD with other subjects, showing that analysis of the branching structure can indeed contribute to the diagnosis of AD.

## 4. Capillary Structure Analysis

### 4.1 Overview

The main focus of this thesis is to find the features that might lead to the analysis and description of the capillary (branching) structure. Thus, in this context this chapter focuses on the deployment of established feature description approaches for the detection of AD in capillary structures using microscopic images. Therefore, we try to find the interplay of these features: density of the branches and their tortuosity, capillary compactness and planar FDs. We then use these features to classify brain images from subjects with AD against two other groups – Young and Old brains.

### 4.2 Branch Density

#### 4.2.1 Introduction

Initially, the formation of new vessels called angiogenesis that has been discussed in previous chapter could be a contributor to differentiate AD from other subjects. Thus, in order to find the correlation between angiogenesis and AD, the density by counting the number of branches in the image is analysed. Moreover, in order to obtain the number of branches, we pre-process the image to obtain a binary version and then convert vessels into their skeletons. Then, we seek to find the branching points so as to determine the intersections between them (should they occur).

#### 4.2.2 Density

After obtaining the branching points  $I_{bp}$ , they are then excluded when counting the number of branches  $N_{branches}$  in the image. This was implemented by setting the branching points to black, the same value as for the background image. This resulted in an image containing only branches with no branching points, and the branches were labelled for counting as in Equation (4-1).

$$N_{branches} = \sum (I_{vessel} \cap \overline{I_{bp}}) \quad (4-1)$$

## 4.3 Tortuosity

### 4.3.1 Introduction

Studies have discovered that vessel tortuosity is related to many diseases, such as diabetes, hypertension and peripheral arterial disease [65]. Tortuosity can be defined as the property of a curve that has been twisted. It has been used in the images of eye fundus to determine symptoms of diabetes and hypertension. For example, an increase in blood pressure causes an increase in a vessel's tortuosity [66].

The quantitative measurement for tortuosity was discovered by Lotmar, Freiburghaus and Bracher [67]. Tortuosity  $\tau$  is described as an arc-chord ratio:

$$\tau = \frac{L}{C} \quad (4-2)$$

where  $L$  is the length of the curve and  $C$  is the distance between the ends of the curve. Figure 4-1 illustrates the measurement they used to calculate the vessel's tortuosity.

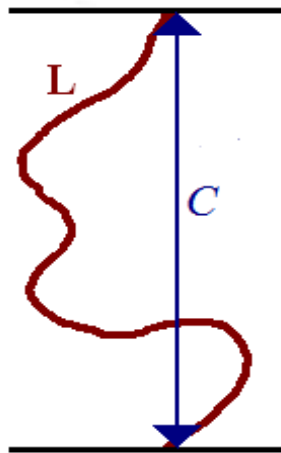


Figure 4-1. Normal tortuosity measurement

Another alternative method to define the shape is curvature. It is a very important boundary feature for humans to judge similarity between shapes. It also has prominent perceptual characteristics and has proven to be very useful for shape recognition. Curvature can be considered as the rate of change in edge direction. This rate of change characterises the points in a curve; points where the edge direction changes rapidly are corners, whereas points where there is a little change in edge direction correspond to a straight line.

Such extreme points are very useful for shape recognition, and therefore can be used to define the shape tortuosity, since they represent significant information to define the measure. Nixon (2012) described the curvature  $\kappa$  as the changes in the direction  $\varphi(t)$  with respect to the changes in arc length [37]:

$$\kappa(t) = d\varphi(t)/ds \quad (4-3)$$

where  $s$  is arc length, which represents the edge itself and  $\varphi$  is the angle of the tangent to the curve:

$$\varphi(t) = \tan^{-1}(\dot{y}(t)/\dot{x}(t)) \quad (4-4)$$

Since a curve parameterised by the arc length maintains a constant speed of motion, curvature represents changes in direction for constant displacement along the curve. Nixon applied the chain rule to derive the curvature as:

$$\kappa(t) = \frac{d\varphi(t)}{dt} \frac{dt}{ds} \quad (4-5)$$

As the differential  $ds/dt$  defines the change in arc length with respect to the parameter  $t$ , the curve can be considered as the motion of point described by:

$$ds/dt = |\dot{v}(t)| = \sqrt{\dot{y}^2(t) + \dot{x}^2(t)} \quad (4-6)$$

and:

$$dt/ds = 1/\sqrt{\dot{y}^2(t) + \dot{x}^2(t)} \quad (4-7)$$

By considering the equation above, the curvature  $\kappa$  at the point  $\dot{v}(t)$  is given by:

$$\kappa(t) = \frac{\dot{x}(t)\ddot{y}(t) - y(t)\ddot{x}(t)}{[\dot{y}^2(t) + \dot{x}^2(t)]^{3/2}} \quad (4-8)$$

The calculation of the curvature-based tortuosity is based on Equation (4-8).

### 4.3.2 Extraction of tortuosity from curvature

We introduce a measurement of tortuosity based on the curvature that is shown to be an alternative feature for measuring the tortuosity. For example, Martin proposed the analogy of riding a bicycle or driving a car in a trajectory with a constant curvature [68]. He considered that it is harder to drive on trajectories with a curvature that changes. He suggested that tortuosity could be measured by the relative change of curvature and proposed a local measure, which is a derivative of the logarithm of curvature, given by:

$$\tau = \frac{d}{dt} \log \kappa \quad (4-9)$$

where  $t$  is an index to a curve's exterior boundary. In another method, Smedby *et al.* [69] evaluated five measurements of tortuosity applied in femoral arteries. Included are several measures of vessel fraction that have high curvature and the integral curvature along the blood vessel:

$$\tau = \int_{t_0}^{t_1} |\kappa(t)| dt \quad (4-10)$$

Where  $t_n$  represents boundary points on the curve. In this thesis, we have developed another curvature-based tortuosity measured by implementing the average bending energy published by Young [70], given by:

$$\tau = BE = \frac{1}{N} \sum_{t=0}^{N-1} \kappa(t)^2 \quad (4-11)$$

where  $BE$  is the average bending energy of a point on a contour containing  $N$  points. In this study, we compare these three calculations of tortuosity based on curvature with the standard approach of tortuosity, aiming to find the best measure of tortuosity.

## Framework of Tortuosity

The figure below shows the branching points using the approach in Section 3.3.1; the branch points are then labelled and counted. The branch points themselves (shown in Figure 4-2) are not used within the calculation of number of branches and its tortuosity.

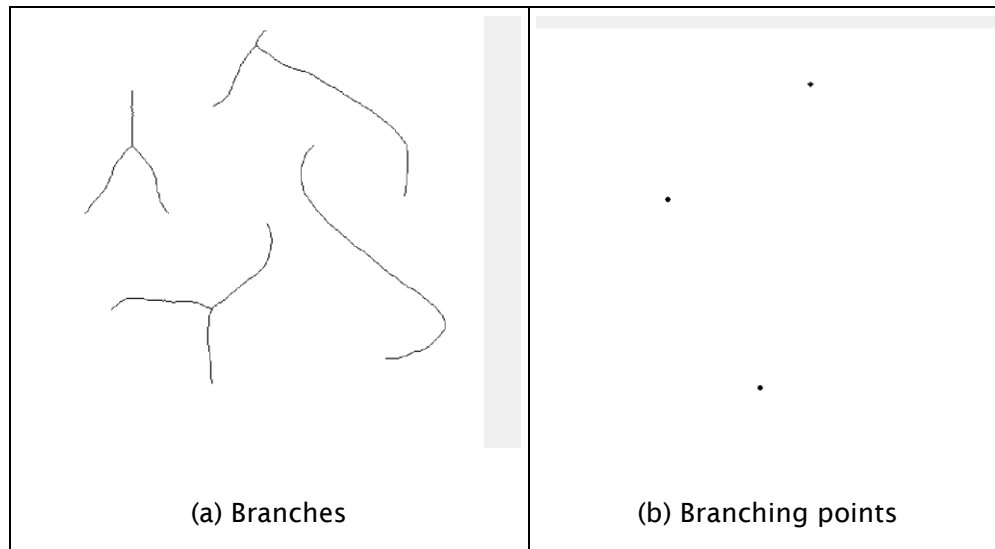


Figure 4-2. Extracting branch points

After obtaining the number of branches, the tortuosity of branches is derived as in Equation (4-2). Figure 4-3(a) shows the path length of each branch and Figure 4-3(b) shows its tortuosity. The mean tortuosity of branches then describes the overall structure within the image.

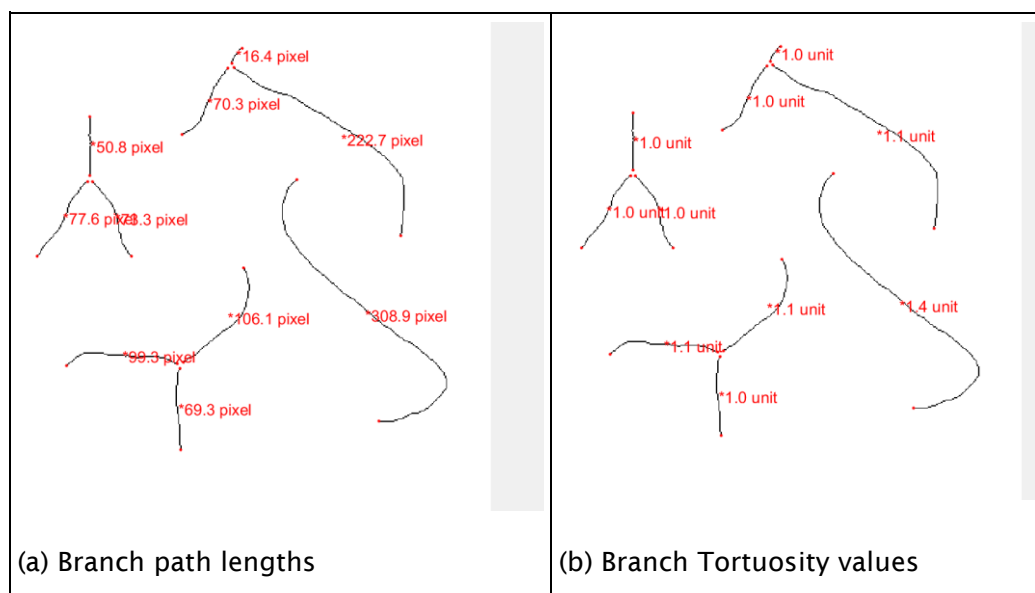


Figure 4-3. The tortuosity measurement by Equation (4-2)

For curvature-based tortuosity, we first find the boundary of the image using the boundary function that implements the Moore-Neighbor tracing algorithm modified by Jacob's stopping criteria [71]. This function is based on the boundaries function presented by Gonzalez [39]. Then we apply the calculation of curvature in Equation (4-8) to the extracted boundary. Subsequently, the tortuosity measures described in Equation (4-9), (4-10) and (4-11) are then applied to this curvature value and the classification rate is calculated. The best measure of tortuosity is described in the next chapter. For validation, we use the image in Figure 4-4 to ensure that the calculation is correct. The boundary graph in Figure 4-4(b) and the curvature of the boundary is shown in Figure 4-5. In this graph, there appear two peaks which refer to the curvature extrema in Figure 4-4.

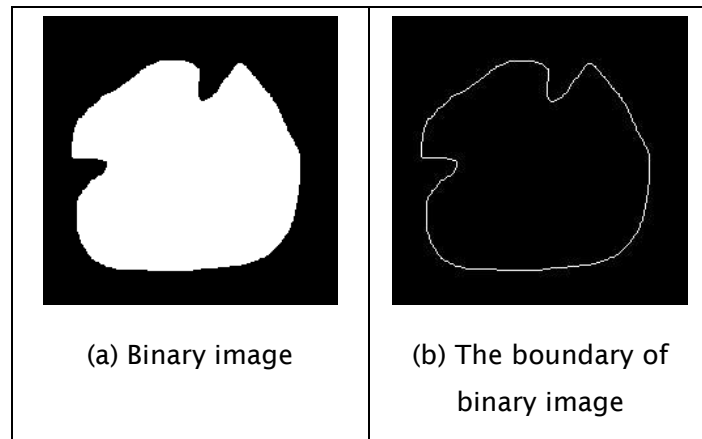


Figure 4-4. Boundary extraction from binary image

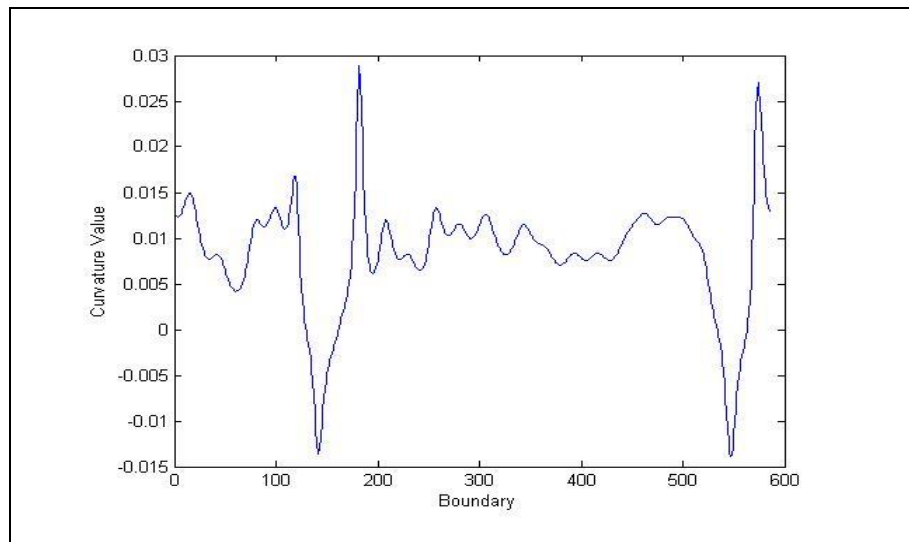


Figure 4-5. The curvature graph of the object in Figure 4-4



## 4.4 Compactness

### Classical Compactness

Compactness plays an important role in classification and shape analysis as this measurement is extracted using the main properties for planar shape: perimeter and area of objects. This measure is also becoming an essential feature in medical applications such as in detection of lung nodules [72], cancer [41] and atherosclerotic disease [73]. In this feature, the compactness of the vessel shapes is used as a feature to differentiate AD from other normal brains. The compactness  $C$  of an object can be measured by the ratio of the perimeter to the area of a given shape as follows:

$$C(S) = \frac{4\pi A(S)}{P^2(S)} \quad (4-12)$$

Compactness measures the efficiency with which a boundary encloses area. For a perfect circular region  $C = 1$ , which represents the maximum compactness value as a circle is the most compact shape [37]. In contrast, in a convoluted region, the value will be lower. If we measure the perimeter of a convoluted region and draw a circle with the value, the circle will contain a greater area. Thus, the object is not as compact as the circle. The example of variety of compactness is illustrated in Figure 4-6

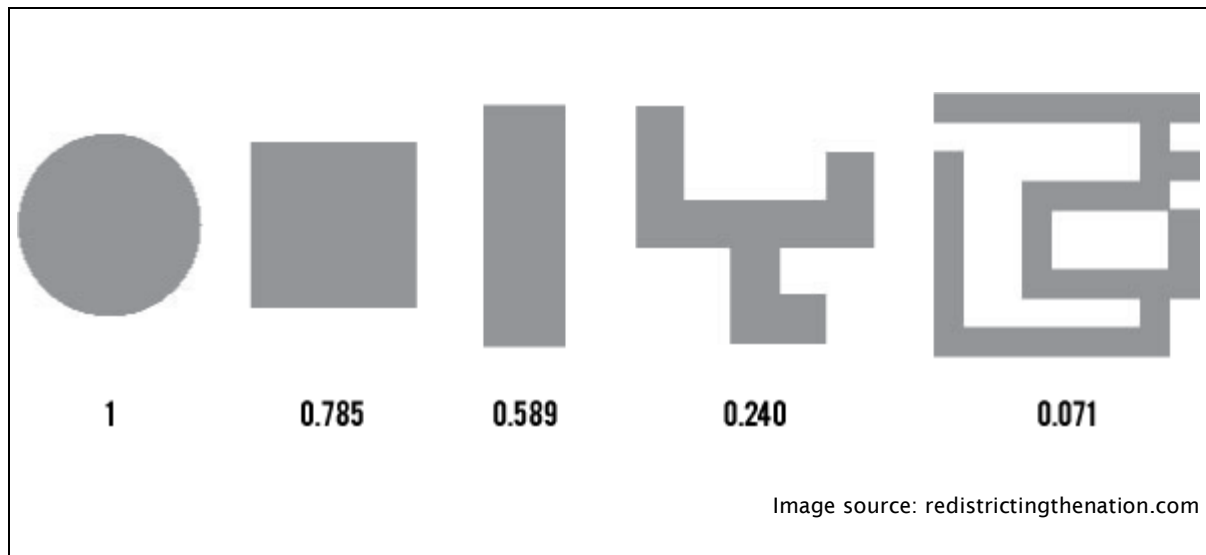


Figure 4-6. The variety of objects with their compactness

As this measurement is an intrinsic property of objects, the measure of compactness is invariant under geometric transformations, such as translation, rotation and scaling. In our analysis, compactness is deployed to measure the compactness of the blood vessels in the brain.

### Discrete Compactness

Due to the noise within the input images, many shapes have no well-defined contours. The measurement in Equation (4-12) might produce perimeters affected by noise or enclosing-surfaces with larger values which will affect the measure of compactness. Therefore, the measurement of compactness has to be improved to solve this problem in the digital domain. An approach originally developed by Brisbjesca [74] is to assume that an entity has been isolated from the real world. Therefore, the equation of compactness employs pixels for 2D images and voxels for 3D volumes. The compactness by this measure is defined to be maximum for a square region (in 2D images) and a cube (in 3D images) and has the highest possible value (which is 1) if and only if the measured shape is a square region or a cube.

This definition of compactness is a measure that is sensitive to changes in shape and is computed, for a given structure, as the ratio of contact perimeter  $P_c$  to the maximum contact perimeter  $P_{c_{max}}$ . The contact perimeter is essentially a measure of the number of occasions when pixels within a shape are adjacent. The maximum contact perimeter  $P_{c_{max}}$  is that obtained for a square or a cube. The measure is normalised to be of value between 0 and 1, and is invariant to scaling, rotation, and translation. Even though it is not a new definition, this measurement is yet to be implemented in this field. Thus, in this research we implement this measurement for finding its capabilities as blood feature descriptor.

The new definition of compactness  $C_d$  by Brisbjesca for 2D as follows:

$$C_d = \frac{P_c}{P_{c_{max}}} \quad (4-13)$$

The contact perimeter  $P_c$ , of a 2D shape composed of pixels corresponds to the sum of the length of segments that are common to each pair of pixels within the shape. In other words the greater contact perimeter every object has higher compactness of the object. The equation of  $P_c$  can be expressed as:

$$2P_c + P = 4 \times l \times n \quad (4-14)$$

where  $n$  is the number of pixels of the object,  $l$  is the length of side of the pixel (in this case  $l$  is assumed to be one) and  $P$  is the perimeter of the object, which means the sum of the segments lengths of the closed shape's sides. This measure corresponds to the classical concept of perimeter.

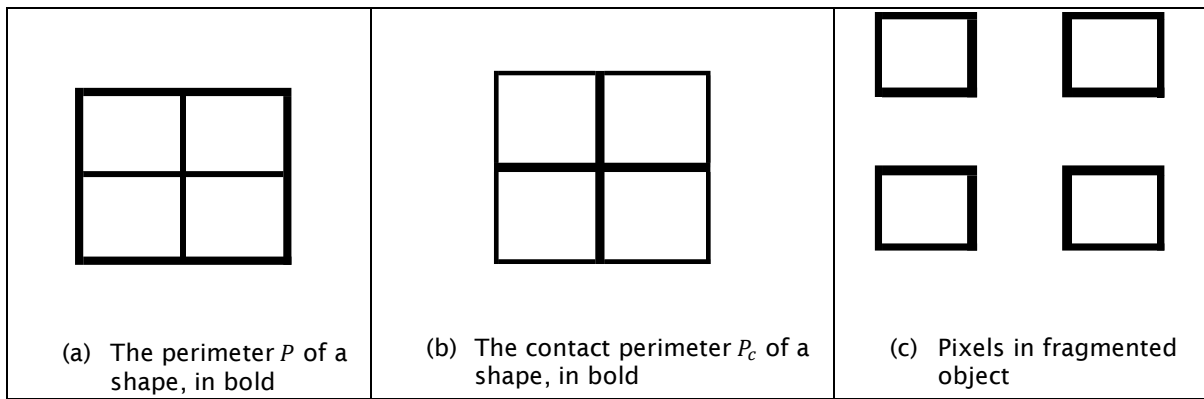


Figure 4-7. Comparison between the perimeter and the contact perimeter

In Figure 4-7, the rectangular shape has a perimeter value of eight pixels (a) and the contact perimeter of four pixels (b). Thus, when a rectangular shape is separated into a fragmented shape like (c), the total perimeter of the shape is four sides of one pixel times the number of pixels, which results in 16 pixels. It is equal to the sum of two times the contact perimeter  $P_c$  plus the perimeter  $P$ .

The contact perimeter  $P_c$  is defined as:

$$P_c = \frac{4ln - P}{2} \quad (4-15)$$

Then, the maximum measure of the contact perimeter  $P_{c_{max}}$  of discrete compactness  $C_d$  for a square composed of  $n$  pixels is obtained using Equation (4-16), as:

$$P_{c_{max}} = 2(n - \sqrt{n}) \quad (4-16)$$

given that a square region of pixels is the most compact shape and its perimeter  $P$  is  $4\sqrt{n}$ .

We have illustrated the example of the definition of  $P_c$  in Equation (4-4). For a region containing 9 pixels the square region has the greatest value of  $P_c$  and the irregular figure has the smallest value. Note that the value of  $P_c$  in (c) is the same as that for a straight line since neither has any compactness.

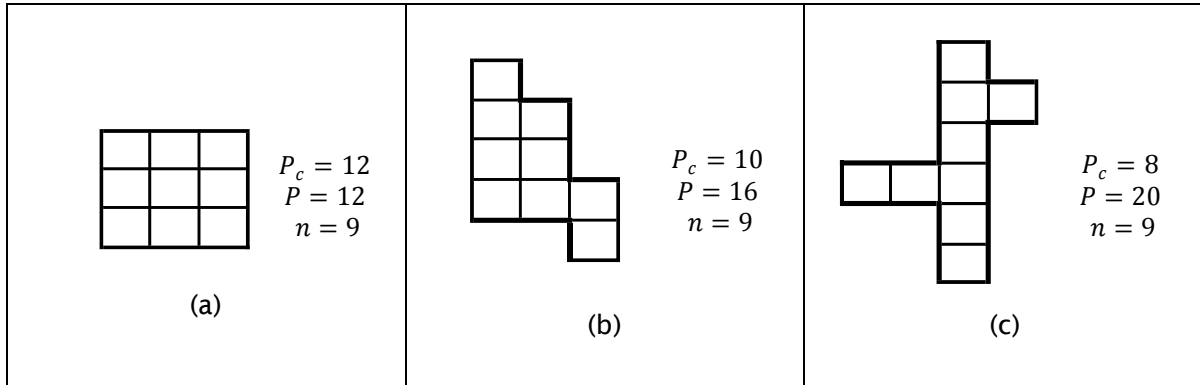


Figure 4-8. Variety of shapes and their contact perimeter

The compactness  $C_d$  is obtained by combining Equations (4-15) and (4-16) as:

$$C_d = \frac{n - P/4}{n - \sqrt{n}} \quad (4-17)$$

where  $n$  is the number of pixels in the objects and  $P$  is its perimeter. This method considers that all images that are analysed using the computer vision technique are based on pixels. This method also varies linearly, which indicates that this feature is suitable for shape classification. It produces a robust measure for noisy perimeters as this method largely depends on the summation of contact perimeters of the side-connected pixels. For the case presented in Figure 4-8 (a-c), when substituting these values in Equation (4-17), the compactness of the shapes is 1, 0.7 and 0.2, respectively.

To verify which method is suitable in our analysis, the analysis for compactness using both methods is performed and the results show that the discrete compactness shows a higher classification rate than the classical approach.

## 4.5 Planar Fourier Descriptors

Fourier descriptors (FDs) have been shown to be an efficient way to recognize shapes due to their robustness to changes in scale, rotation, shifting and starting point. Furthermore, although the FDs technique is already more than 40 years Old, it has features that are easy to compute and robust to noise. Although curvature has already been shown to be a robust technique to measure tortuosity by preserving the information of its boundary, it is important for us to find the best measurement to describe the vessels. Accordingly, by considering an approach that is intrinsically scalable, rotational and shift invariant, we might achieve a more robust measurement to describe the vessels.

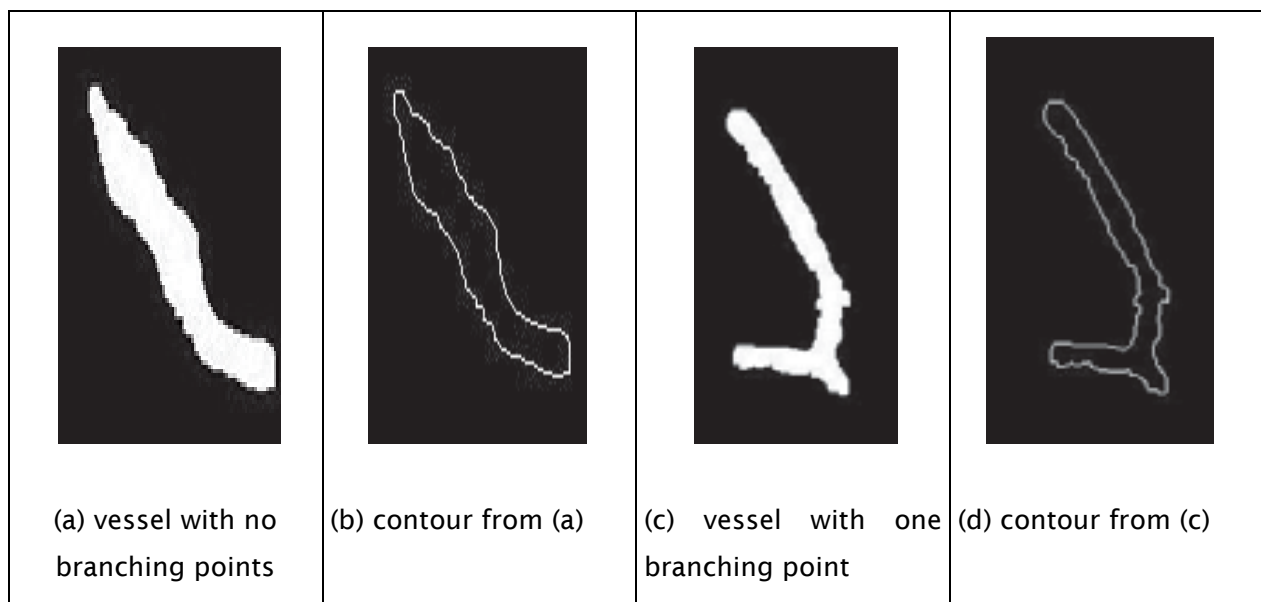


Figure 4-9. Vessels for FDs analysis.

As a general rule, as illustrated in Figure 4-9, FDs are achieved by using Fourier analysis to find the frequency content of the whole shape by using the contour derived from shape boundary coordinates [37]. Based on frequency analysis, we can choose a small set of numbers, or better known as the Fourier coefficients, which describe a shape rather than any noise that might corrupt it.

For FDs analysis, a curve is two-dimensional (2D) and the image space is considered as a complex plane [39]. Thus, every pixel is represented by a complex number.

$$s(k) = x(k) + jy(k) \quad (4-18)$$

where  $x(m)$  and  $y(m)$  is the coordinates of the boundary.

In FDs, the Discrete Fourier Transform is applied since the contour of the shape is defined by closed curves and Fourier descriptor can be denoted as:

$$a(u) = \sum_{k=0}^{K-1} s(k) e^{\frac{-j2\pi uk}{K}} \quad (u = 0, 1, 2, \dots, K-1) \quad (4-19)$$

The inverse Discrete Fourier Transform of these coefficients reconstructs  $\hat{s}(k)$ :

$$\hat{s}(k) = \frac{1}{P} \sum_{u=0}^{P-1} a(u) e^{\frac{j2\pi uk}{P}} \quad (k = 0, 1, 2, \dots, K-1) \quad (4-20)$$

where  $P$  is the number of specified Fourier coefficients.

The normalisation needs to be implemented in order to obtain FDs that are invariant to scaling, shifting, rotating and the starting point. It is an important feature that makes FDs have an important role in shape analysis. As such, every invariant feature has to be calculated by the formulae in Table 4-1.

Transformation	Fourier Descriptor
Translation	$a_t(u) = a(u) + \Delta_{xy}\delta(u)$
Scaling or Zooming	$a_s(u) = \alpha a(u)$
Starting point	$a_p(u) = a(u)e^{-j2\pi k_0 u/K}$
Rotation	$a_r(u) = a(u)e^{j\theta}$

Table 4-1. The measurements of invariants in FDs

An alternative approach is to use Elliptic FDs which also have similar invariance to complex FDs, but do not include the effects of high order frequencies that are more prone to noise [75]. Let us denote  $c'(t) = x'(t) + jy'(t)$  as the transformed contour. This contour is defined as:

$$\begin{bmatrix} x'(t) \\ y'(t) \end{bmatrix} = \frac{1}{2} \begin{bmatrix} a'_{x0} \\ a'_{y0} \end{bmatrix} + \sum_{k=1}^{\infty} \begin{bmatrix} a'_{xk} & b'_{xk} \\ a'_{yk} & b'_{yk} \end{bmatrix} \begin{bmatrix} \cos(k\omega t) \\ \sin(k\omega t) \end{bmatrix} \quad (4-21)$$

The advantage of these descriptors  $a'$  and  $b'$  with respect to complex FDs is that they do not involve negative frequencies. In Equation (4-22), the Elliptic FDs are also made invariant to contain neither the scale factor, nor rotation.

$$\frac{|A'_k|}{|A'_1|} = \frac{\sqrt{a'^2_{xk} + a'^2_{yk}}}{\sqrt{a'^2_{x1} + a'^2_{y1}}} \text{ and } \frac{|B'_k|}{|B'_1|} = \frac{\sqrt{b'^2_{xk} + b'^2_{yk}}}{\sqrt{b'^2_{x1} + b'^2_{y1}}} \quad (4-22)$$

Even though FDs have been one of the most popular boundary descriptions in shape analysis there is a limitation concerning shape recognition in as much as this technique can only detect similar shapes. This is because this technique was initially used to remove the noise that occurred in the boundary, and consequently, it is well applied to recognize similar objects that have a similar pattern as the original. Therefore, FDs cannot be used for mixed shapes, which rely on extraction techniques that can handle occlusion[37]. Consequently, it is difficult to implement FDs technique to differentiate the branching structures that have a mixture of shapes, even though the description is robust to scaling, starting point and rotation. For this reason, we have to construct an algorithm that can fit this technique to measuring the dissimilarity between AD and a normal brain; this is discussed later in the analysis section of this chapter.

## 4.6 Analysis of Extracted Features

### 4.6.1 Analysis of Density measurement

ANOVA					
	Sum of Squares	df	Mean Square	F	Sig.
Between Groups	3130.000	2	1565.000	4.072	.045
Within Groups	4612.000	12	384.333		
Total	7742.000	14			

Table 4-2 ANOVA table for analysis of density

In this analysis, we compare the density of the groups using ANOVA to find whether there is any statistically significant difference among them. The  $p$ -value (denoted by Sig.) as shown in Table 4-2 is 0.045 and this means there is statistically significant difference at  $p < 0.1$  level in density amongst three groups. Subsequently, the Post Hoc test is done to measure the difference in means between the classes. Tukey HSD test is used for Post Hoc test and the result is shown in Table 4-3. This table indicates that there is a significant difference between AD and Old in density with  $p$ -value of 0.038. However, there is no significant difference by comparing AD versus Young and Old versus Young with  $p$ -value = 0.562 and 0.219, respectively. AD shows higher density amongst the groups with mean difference between AD and Old of 35 and AD and Young of 13. This means that the density can be a good factor for the detection of AD.

Higher density in AD may be due to the regeneration of new vessels in AD. The regeneration of vessels in AD is caused by the dead vessels due to the accumulation of A $\beta$  in the brain. Interestingly, from three groups, it appears that the AD and Young have comparable levels of density. The normal vessels in Young brains may be dead and the regeneration of new vessels makes the density similar. The lower number of Old brains is constantly low due to dead vessels in its brain and indicates that the brains have no regeneration of vessels caused by AD. If the regeneration of new vessels happens in the AD brain, the vessels' structure could be changed by their tortuosity, as the new vessels can find its new way in unaffected regions. Consequently, for deeper analysis, the tortuosity and other shape descriptors are analysed to find their connection to AD in the next analysis.



### Multiple Comparisons

Tukey HSD

(I) Grouping	(J) Grouping	Mean Difference (I- J)	Std. Error	Sig.	90% Confidence Interval	
					Lower Bound	Upper Bound
Old	Young	-22.000	12.399	.219	-50.09	6.09
	Alzheimer's Disease	-35.000*	12.399	.038	-63.09	-6.91
Young	Old	22.000	12.399	.219	-6.09	50.09
	Alzheimer's Disease	-13.000	12.399	.562	-41.09	15.09
Alzheimer's Disease	Old	35.000*	12.399	.038	6.91	63.09
	Young	13.000	12.399	.562	-15.09	41.09

\*. The mean difference is significant at the 0.1 level.

Table 4-3 Multiple comparisons table for Tukey HSD test for density between groups

#### 4.6.2 Analysis of Tortuosity measurement

For the extensive analysis, we test the significance difference using ANOVA after obtaining the data set to choose the best tortuosity measurement for classification. As depicted in Table 4-4, the  $p$ -value of log T shows the lowest value amongst other measurements which is  $p=0.075$ . The other measurements of tortuosity are exceeding the statistical significant level of  $p=0.1$  as shown in Table 4-4. Thus, it can be concluded that the other measurements are not suitable to use as features for classification. For deeper analysis, we chose the best tortuosity measurement; log T to represent tortuosity as one of the feature descriptions.

ANOVA

		Sum of Squares	df	Mean Square	F	Sig.
logT	Between Groups	.023	2	.011	3.241	.075
	Within Groups	.042	12	.003		
	Total	.065	14			
bendET	Between Groups	3407617403.764	2	1703808701.882	2.130	.162
	Within Groups	9599651016.425	12	799970918.035		
	Total	13007268420.189	14			
meanT	Between Groups	.000	2	.000	.006	.994
	Within Groups	.232	12	.019		
	Total	.232	14			
normalT	Between Groups	.009	2	.005	1.750	.215
	Within Groups	.031	12	.003		
	Total	.040	14			

Table 4-4. ANOVA table for various measurement of Tortuosity

For log T measurement, we have run the Post Hoc test of Tukey HSD to find the difference means of each group. Contrary to the measurement of density which can differentiate Old and AD, the tortuosity using logT can only discriminate AD and Young with  $p=0.062$  as

demonstrated in the Table 4-5. The angiogenesis recorded in AD may contribute to the complexity of the vessel network hence increasing the tortuosity of the vessel. Thus, this measurement will be used as one of the measures in feature description of branching vessels.

We perform the Post Hoc Test of Tukey HSD to find the difference between groups mean. Surprisingly, the comparison between AD and Old are not significant as  $p$ -value of 0.413 which is exceeding the threshold. However, we have obtained the  $p$ -value of 0.062 which is below significance level of  $p=0.1$  by comparing between AD and Young. In statistical point of view, the tortuosity of blood vessels of AD are different from that of Young. It might indicates that the angiogenesis as occurs in AD might contribute the tortuosity of the vessels. Even though the comparison between AD and Old are not significant, it does not mean that these are the same. Future works particularly on increasing the sample data may improve the analysis hence the better understanding will be achieved.

## Post Hoc Tests

### Multiple Comparisons

Tukey HSD

(I) Group	(J) Group	Mean Difference (I-J)	Std. Error	Sig.	90% Confidence Interval	
					Lower Bound	Upper Bound
Old	Young	.04595	.03741	.460	-.0388	.1307
	AD	-.04926	.03741	.413	-.1340	.0355
Young	Old	-.04595	.03741	.460	-.1307	.0388
	AD	-.09521*	.03741	.062	-.1800	-.0105
AD	Old	.04926	.03741	.413	-.0355	.1340
	Young	.09521*	.03741	.062	.0105	.1800

\*. The mean difference is significant at the 0.10 level.

Table 4-5. Tukey HSD Post Hoc test for logT measurement of Tortuosity.

### 4.6.3 Analysis of Compactness

For compactness, we compare the classical compactness method with discrete compactness method, and then we choose which one has the best classification rate to use as the feature description of the vessel.

As an initial stage, we compare both of the measurement using ANOVA to investigate their statistical significance for comparison amongst groups. As presented in Table 4-6, both of them have lower  $p$ -value than significant level of  $p=0.1$  which are  $p=0.003$  for Discrete Compactness and  $p=0.002$  for Classical Compactness. Since the  $p$ -value for both measurements are remarkably low, it indicated that measurement of compactness displays an important feature for blood vessel description.

ANOVA

		Sum of Squares	df	Mean Square	F	Sig.
Discrete Compactness	Between Groups	.000	2	.000	10.095	.003
	Within Groups	.000	12	.000		
	Total	.000	14			
Classical Compactness	Between Groups	.009	2	.004	10.923	.002
	Within Groups	.005	12	.000		
	Total	.013	14			

Table 4-6. ANOVA table for various measurement of Compactness

We also performed Post Hoc analysis of Tukey HSD for comparing the difference of mean group. The lower  $p$ -value exhibited in Table 4-7 indicates that both measurements show significant difference for AD versus Old and Young versus Old. However, the comparison of Young versus AD has exceeded the significant level of  $p=0.1$ . It could be inferred that the compactness is different by disease profile and by age. Interestingly to note, the mean value of compactness in Old is the highest amongst the groups. This result is consistent with the report addressed by Geary and Buchholz[76]

## Multiple Comparisons

### Tukey HSD

Dependent Variable	(I) Grouping	(J) Grouping	Mean Difference (I-J)	Std. Error	Sig.	90% Confidence Interval	
						Lower Bound	Upper Bound
Discrete Compactness	Old	Young	.007 <sup>*</sup>	.002	.006	.003	.011
		Alzheimer's Disease	.007 <sup>*</sup>	.002	.005	.003	.012
	Young	Old	-.007 <sup>*</sup>	.002	.006	-.011	-.003
		Alzheimer's Disease	.000	.002	.994	-.004	.004
	Alzheimer's Disease	Old	-.007 <sup>*</sup>	.002	.005	-.012	-.003
		Young	.000	.002	.994	-.004	.004
Classical Compactness	Old	Young	.041 <sup>*</sup>	.012	.017	.013	.069
		Alzheimer's Disease	.056 <sup>*</sup>	.012	.002	.028	.085
	Young	Old	-.041 <sup>*</sup>	.012	.017	-.069	-.013
		Alzheimer's Disease	.016	.012	.447	-.013	.044
	Alzheimer's Disease	Old	-.056 <sup>*</sup>	.012	.002	-.085	-.028
		Young	-.016	.012	.447	-.044	.013

\*. The mean difference is significant at the 0.10 level.

Table 4-7. Post Hoc Test for measurements of compactness

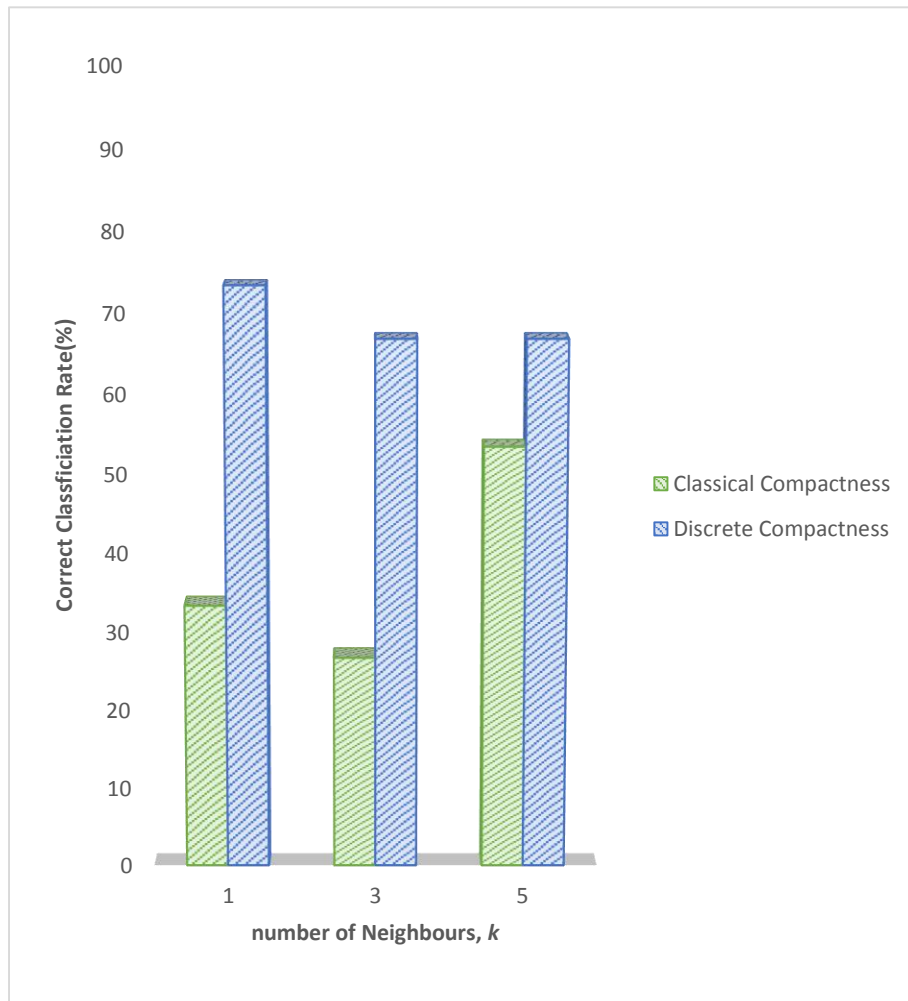


Figure 4-10. Comparison between classical and discrete compactness by increasing the number of  $k$  in  $k$ -NN classification technique

In Figure 4-10, we then measure the CCR using leave-one-out cross validation of  $k$ -NN classification between the classical and discrete compactness to see their performance. In this analysis, we can see that the compactness using discrete measurement shows competent capability of discrimination between AD, age-control and Young brains. Even though the difference between  $p$ -values by ANOVA analysis is small, the CCR rate is higher for discrete classification suggests that this measurement should be used as one of the features for shape description of AD.

#### 4.6.4 Analysis of Fourier Descriptors

In order to calculate FDs for each branch, we detect the branches which have branching point and labelled every of them. Then, we detect their boundary for FDs calculation. We then find the coefficients of the FDs for those branches in every image. We specify only the first 64 coefficients,  $P$  of coefficient for this descriptor after finding the optimum value of Fourier Coefficient at highest CCR at  $k=1$  and lower coefficient number which is 64 as shown in Figure 4-11. We then compare the FDs for each image using  $k$ -NN classification to differentiate between AD and other groups' images.

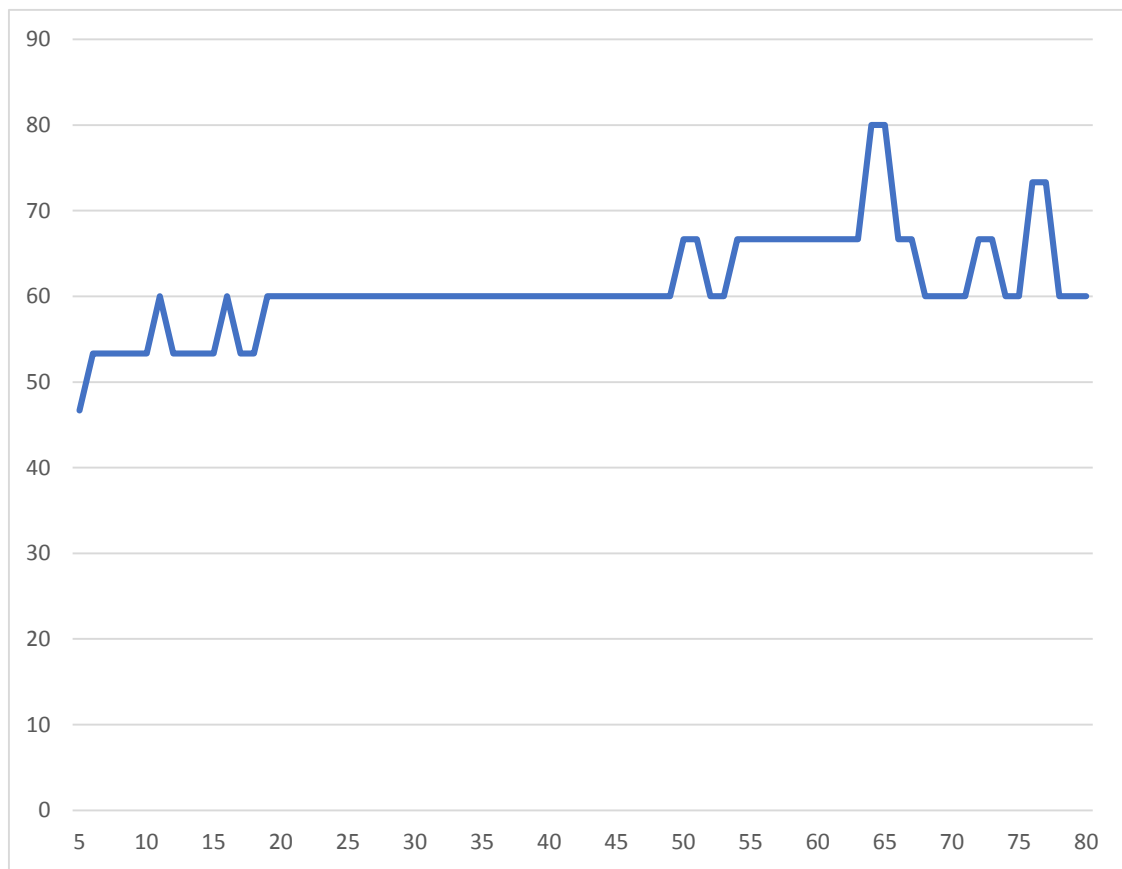


Figure 4-11. CCR using different number of FD coefficient.

In our analysis, we compare two different FDs to find the best FDs in our feature descriptor using  $k$ -NN classification. As the Fourier descriptor have more than one variable (in our case it is 64), the comparison was not done using ANOVA, as ANOVA needs only one variable for the comparison of each group. Clearly, as

shown in Figure 4-12, the higher CCR is obtained for the complex FDs, which is CCR of 80%.

The lower rate for elliptic FDs may be caused by the unsuitable shape descriptor as the elliptic is based on closed elliptical shape. As conclusion, the complex FDs is chosen for later analysis. The nature of this change is yet to be established, and is a likely consequence of the differing drainage of A $\beta$  in subjects with AD, leading to a high recognition capability.

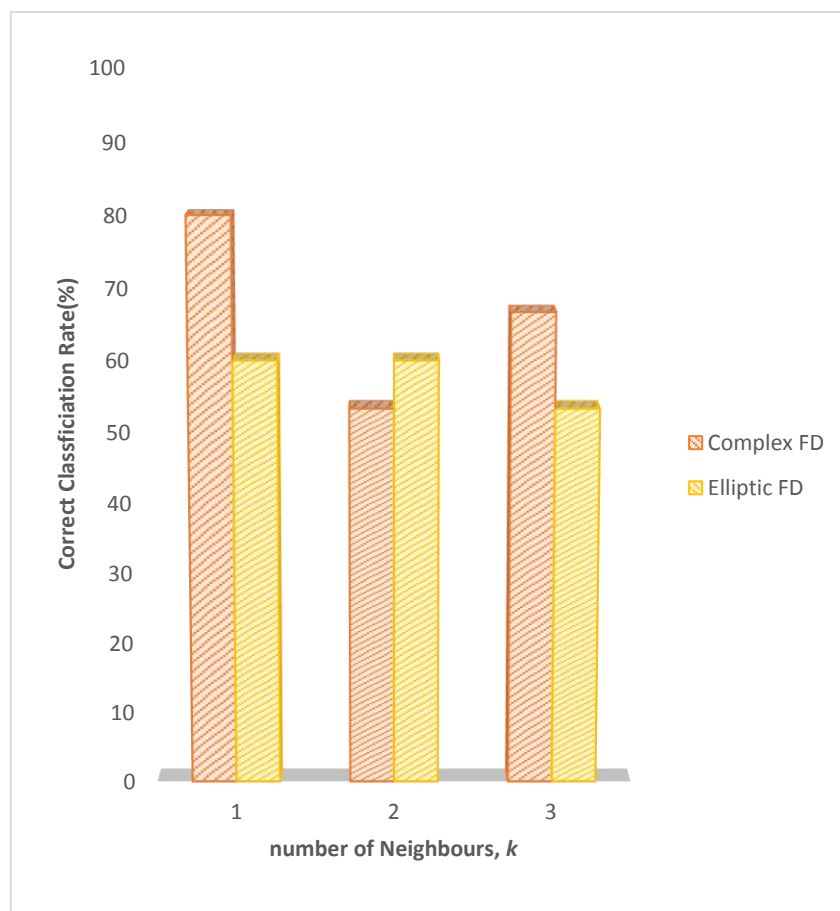


Figure 4-12. CCR using Complex and Elliptic FD



## 4.7 Results and Discussion

This part contains all the analysis of features. We divide our analysis into two stages, which are the deeper statistical analysis and the analysis of the performance of every feature and feature fusion. For the first analysis, deeper understanding of every feature is performed using contrast analysis for planned comparison. Planned comparison is the test when we have a specific question (hypothesis) about a pattern of results of an ANOVA. It is necessary when comparing specific group such as comparing AD with normal (defined by combination of Old and Young) or comparing Old and Young without looking at AD [77]. These questions are converted into equations that are translated by the contrast test into a set of numbers called contrast coefficients [78]. As described in Section 1.2, these are hypotheses for 2D analysis that we want to analyse using contrast test;

- a) Research Hypothesis 1: Is there any difference between AD and Normal Brain
- b) Research Hypothesis 2: Is there any difference between Normal Brain (Old versus Young)

**Contrast Coefficients**

Contrast	Group		
	Old	Young	Alzheimer's Disease
1	1	1	-2
2	1	-1	0

Table 4-8. Contrast coefficients of ANOVA

The above hypotheses are transformed into statistical hypotheses as shown in Table 4-8. For the first contrast, we want to take the Old and Young groups and combined them as one group. Thus, the coefficient value will be the same which is 1. Then as we want to compare AD with normal (Young and Old), AD will have a coefficient value of -2. The sum of coefficients for each statement is zero as it should be for a contrast. If we want to ignore one of the three groups (for example comparing Young with Old), then we need to adjust the other coefficient value so that the sum of coefficients is zero. On the other hand, for the second contrast analysis, we compare between Old and Young while ignoring group AD, so the coefficient of group Old will be 1 and of group Young will be -1 while group AD will have a coefficient of 0. Subsequently, coefficients with different values are compared and the result is shown in Table 4-9 and Table 4-10 respectively.

As shown in Table 4-9, the homogeneity of variances was analysed between group using the Levene Test of Homogeneity of Variances [77] in order to understand the contrast analysis. In Table 4-10, all the  $p$ -value of the features for the contrast (1) is lower than significant level of  $p=0.1$ . It is clearly evident that the AD is different from normal brain tissue for all the features. Amazingly, for the second contrast, it appears from the evidence that only compactness is rejecting the null hypothesis that Old is same with Young. As the blood vessels lose their tone due to ageing, they become of a different shape from Young. The smooth muscles become very flat and the “cement” between them (the basement membranes that are the drainage pathway that we are investigating) are also changing in composition and morphology [79]

This result nevertheless suggests that only compactness from all the features tested could be used as a feature for classification of Old and Young brain. This indeed provides an understanding that Compactness has distinctive features that are different from other features. Hence, the analysis will continue to figure out the feature fusion for higher CCR.

Test of Homogeneity of Variances				
	Levene Statistic	df1	df2	Sig.
Branching Structure	.352	2	12	.711
Density	11.218	2	12	.002
Tortuosity	.184	2	12	.834
Compactness	12.731	2	12	.001

Table 4-9. Test of Homogeneity of Variances of all 2D features

### Contrast Tests

Contrast		Value of Contrast	Std. Error	t	df	Sig. (2-tailed)
Branching Structure	Assume equal variances	-.327	.158	-2.073	12.000	.060
		-.134	.091	-1.467	12.000	.168
	Does not assume equal variances	-.327	.167	-1.964	6.912	.091
		-.134	.086	-1.558	7.271	.162
Density	Assume equal variances	-48.000	21.476	-2.235	12.000	.045
		-22.000	12.399	-1.774	12.000	.101
	Does not assume equal variances	-48.000	16.879	-2.844	7.063	.025
		-22.000	14.577	-1.509	4.435	.199
Tortuosity	Assume equal variances	-.144	.065	-2.230	12.000	.046
		.046	.037	1.228	12.000	.243
	Does not assume equal variances	-.144	.071	-2.025	6.273	.087
		.046	.033	1.385	7.946	.204
Compactness	Assume equal variances	.008	.003	2.334	12.000	.038
		.007	.002	3.839	12.000	.002
	Does not assume equal variances	.008	.003	3.010	7.311	.019
		.007	.002	3.247	4.840	.024

Table 4-10. Results of Contrast Analysis of all 2D features

Due to the similar pattern of statistical result of tortuosity, density and branching structure, thus we combined them as one feature to analyse their potential for increasing the classification rate. These three features are normalised by z-score normalization[80]. The significant test for this feature fusion is measured using ANOVA to investigate its effect of this feature on these groups. Moreover, the classification rate for this feature is measured using leave-one-out cross validation for *k*-NN classification.

### ANOVA

#### Feature Fusion

	Sum of Squares	df	Mean Square	F	Sig.
Between Groups	11.440	2	5.720	7.862	.001
Within Groups	30.560	42	.728		
Total	42.000	44			

Table 4-11. ANOVA table for feature fusion.

As depicted in Table 4-11, there is a very significant effect by combining these features at the  $p < 0.1$  level for these three groups [ $F(2, 42) = 7.862, p = .001$ ]. Since we have found a statistically significant result in this feature, Post Hoc test (Tukey HSD) is computed to compare each of our groups to every condition. Post Hoc comparisons using the Tukey HSD test as in Table 4-12 indicates that the mean score for the AD is significantly different than Old and Young. However, the Old is not significantly differing from Young.

#### Multiple Comparisons

Dependent Variable: Feature fusion

Tukey HSD

(I) Group	(J) Group	Mean Difference (I-J)	Std. Error	Sig.	90% Confidence Interval	
					Lower Bound	Upper Bound
Old	Young	-.35583	.31147	.494	-1.0130	.3013
	AD	-1.20216*	.31147	.001	-1.8593	-.5450
Young	Old	.35583	.31147	.494	-.3013	1.0130
	AD	-.84634*	.31147	.025	-1.5035	-.1892
AD	Old	1.20216*	.31147	.001	.5450	1.8593
	Young	.84634*	.31147	.025	.1892	1.5035

\*. The mean difference is significant at the 0.10 level.

Table 4-12. Post Hoc result using Tukey HSD for feature fusion

It is interesting to note that when we performed the same contrast test to feature fusion, similar result from the test that has been conducted for each feature (tortuosity, density and branching structure) has been obtained. The AD is statistically different from Normal (Old and Young) and Old and Young is not statistically significant. It indicates that these features are associated with each other.

For the second analysis, we performed the classification using  $k$ -NN classification in order to obtain the CCR for those features including the feature fusion. We use LOOCV and take one image from the dataset to test the image and the rest become the training set for that classification. We then find the CCR for each cycle and the average for all cycle. Overall, we performed the classification of six features and obtained the CCR for each feature. For the overall section, we used  $k = 1, 3$  and  $5$ .

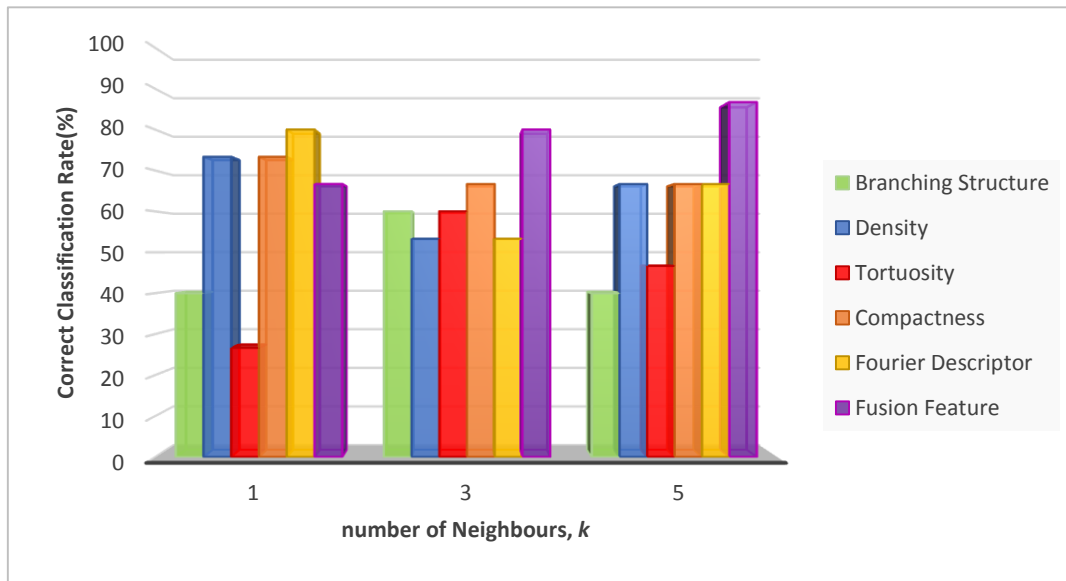


Figure 4-13. CCR of  $k$  for each features between three groups.

Figure 4-13 shows the CCR for each feature applied to the three groups together, discriminating the images from subjects with AD from the images derived from other brains. The best performance (excluding the feature fusion) was achieved by the FDs: this shows a CCR of 80% for the nearest neighbour and reduces somewhat with increasing values of  $k$  suggesting that the discrimination of the shape in this dataset needs the invariants that are well described in the FDs algorithm. The low CCR for  $k=3$  suggests that there is some uncertainty in the feature space, which warrants further investigation.

Interestingly, the CCRs related to compactness exhibit steadiness with increasing values of  $k$ , indicating that the feature space associated with compactness is smoother than those associated with other measures. This could be achieved by improving the pre-processing technique, such as the skeletonisation process. This technique computed in this study is highly complicated so much so that it might contribute to the lower CCR of the feature associating to it (tortuosity and branching structure). Clearly, the results show that discrimination can be achieved, however, the underlying procedures could benefit from further investigation and refinement.

Even though that the measures of tortuosity, branching structure, compactness and FDs are simply averaged over all branches to obtain single values per image, we could still achieve a good classification rate. At this particular stage we are

interested as to whether the broad class has a capability to discriminate the structures of interest. As all numbers can be normalised, it becomes a matter of consistency. Thus, in pattern recognition, it is about whether we can yield the same measures consistently for different samples of the same class. If the measures are inconsistent, recognition cannot be achieved.

Comparing to all single features, the feature fusion obtained the highest CCR when  $k=3$  and  $k=5$  which is 87%. The performance of this feature fusion is better than when performing classification separately to branching structure, density and tortuosity. This fusion is also better than compactness and FD which have higher classification rate.

## 4.8 Conclusions

In conclusion our pilot study of branching density by using the number of branches shows that this measure is a novel contributor to discriminate AD from a normal brain. It also can be concluded that the AD are different from other subjects due to formation of a new branches (angiogenesis). Furthermore, the result of tortuosity has contributed in defining the branching structure and motivated us to increase the performance of the classification by finding a better way to measure tortuosity. As a result, we developed another measurements based on curvature.

Unsurprisingly, the curvature-based tortuosity showed a competitive CCR compared to the normal measurement of tortuosity. By focusing on the curvature, we can conclude that the measurement of log-based tortuosity has a significant result for the CCR suggesting that the definition of tortuosity in log-based-curvature measurement is trustworthy. The calculation of differentiation on the curvature measure has to be looked at further to ensure robust calculation of the curvature.

Next, the measurement of compactness showed high classification capability. The definition of vessels according to their compactness indicates the efficiency of the blood flow in the vessels. The implementation of existing discrete compactness equation for this analysis appears to be new in this area and it shows higher discrimination capability than classical compactness, since the measure considered digitisation in its formulation. Even though the discrete compactness is not new but the implementation of this measurement is still new. Thus, this measurement will be chosen for the next analysis.

Finally, we used FDs as one of features to define the shape of vessels. With regard to FDs that are invariant to scale, rotation and translation, as well as the starting point helped to provide a significant result for recognition; we obtained a good result for FDs suggesting the capability of this feature for shape classification. We perform the analysis using Complex FDs which showed a higher classification rate than Elliptic FDs.

In our final analysis, we tested the abilities of these features to compare AD versus Normal Old versus Young using a contrast analysis. As result, AD is statistically different from Normal for these features. While by only using compactness, Old and Young are statistically different. These results could indicate the understanding of the features better in terms of medical analysis.

By combining three features which are tortuosity, branching structure and branching density, we obtained highest CCR compared to all single features. This indicated that these features are associated with each other.

Our measurements are conducted in 2D environment using microscopic images show good discrimination capabilities. However, this environment has limitation on dimensions of the branches hence the branches are not well represented for whole brain. Hence, the classification capability could be improved by using another environment which is a three-dimensional approach. The studies so far have been on brain tissue samples and are thus in vitro tests. Development of recognition capability on live subjects is of considerably more interest, though analysis protocols naturally need to follow established medical guidelines. For our next chapter, MRI based 3D-environment are used to magnify our method for feature description of branching in brain.

## 5. MRI Image Analysis

### 5.1 Introduction

One novelty in this thesis lies with the data and its analysis of Magnetic Resonance Angiography (MRA) which is a technique in common use to extract images of blood vessels. MRA is a group of techniques based on magnetic resonance imaging (MRI) that generate images of arteries in order to evaluate them for abnormality in the neck or brain, such as stenosis (abnormal narrowing), occlusions, aneurysms (vessel wall dilatations, at risk of rupture) or other abnormalities. Even though this technique does not involve any radiation, the area of the body being studied will be injected with a dye to make the vessels show up more clearly. Therefore, allergic reactions to the substance might occur, especially in the patients with AD. Moreover, there is considerable discussion regarding the capabilities of MRA to detect the abnormalities in the body [81].

Notwithstanding these potential problems, the advantages of MRA are immense. By undergoing just one simple process of MRI, we should have the capability to detect changes and abnormalities in the body with the help of computer vision. In this chapter, different features are studied by extending the features in the studies of capillaries to MRI. We define the anterior and posterior capillaries as part of a first stage in MRI image analysis targeted to later find the detection capabilities of AD via MRI in future work. Our new approach develops and deploys an extended 3D model-based branching structure described in the next section followed by other features, which are described in Section 5.3. The overall analysis is summarized in Section 5.4 with discussion and conclusions later.

#### 5.1.1 Why posterior and anterior?

Cerebral amyloid angiopathy (CAA) is a neurological condition characterised by the build-up of proteins such as amyloid on the walls of arteries in the brain. The condition increases the risk of stroke and dementia and occurs in 80-100% of the cases associated with AD [82]. The amyloid disturbs the blood flow of the vessel as well as the vascular network of the brain. Thal found some alteration in blood flow in the thalamic region of mice [83]. In most cases, CAA is found in the temporal and occipital lobes. This part of the brain is supplied mostly by the posterior cerebral artery, which may indicate an inclination for this region of the vascular network circulation to develop CAA [8]. In this research, comparing the structure of the branches in the posterior circulation to those in the anterior circulation will identify markers that can be used in future to assess those patients with mild cognitive impairment and therefore at risk of progressing to AD.



### 5.1.2 Pre-processing

The segmentation of vessels in 3D images has received growing attention in recent years due to its importance in assisting the diagnosis of many diseases. It is indeed an essential phase for the accurate visualization of vessels from sophisticated datasets and for the assessment of pathologies. works have been on 3D segmentation and have been reviewed thoroughly by Lesage D *et al.*[84]. It can be concluded that 3D segmentation can be categorised into different kind of approaches. The main approach of 3D segmentation is to use a Hessian matrix which requires second-order partial derivatives of an image [85]. Generally in these approaches that has been applied by Frangi *et al.*[86], Sato *et al.* [87], Koller *et al.* [88], Krissian *et al.*[89], Bullitt *et al.*[90] and Manniesing *et al.*[91], eigenvalues and eigenvectors of the Hessian are exploited, and often a vesselness measure is defined based on eigenvalues. However, the segmentation of vessels from MRI is difficult and challenging for many reasons such as the noise in the images and various of types and width of vessels which can make the segmentation difficult [85].

Thus, for our pre-processing of 3D features, as this is our pilot project, we implemented manual segmentation using morphological operations, which include erosion, dilation and skeletonisation of the MRI images as shown in Figure 5-1. Furthermore, as our main analysis focuses on the description of the shapes and features of blood vessels, manual segmentation is done by manually selecting the region of interest (ROI) which is the middle part of the brain by deleting the skull and the unnecessary parts of each frames in each images. It is necessary as the skull has a similar intensity value to the blood vessels. Then, the grayscale-images are converted to binary images using thresholding.

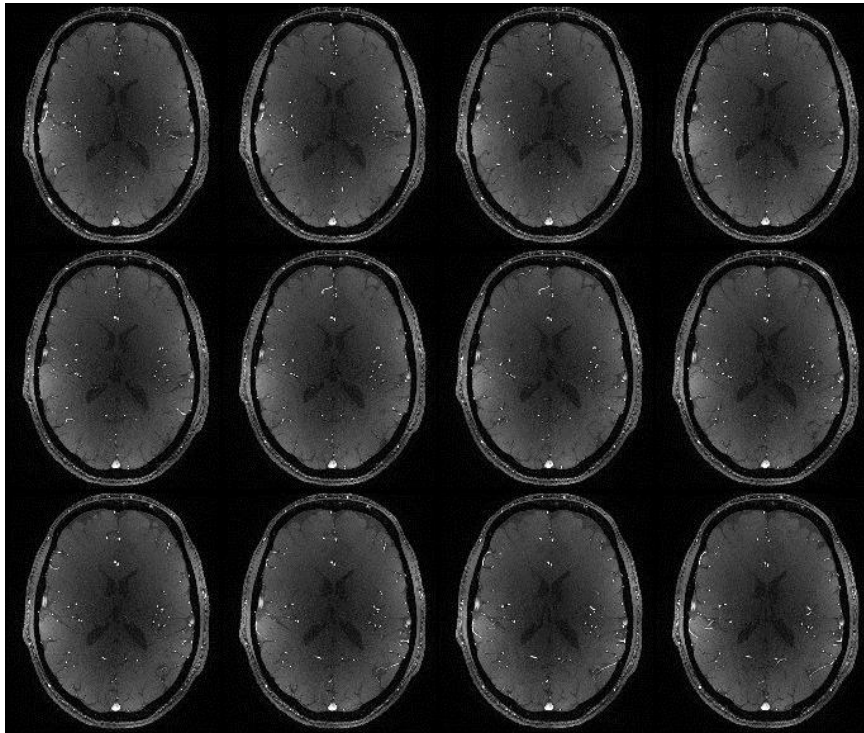


Figure 5-1. Example of 3D MRI montage of a normal brain

Morphological operation is used to improve the segmented vessel by using erosion and dilation.

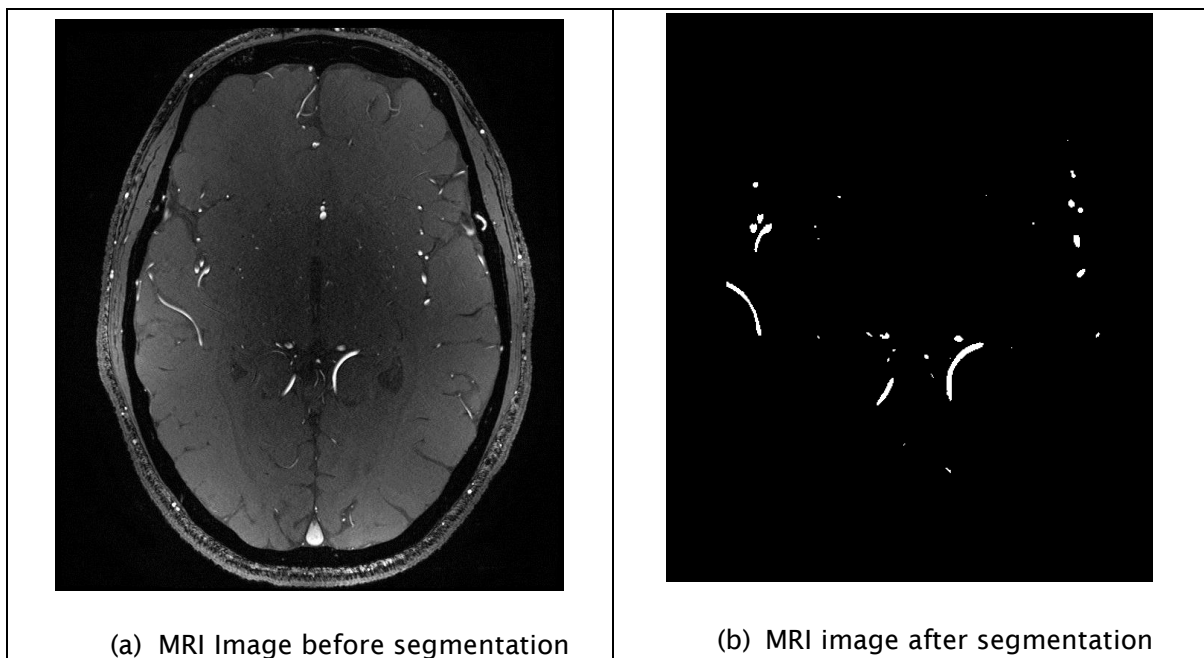


Figure 5-2. Comparison between original image and segmented image

In Figure 5-2, the segmentation of the brain is necessary to remove the skull, which has higher contrast than the main vessels. Although there are vessels in the skull, as shown in this figure, the vessels are considered not significant as our main interest is to extract the vessels in the centre of the brain. The view of manual segmentation is shown in Figure 5-3.

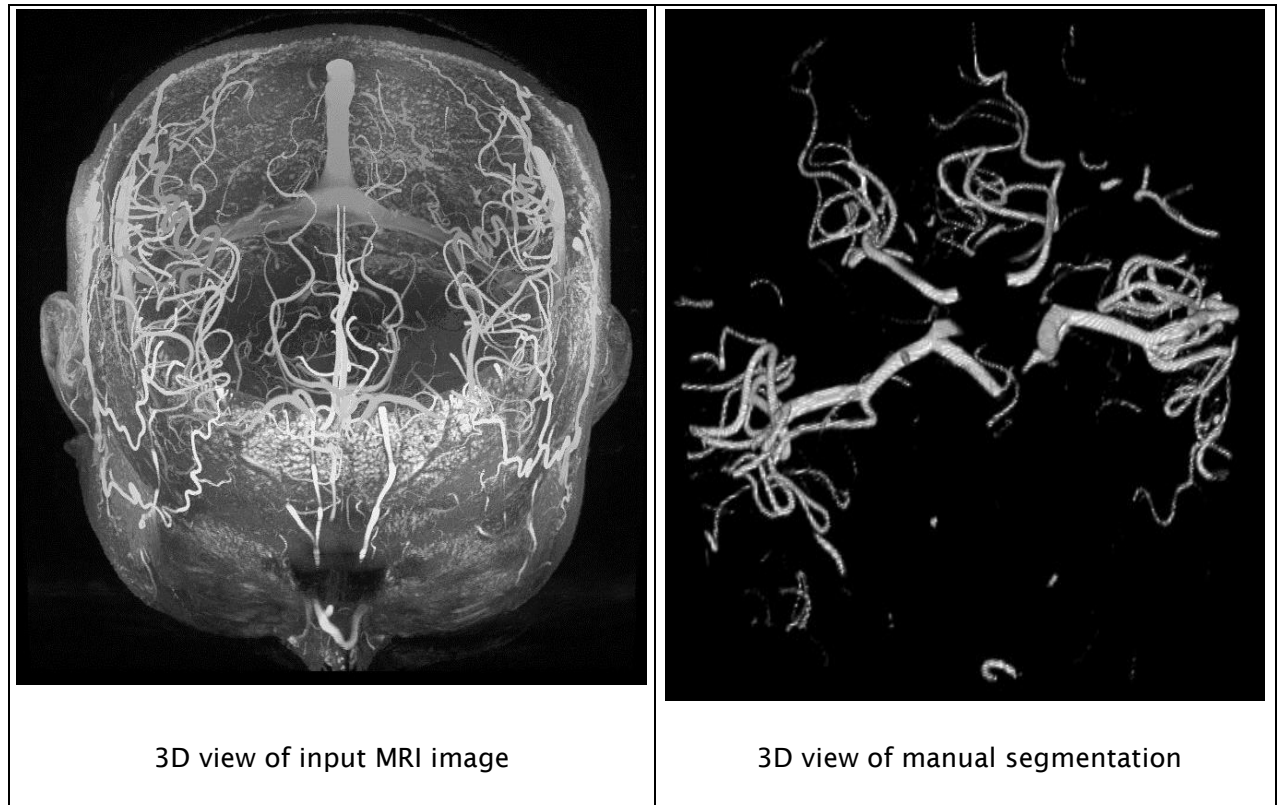


Figure 5-3. 3D view for 3D MRI images

## Skeletonisation

First, the images from the 2D stacked image are manually identified according to their type; anterior and posterior regions. Using a threshold value of 0.5, the images are converted to binary images. Next, the images are labelled, and, in order to find the features for later use, both regions are skeletonised using the thinning algorithm described by Kollmannsberger [92]. The skeletonised branches are shown in Figure 5-4.

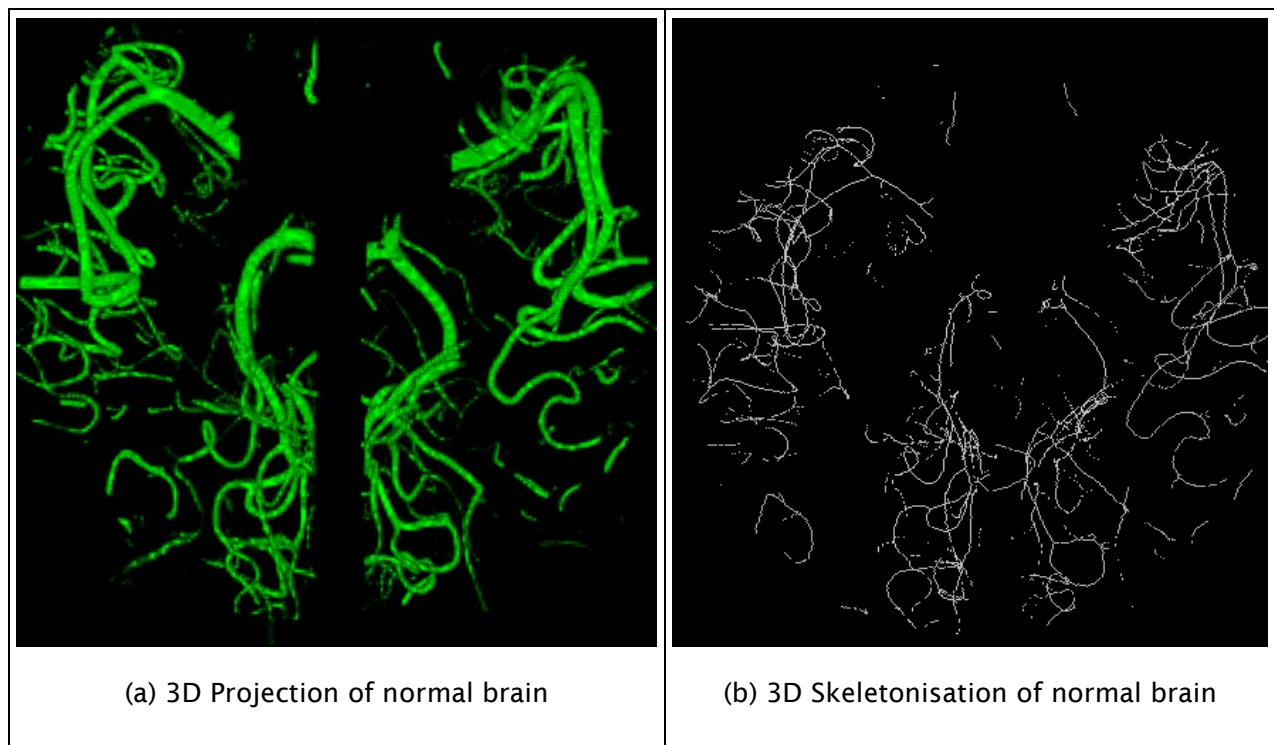


Figure 5-4. 3D Skeletonisation process in normal brain

## 5.2 3D Model-based Branching Structures

Our novel approach to analysing model based branching structures in capillaries showed a maximum capability of just over 60% CCR of AD from subjects with Young and Old brains. The model could be extended to a 3D approach aiming to improve reliability, and hence increasing the classification rate. For that purpose, in this section, the model is modified to suit the 3D environment and applied to MRI images to show the feature description capabilities of the new model.

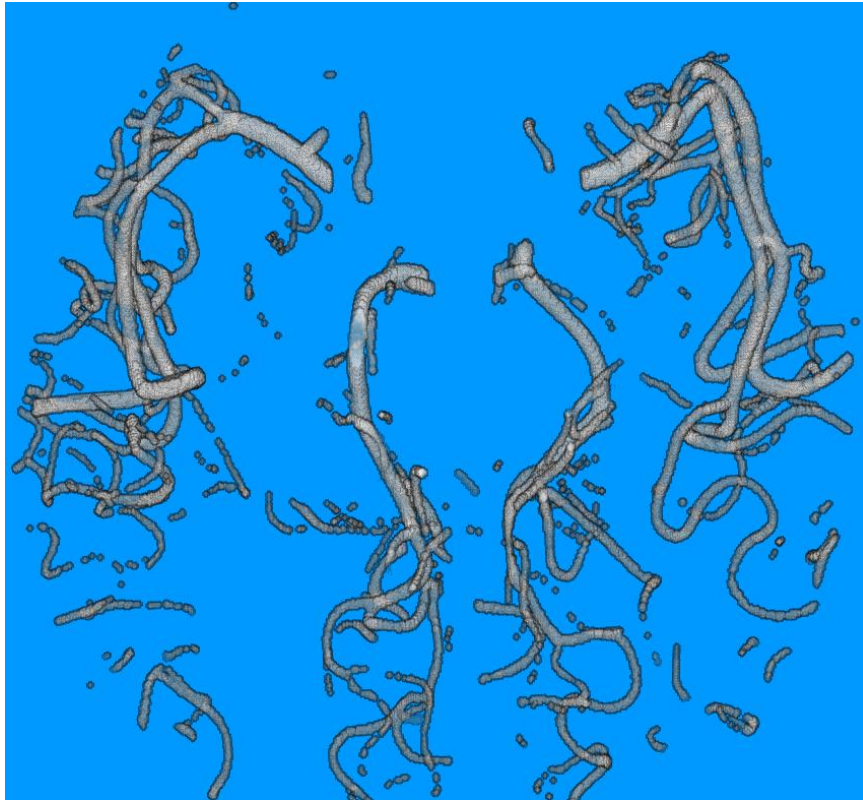


Figure 5-5. 3D Branching Structure for whole brain

### 5.2.1 Angle description

The angle in 3D should represent two component angles, as the perceived view will be different if the object is rotated. As we want to measure the angles with reference to the branch point, azimuth and elevation represent the angle in 3D coordinate systems. In simple words, elevation refers to the vertical angular measurement and the azimuth is to horizontal angle measurement (Figure 5-6).

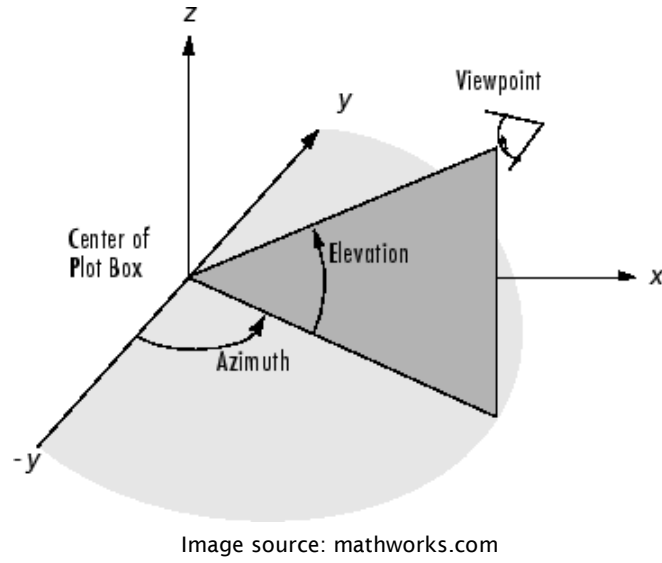


Figure 5-6. Comparison between Azimuth and Elevation angle

The angles of azimuth  $\theta$  and elevation  $\varphi$  are as follows,

$$\theta = \tan^{-1}(y, x) \quad (5-1)$$

$$\varphi = \tan^{-1}\left(z, \sqrt{x^2 + y^2}\right) \quad (5-2)$$

where the implementation is,

$$\text{atan2}(y, x) = \begin{cases} \tan^{-1} \frac{y}{x} & x > 0 \\ \tan^{-1} \frac{y}{x} + \pi & y \geq 0, x < 0 \\ \tan^{-1} \frac{y}{x} - \pi & y < 0, x < 0 \\ +\frac{\pi}{2} & y > 0, x = 0 \\ -\frac{\pi}{2} & y < 0, x = 0 \\ \text{undefined} & y = 0, x = 0 \end{cases} \quad (5-3)$$

### 5.2.2 Model Description

As the angle in 3D has two component angles, our branching structure equation from Eqn. 3-3 has to be modified by including the elevation angle  $\theta_E$  and the azimuth angle  $\theta_A$ . Therefore, we can define the equation by:

$$B_{cos} = \frac{\sum_{i=1, N, j=1, N} (L(i) + L(j)) \times \cos(\theta_A(i, j)) \times \cos(\theta_E(i, j))}{\sum_N L_N} \quad i \neq j \quad (5-4)$$

We then deployed this equation to five MRI volumes of normal brains (described in Section 0), to allow comparison of the posterior and anterior artery structures. These structures are segmented first as pre-processing procedure in Section 5.1.2 to extract branches and branch points in order to find their angle and the length. In order to find the branching point, the skeleton is converted into a network topology described by nodes, links and cells. Voxels with more than two neighbours were defined as a node or branching point, and voxels with two neighbours were defined as links or branches. All branches shorter than 10 voxels, all loops and isolated voxels were deleted. This algorithm was described by Kollmannsberger [92] .

## 5.3 3D Feature Detection

### 5.3.1 3D Tortuosity

Pathological modifications of vasculature can be an indicator of the existence of disease. The detection of the pathological changes in three-dimensional images could help the diagnosis of the disease in early stages. Tortuosity or the twistiness of the vasculature is a significant feature to detect the changes of the vasculature's network. An advanced technology, such as MRI and CT scans, cannot provide the user with direct information about the tortuosity of the vasculature as pre-processing has to be done before the feature can be detected and classified. In this section, we analyse the 3D tortuosity in MRI Images of normal subjects to find the differences between the posterior and anterior arteries of the brain.

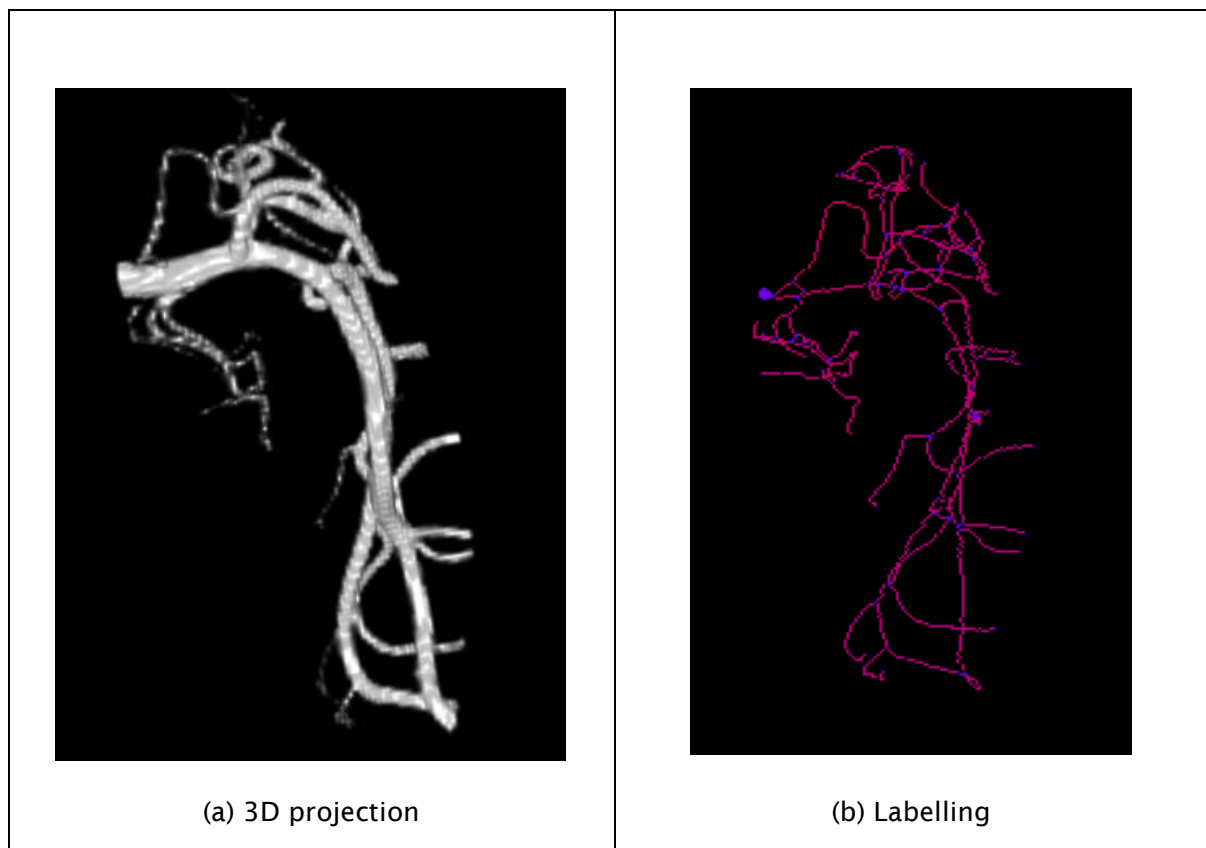


Figure 5-7. Preprocessing of 3D anterior artery

In order to find the tortuosity in the vessel, using the same equation in 2D tortuosity measurement described by  $= L/C$ , we had to extract the vessel's branching points and extract the branches from the vasculature as shown in Figure 5-7(a). This procedure of branch point extraction uses the same method



described in Section 5.2.2. In Figure 5-7(b) the branching points are depicted in blue and the branches in pink. The same process is shown for the posterior artery in Figure 5-8. The 3D tortuosity was then calculated by dividing the length of the branches (defined by the number of voxels) with the length between the two end points of the branches.

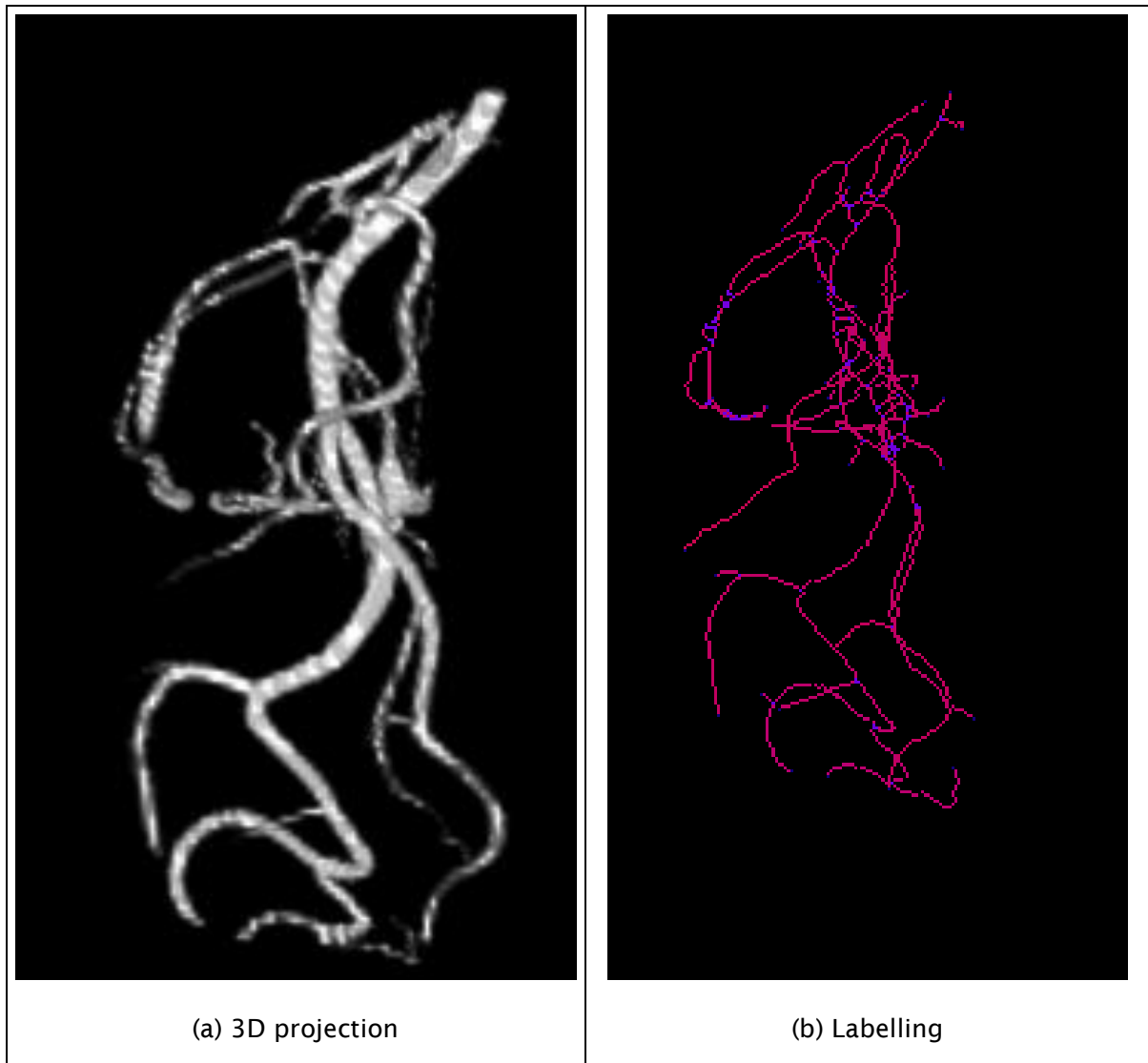


Figure 5-8. Preprocessing of 3D posterior artery

### 5.3.2 3D Compactness

#### 3D Classical Compactness

2D compactness shows high capability to classify objects, whilst the results of previous chapter demonstrated a higher rate compared to the other features in AD classification. The classical definition of compactness can easily be extended to 3D in which the most compact possible shape is a sphere, as in Equation (5-5) [39]:

$$C_{3D}(S) = \frac{36\pi \cdot Volume(S)^2}{Surface(S)^3} \quad (5-5)$$

In the context of this measure, compactness is unity for a sphere. In implementation however, this measure depends on the enclosing surface of the objects. In real volumes, most (discrete) objects have a noisy enclosing surface, which makes the measurement of compactness sensitive to noise. This factor could contribute to a lower classification rate when used for feature description. For that reason, we implement an existing measurement of compactness introduced by Bribiesca [74] to the new environment in the following section.

#### 3D Discrete Compactness

Discrete compactness has exhibited promising performance in AD classification from 2D images. 3D discrete compactness was introduced by Bribiesca to overcome the noisy enclosing surface of 3D objects in Equation 5-5. The measure of 3D discrete compactness  $C_D$  is defined by the ratio of contact surface area  $A_c$  to the maximum contact surface area  $A_{c_{max}}$  [72] as in Equation (5-6):

$$C_D = \frac{A_c}{A_{c_{max}}} \quad (5-6)$$

where  $A_c$  is defined by the contact surface area of a rigid solid composed of a finite number  $n$  voxels, obtained by the summation of the areas of the contact surfaces that are common to two voxels. For every voxel that is connected to another voxel, the summation of twice the contact surface area and the surface area  $A$  is the same as  $6n$  voxels since every voxel has six surfaces. Thus:

$$2A_c + A = 6an \quad (5-7)$$

Where  $n$  is the number of voxels and  $a$  is the area of the each voxel surface (in this analysis we assume  $a = 1$ ). For example, as in Figure 5-9(a), when one voxel connects to another voxel,

only one surface area is common to the two voxels. Hence, there is only one contact surface area for this case.

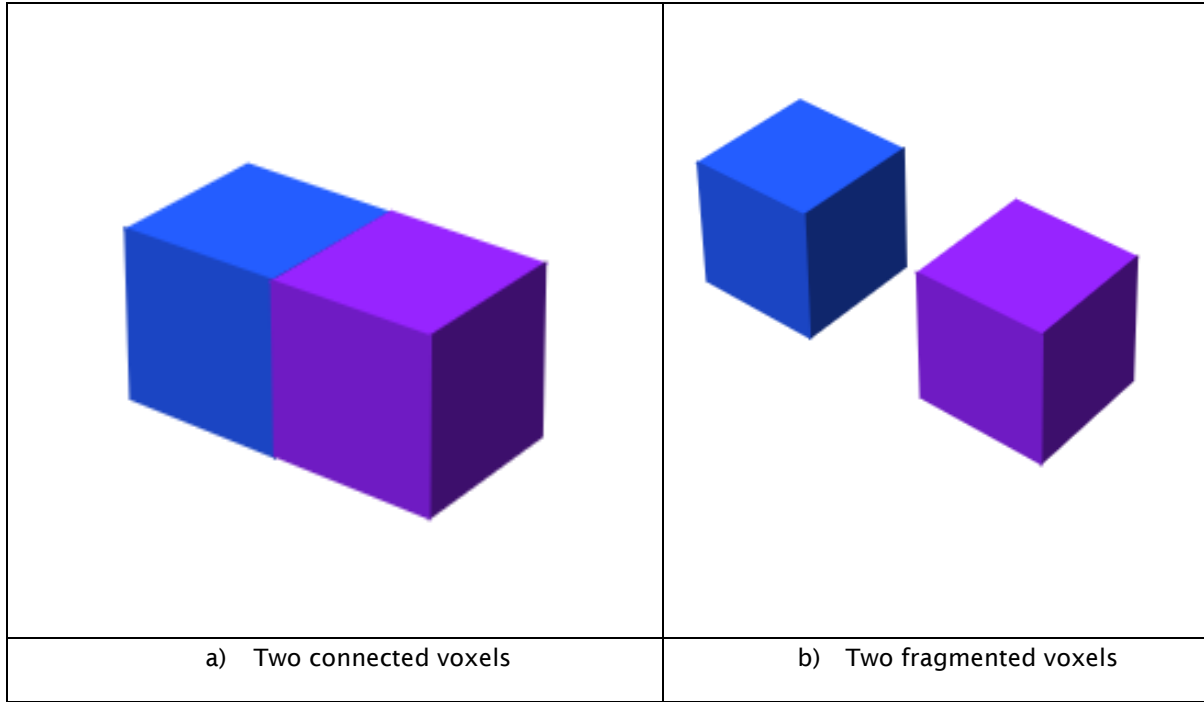


Figure 5-9. The understanding of contact surface area

By Equation (5-7), the contact surface area can be defined as follows:

$$A_c = 3(n - A/6) \quad (5-8)$$

given  $a=1$ . For maximum contact surface area,  $A_{c_{max}}$  for a shape composed of  $n$  voxels, where a perfect cube is defined by  $n = m^3$  where  $m$  is the length of the voxel's side. On the other hand, the surface area  $A$  can be defined as  $A_{max} = 6m^2$  for a perfect cube. By substituting these expression into Equation (5-8) and  $a=1$ , the definition of maximum contact surface in Equation (5-7) with  $a=1$ ,  $A_{c_{max}}$  can be expressed as:

$$A_{c_{max}} = 3(m^3 - m^2) \quad (5-9)$$

In conclusion, an approximation of  $A_{c_{max}}$  is given by:

$$A_{c_{max}} \approx 3 \left( n - (\sqrt[3]{n})^2 \right) \quad (5-10)$$

Finally, by substituting these equations into Equation (5-8) and (5-10) in Equation (5-6), the measurement of 3D compactness is obtained and expressed as below:

$$C_D = \frac{n - \frac{A}{6}}{n - (\sqrt[3]{n})^2} \quad (5-11)$$

where  $n$  is the number of voxels of the objects and  $A$  is the surface area of the objects. From the equation we can understand that the equation relies on the sum of the contact surface area of the face-connected voxels of objects which produces a more robust measure for noisy enclosing-surfaces. As such the capability of discrete compactness are compared with that of classical compactness for the discrimination of anterior vs posterior arteries.

### 5.3.3 3D Fourier Descriptors

Unlike 2D FDs (that used boundary extraction), 3D FDs uses another feature to represent the objects for description. One of the ways is to use the surface representation to create the Fourier coefficients from the images. First, the binary objects are converted to a polygon mesh, which is basically a group of 2D polygons (in this case triangles) that are all connected together to create a 3D object. Figure 5-10 shows the triangle mesh for the anterior artery.

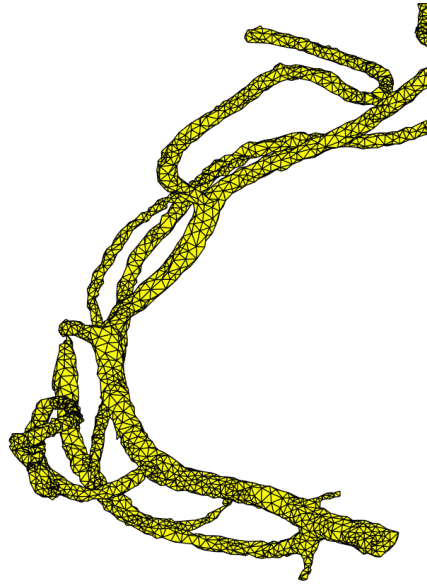


Figure 5-10. 3D anterior arteries represented as a mesh of 2D triangles

Many 3D FDs have been applied in 3D object retrieval including a work done by Vranic [76] who described a technique with low complexity and computational cost. Vranic introduced a bounding box, which refers to the tightest cube surrounding the normalised object. A normalisation process was used so as to determine 3D descriptors that are invariant to position, rotation and scale. Vranic's method for rotation invariance used Principal Components Analysis (PCA) to determine the canonical coordinate system axes of a 3D model by calculating the corresponding eigenvectors and eigenvalues. The covariance matrix is obtained in order to extract the eigenvectors and eigenvalues. Subsequently, the eigenvalues are re-arranged in decreasing order to indicate the most important factor. In our work, Vranic's method was implemented for translation and scaling where the mesh was translated into a voxel structure. The FDs were derived by Fourier transformation of normalised object's voxel coordinates and classified using the  $k$ -NN approach in order to compare the posterior with anterior arteries. The process of 3D FDs is illustrated in Figure 5-11.

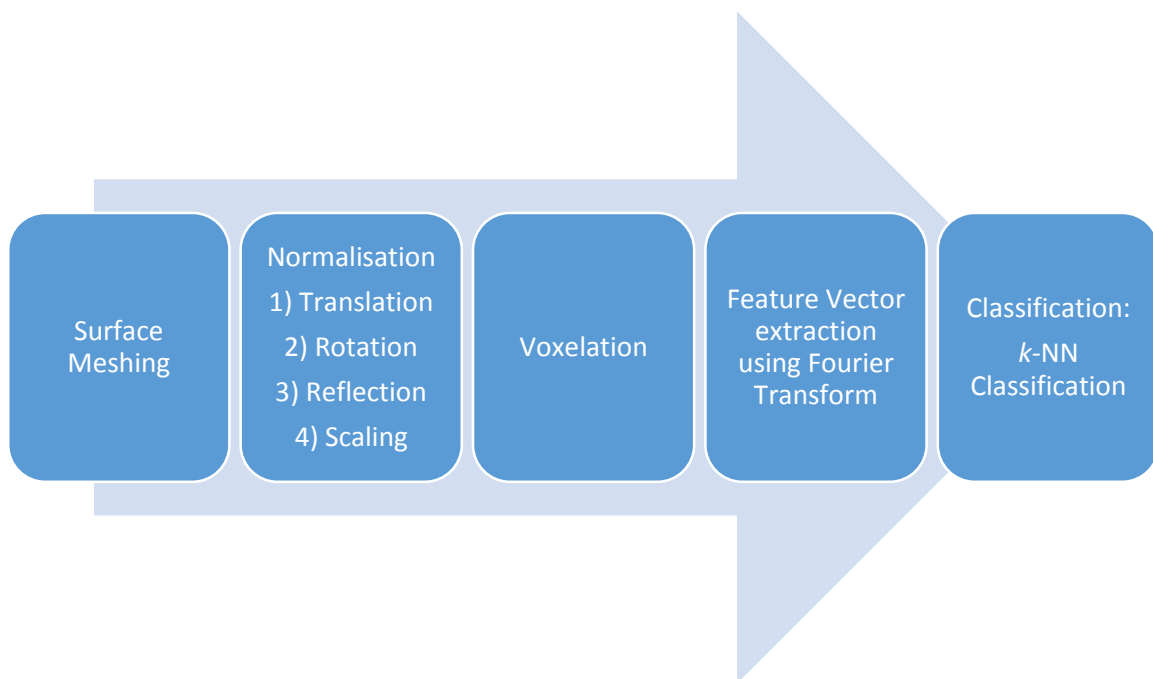


Figure 5-11. Flowchart of 3D FDs Algorithm

## 5.4 Analysis of 3D Features

As previously mentioned in Section 2.3, our analysis was conducted using five images acquired from 7T MRI from five subjects of normal groups. These images consist of 219 frames where each image is segmented using morphological operations and the vessels are labelled for the 26-connected components in binary images using Matlab function *bwlabeln*. Each subject's image will consists of 4 blood vessels which are the right and left anterior and the right and left posterior. This is added up to total 20 vessels which are 10 anterior and 10 posterior. The labelled vessels are then used for the analysis of the different features in order to assess its feature capability for discrimination and to assess the classification accuracy of these features.

### 5.4.1 Analysis of 3D Model-based Branching Structure

For our investigation in 3D, different types of Branching Structure were analysed using independent *t*-test to find its statistical significances difference between the features computed for the anterior and posterior. If the test shows there is a significant difference, it means that the posterior structure is different from the anterior. Thus, there is probability that the accumulation of amyloid beta has occurred only on the posterior vasculature and not the anterior.

Independent Samples Test

		Levene's Test for Equality of Variances		t-test for Equality of Means						
		F	Sig.	t	df	Sig. (2-tailed)	Mean Difference	Std. Error Difference	90% Confidence Interval of the Difference	
									Lower	Upper
Cosine	Equal variances assumed	.761	.395	3.287	18.000	.004	.076	.023	.036	.117
	Equal variances not assumed			3.287	15.710	.005	.076	.023	.036	.117
Degree	Equal variances assumed	.102	.753	.855	18.000	.404	928.176	1085.098	-953.453	2809.805
	Equal variances not assumed			.855	16.391	.405	928.176	1085.098	-963.511	2819.864

Table 5-1. Result of Independent Sample *t*-test of different measurement of 3D Branching Structure

As shown in Table 5-1, the  $p$ -value for 3D Cosine Branching Structure is 0.004 and there is significant difference at the  $p<0.1$  level between anterior and posterior (Cosine-based Branching Structure has equal variances when tested using Levene's Test). However, the Degree-based Branching Structure exceeded the significant level of  $p=0.1$  as having  $p$ -value of 0.404. Thus, there is no statistically significant difference between the groups by using Degree-based Branching Structure.

**Independent Samples Test**

		Levene's Test for Equality of Variances		t-test for Equality of Means						
		F	Sig.	t	df	Sig. (2-tailed)	Mean Difference	Std. Error Difference	90% Confidence Interval of the Difference	
									Lower	Upper
Cosine	Equal variances assumed	.761	.395	3.287	18.000	.004	.076	.023	.036	.117
	Equal variances not assumed			3.287	15.710	.005	.076	.023	.036	.117
Degree	Equal variances assumed	.102	.753	.855	18.000	.404	928.176	1085.098	-953.453	2809.805
	Equal variances not assumed			.855	16.391	.405	928.176	1085.098	-963.511	2819.864

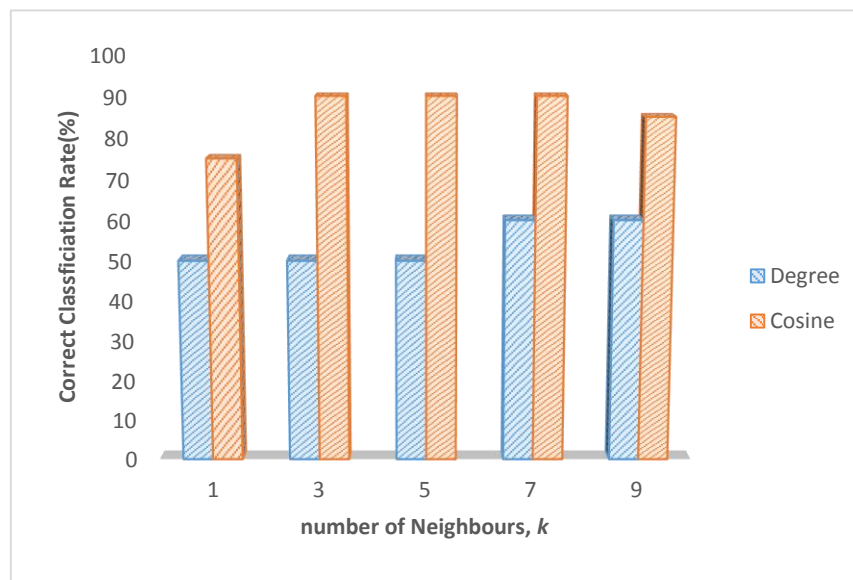


Figure 5-12. CCR using 3D Branching Structure measures

Next, the measurement using degrees was compared with the measurement using cosine function using LOOCV of  $k$ -NN classification as shown in Figure 5-12. By applying the cosine function, a higher CCR of 90 per cent was the most significant classification achieved here. Clearly in both analyses, the Cosine Branching Structure shows good capability to become a feature and classify the groups. The feature also means that the blood vessels description is associated with angle and the length of the vessels. Hence, the cosine-based branching structure was chosen for the 3D feature description of the blood vessels. Future works particularly on automatic pre-processing and extending the formula may increase the classification capability of this feature.

#### 5.4.2 Analysis of 3D Tortuosity

For the next analysis, statistical significant difference of tortuosity between groups is analysed using independent sample  $t$ -test. As depicted in Table 5-2,  $p$ -value for tortuosity measurement is higher than significant level of  $p=0.1$  which is 0.616 and hence there is no significant difference of tortuosity between posterior and anterior. This proves that in there are not much differences in tortuosity at large artery level. Furthermore, the accumulation of amyloid beta, which is the reason of AD, is starts to take place only in the cortices of the brain.

Independent Samples Test									
		Levene's Test for Equality of Variances		$t$ -test for Equality of Means					
								90% Confidence Interval of the Difference	
		F	Sig.	$t$	df	Sig. (2-tailed)	Mean Difference	Std. Error Difference	
Tortuosity	Equal variances assumed	.650	.431	.510	18.000	.616	.013	.026	-.032 .059
	Equal variances not assumed			.510	17.672	.616	.013	.026	-.032 .059

Table 5-2. Result of Independent Sample  $t$ -test for 3D Tortuosity

Subsequently, the tortuosity is classified using  $k$ -NN classification and the accuracy of the classifier is tested using LOOCV. The result of 3D tortuosity only achieved at best CCR at  $k=1$  with 65% and then decreased with increasing the number of neighbours,  $k$ . When  $k$  are 3, 5, 7 and 9, the CCR is lower than the random rate.



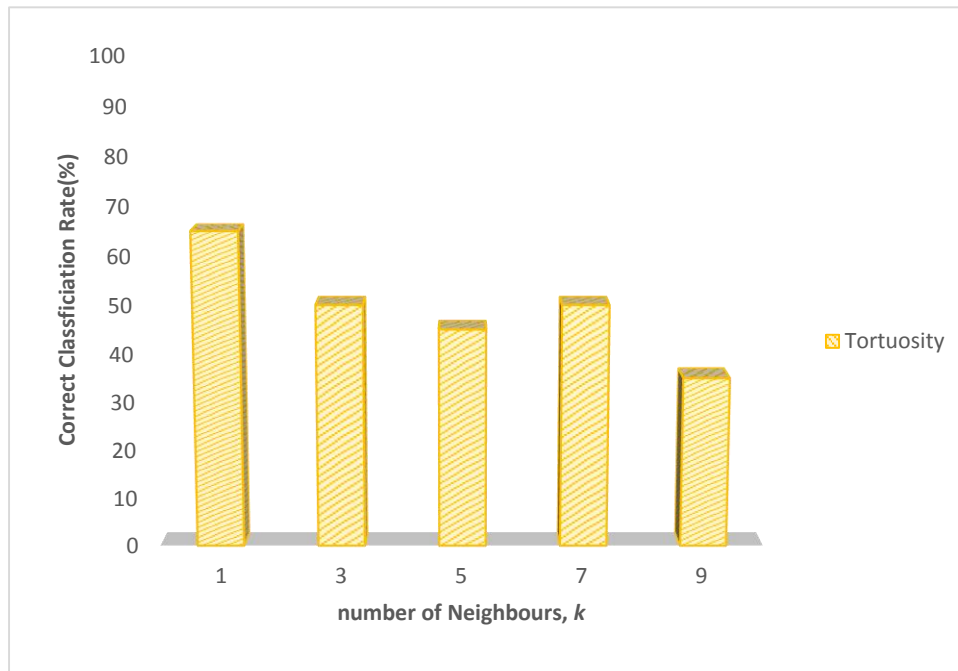


Figure 5-13. Recognition of Anterior vs Posterior Vessels by Tortuosity

### 5.4.3 Analysis of 3D Compactness

In order to determine the best method to be used for classification, the measurement of 3D discrete compactness was compared with classical 3D compactness using independent samples  $t$ -test and  $k$ -NN classification. As shown in Table 5-3, independent sample  $t$ -test is analysed between Discrete Compactness and Classical Compactness. For Discrete Compactness, there is highly significant difference between anterior and posterior with  $p$ -value less than 0.001 at significant level  $p < 0.1$ . However, there is no significant difference ( $p=0.772$ ) for Classical Compactness between each group at significant level  $p < 0.1$ . Thus, discrete compactness shows good discrimination capability for anterior and posterior.

Independent Samples Test										
		Levene's Test for Equality of Variances		t-test for Equality of Means						
		F	Sig.	t	df	Sig. (2-tailed)	Mean Difference	Std. Error Difference	90% Confidence Interval of the Difference	
									Lower	Upper
Discrete	Equal variances assumed	.853	.368	4.587	18.000	.000	.051	.011	.032	.070
	Equal variances not assumed			4.587	16.319	.000	.051	.011	.031	.070
Classical	Equal variances assumed	1.196	.288	.294	18.000	.772	.138	.469	-.676	.951
	Equal variances not assumed			.294	15.808	.773	.138	.469	-.682	.957

Table 5-3. Result of Independent Sample *t*-test of different measurement of 3D Compactness

Figure 5-14 presents the CCR using a *k*-NN classifier which was employed to compare the classical compactness against discrete compactness. It is noted that a higher classification rate was obtained using discrete compactness, whereas, classical compactness is lower than a random choice. This is due to the measurement of classical compactness, which is based on surface area that is prone to noise, where the results confirm the ambiguity of the classical compactness measured in 3D. Henceforward, discrete compactness is used in our feature description of vessels in 3D MRI.

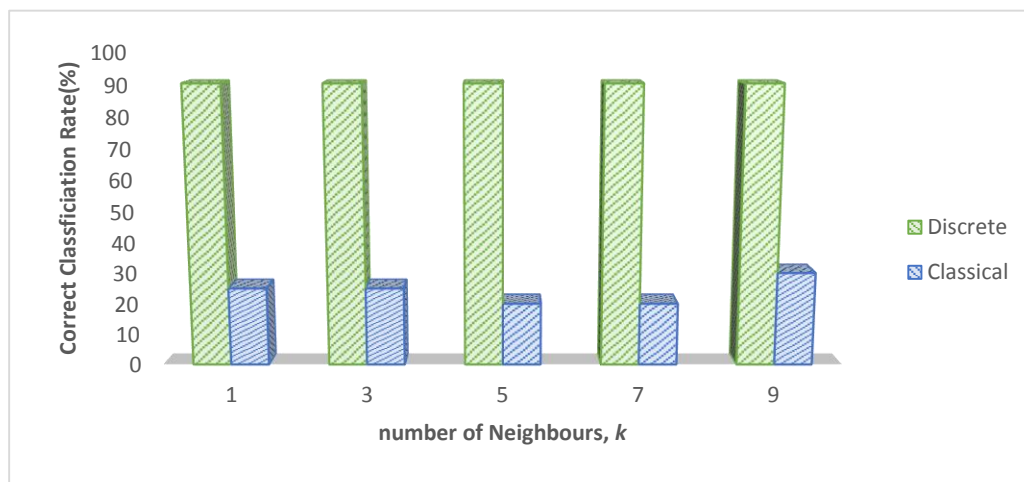


Figure 5-14. CCR using 3D compactness measures

#### 5.4.4 Analysis of 3D Fourier Descriptor

As the Fourier Descriptor uses coefficients as vectors for features, we are unable to perform *t*-test for this feature as this test only requires one variable to test. Therefore, we proceeded with our test to find the CCR using LOOCV of *k*-NN classification. High classification rate achieved for 3D Fourier Descriptor as CCR for *k*=7 and 9 was 85%.

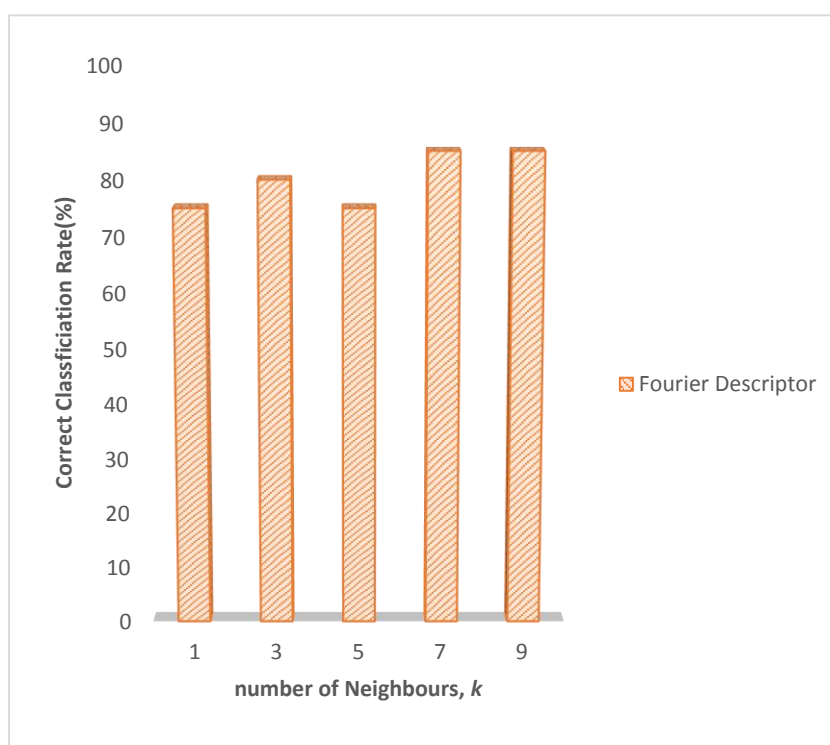


Figure 5-15. CCR using 3D Fourier Descriptor

Environment	Comparison	Best three coefficients using SFFS
2D Environment	Compare Young with Old	1 <sup>st</sup> , 2 <sup>nd</sup> and 4 <sup>th</sup>
	Compare Old with AD	2 <sup>nd</sup> , 3 <sup>rd</sup> and 4 <sup>th</sup>
	Compare Young with AD	2 <sup>nd</sup> , 3 <sup>rd</sup> and 4 <sup>th</sup>
3D Environment	Compare Anterior with Posterior	2 <sup>nd</sup> , 3 <sup>rd</sup> and 6 <sup>th</sup>

Table 5-4 Result of SFFS for Fourier descriptors

For an in-depth analysis of FDs to investigate its contribution in our research, the Sequential Floating Feature Search (SFFS) technique [93] was used to find the best three FDs. Surprisingly, the results in the Table 5-4 that were obtained from the SFFS for both in 2D and 3D environment, show that the best feature overall features is in the lower order descriptors. The table shows that the second FD is consistently selected as one of the most important features for recognition. FDs show reliability for shape differentiation of an object, and therefore the classification by using this feature is much higher compared to other features. Fascinatingly, FDs shows a remarkable performance confirming that deeper analysis of this technique is well justified.

The FDs is usually used for object retrieval and object enhancement as one of its properties is to improve the smoothness of the objects, hence the object could be easily matched by other objects. Interestingly, by using FDs for classification, the significant value obtained shows that the method is suited to these classifications.

## 5.5 Results and Discussion

This part contains all the analyses associated with classification from all 3D methods in order to discriminate the posterior and anterior vasculature. Initially, the classification was performed using  $k$ -NN classification in order to determine the CCR for those methods. We then used LOOCV which is a well-established technique for the evaluation of small datasets. In other words, we selected one image from the dataset to be tested the image and the rest became the training set for that classification. All features were derived from all volumes in precisely the same way, with the same parameter settings.

For summary, the structures from the anterior and posterior parts of the brain were compared using the Branching Structure, FDs, Tortuosity, and Compactness. Unlike the 2D classification, this does not include the density as the segmentation was executed manually and the segmented vessels did not contain all the branches. Our classification was performed using  $k$ -NN classification on four features in order to find the CCR obtained from LOOCV. For the overall section, we used  $k=1, 3, 5, 7$  and  $9$  as the maximum number of every group is 10.

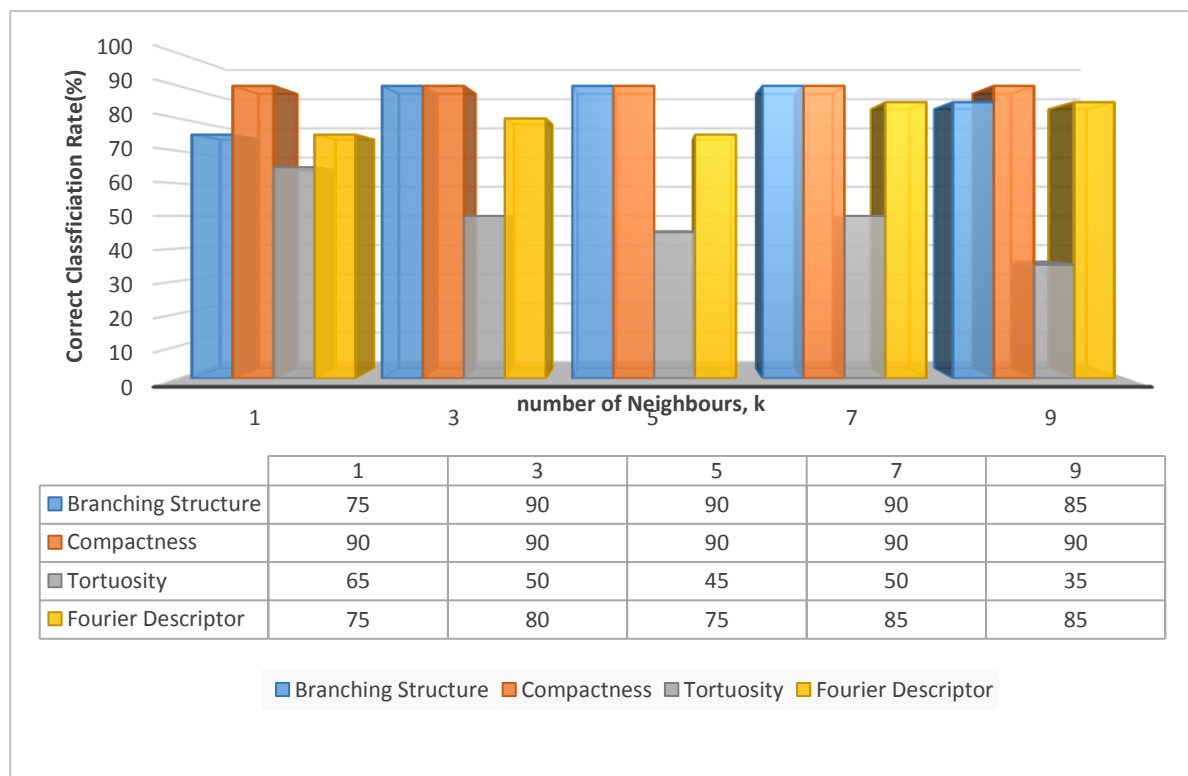


Figure 5-16. CCR for different features of 3D

In Figure 5-16, Branching Structure and Compactness shows a high CCR of 90% with an increasing number of neighbours. This is followed by FDs which obtained at best of 85% CCR and was largely attributed to the high number of coefficients used in FDs.

The branching structure has a CCR of 90%, which suggests the reliability of this method for to be used as a feature description (and with better capability than was observed for 2D images). A better description of the bifurcation ratio of the branch could improve the overall description, and hence, CCR could be increased. Thus, a deeper understanding of the branching structure of the vessels is necessary. This novel algorithm of branching structure could reveal new knowledge of the branching structure in medical understanding.

Tortuosity appeared to be 65% CCR for  $k=1$  and decreased with increasing number of neighbours. Tortuosity on average showed the lowest CCR. Even though the results of tortuosity on average showed the lowest CCR, this could be one of the reasons that the accumulation of A $\beta$  of AD does not happen in larger vessels and just happens at the capillary level, suggesting a deeper understanding is needed of tortuosity and the pathology of the vessels in the brain. Naturally, lack of recognition capability could imply that either this feature has no discriminatory capability or that the measure of this feature is inappropriate (or both).

The compactness feature showed robust recognition with 90 per cent accuracy, and hence this feature could provide new knowledge towards medical understanding of vessel shapes. We suspect that the compactness measure could also describe the flow efficiency of a vessel. The higher compactness the vessel has, the better the blood flow becomes. Thus, the accumulation of A $\beta$  in the posterior vasculature could be caused by the inefficiency of the blood flow in those regions. This is reflected by the results that showed lower compactness for the posterior vasculature when compared to anterior vasculature.

Even though, the result of FDs showed a high CCR of 85%, the meaning of the coefficients derived by FDs is not yet established in medical knowledge. However, in computer vision, the FDs could be used to define the shape as it defined the boundary for the 2D environment and the surface in the 3D environment. Furthermore, the measurement of the boundary and the surface is also included as one parameter to find compactness. Thus, using FDs also contributes to the knowledge of the blood vessel's shape and the efficiency of the blood flow.

Clearly for the future, branching structure, compactness and FDs could be applied to compare AD with normal brain in 3D environment. The feature description for 3D also could be extended by including the density measurement as automatic segmentation can be implemented in future. This result can be further improved by increasing the dataset in such a way the anterior vasculature can be differentiated from the posterior vasculature using these features.

## 5.6 Conclusion

For overall analysis on 3D environment using 7T MRI images, we can conclude that the classification rates for 3D is high. As this environment included all the 3D spaces  $(x, y, z)$  in the analysis, the vessels are 3D structures rather than planar 2D tissue images.

Firstly the new branching structure measurement is analysed in 3D. By implying this feature, there is significant different between anterior and posterior. It is supported by the high classification rate for the branching structure achieved in this analysis. Our measurement featuring the branching angle is defined in azimuth and elevation in 3D to measure the branching structure. The measurement of tortuosity in 3D is applied to the posterior and anterior arteries. Fair classification rates are achieved suggesting the similarity of tortuosity between posterior and anterior arteries.

Following tortuosity, the dissimilarity of compactness is studied between posterior and anterior vasculature using different measurements of discrete and classical compactness. A higher classification rate was achieved by discrete compactness compared to the classical approach. It also reinforces our conclusions in the previous chapter that the compactness indicates the smoothness of the blood flow in the vessels. This argument can also be extended to the definition of tortuosity as the tortuosity of the vessels is defined to smoothness of the vessels.

The last analysis of this chapter is 3D Fourier Descriptors comparing the posterior with anterior vasculature. The whole structure of the vessels is analysed in 3D FDs ensuring a good classification rate as this approach involving Fourier coefficients. By using these coefficients, we can describe the irregularity of vessels more accurately.

## 6. Conclusions and Future Work

### 6.1 Overall Conclusions

The formation of plaques and tangles in bloodvessels is due to the failure to eliminate the amyloid beta, which, hence, modifies the vascular network in the human brain. Research has found that while slight changes are detected in aging, severe vascular modifications are detected in AD. Furthermore, the formation of new vessels called angiogenesis, which is triggered by amyloid beta that also occurs in the AD. Angiogenesis disrupts the natural structure of the brain, which causes the changes in the vessel network. Thus, by quantifying changes in the blood vessels of the brain, angiogenesis might be identified as a consequence or a contributory factor to AD.

Our study uses for the first time computer vision techniques together with statistical approaches for the assessment of blood vessels characteristics that may be used to aid in early detection of AD. The analyses were achieved automatically using the combination of established and new computer vision techniques, such as Fourier descriptors, compactness, tortuosity and branching structure. A new approach has been developed to determine branching structure by medial distance analysis that can be used to analyse shape topology. The analysis of branching structure can be deployed in other forms of cell analysis and is considered a radical new approach to analysing shape to differentiate between tissue samples derived from subjects known to be affected or not by AD.

In order to test the first hypothesis of this study, immunocytochemistry and novel software quantification methods were employed to compare the histological pattern of vascular basement membrane components in brains with AD compared to normal brains of similar ages. A new reliable tool for quantifying the immunohistochemical changes in human cerebrovascular basement membranes was demonstrated via image processing techniques associated with the analysis of branching structures. This study confirmed by using machine learning techniques such as  $k$ -NN classification and leave-one-out cross validation and validated using statistical approaches such as ANOVA, Tukey HSD and a contrast analysis. Thus, the density, compactness and tortuosity can be measured and these features can be used for discriminating AD with Young and Old subjects. Neuropathological studies on post-mortem human tissue have described that the small vessels of aged brains are more tortuous compared to Young brains and tortuosity increases



with the presence of AD pathology. Furthermore, experimental studies using transgenic mice that develop AD's pathology demonstrated that tortuosity increases with deposition of A $\beta$  in the walls of arteries. The increase in tortuosity of the small vessels was associated with a change in the geometry and biochemistry of the cerebrovascular basement membranes that represent clearance pathways for A $\beta$ . This indeed resulted in a failure of perivascular drainage of A $\beta$  and its accumulation in the walls of vessels as CAA.

The measurement of Fourier descriptors to differentiate the AD with other subjects is uncommon as Fourier descriptor is generally used for object recognition. High classification rates were achieved by applying the measures, indicating thereby its importance for discrimination of AD.

Actually, the application of computer vision analysis to MRI-Angiograms is deemed nascent. Due to the invasive nature of angiography which requires an intravenous tracer to highlight the vasculature, the number of patients used in this study was limited. Patients with AD were not used, as the primary aim of our study was to develop the techniques necessary for extracting the compactness features, tortuosity branching structure and Fourier descriptors. The comparison between the features of the vessels of the posterior circulation (associated with high A $\beta$ ) and anterior circulation (low A $\beta$ ) was the second target of our study. Patients with AD had blood vessels that are susceptible to rupture and hemorrhages, which necessitate proper administration and stringent control over the intravenous tracer.

This study has demonstrated that it is possible to apply the computer vision techniques of identifying features of 3D compactness, 3D tortuosity, 3D branching structure and 3D Fourier descriptor to vessels of the posterior and anterior circulation as identified on MRI images. Compactness is a feature demonstrating the ratio of perimeter to area. Anterior vessels are more compact compared to posterior vessels. This suggests that blood flow in the anterior circulation is faster in vessels of the anterior circulation compared to vessels of the posterior circulation. As the motivating force for perivascular drainage appears to be derived from the amplitude of the pulsatile forces in the vessel and the degree of deformation of the wall of the basement membranes, a faster blood flow may be associated with more efficient perivascular clearance. Furthermore, a more efficient blood flow to the cortex is associated with a better perfusion of the cortical tissue, slowing the neurodegenerative processes.

The discrimination of tortuosity of the anterior and posterior can be achieved by simple calculation of tortuosity. This may be a significant factor in AD, with the accumulation of A $\beta$  in artery walls are more affected in posterior circulation. However, low discriminant capability of tortuosity between posterior and anterior might be one of the reasons the accumulation of A $\beta$  of AD in larger vessels does not happen and it only occurs at the capillary level (cortices) instead.

The branching patterns differ between anterior and posterior arteries. This may likely affect the geometry of the basement membranes and the efficiency of perivascular clearance of A $\beta$  along them. It is technically difficult to study the cerebrovascular basement membranes, as they are buried deep in the walls of arteries, and therefore considered inaccessible. The arrangement of the basement membranes at branching points is yet to be determined. Mathematical studies showed that the symmetrical branching pattern for vessels was more efficient for perivascular drainage of A $\beta$ . As the perivascular drainage of solutes advanced along the narrow 100nm thick basement membranes within the walls of capillaries and then arteries, it becomes so important to establish the morphological changes of the basement membranes in relation to the morphological features of arteries for better apprehension the pathogenesis of CAA and AD's.

In summary, this study has developed novel computer vision techniques for the assessment of the features of small vessels on histological images, as well as for the assessment of angiographic large arteries at the brain. The features derived from the measurement of compactness, tortuosity, Fourier descriptor and branching structure showed discrimination capability in both 2D and 3D environments. This indeed may help in identifying patients with risk of AD for whom early therapies may be beneficial.

## 6.2 Future Work

In future, we will focus on improving the measurement of this novel method for deeper understanding of bifurcation ratio of the branching structure. Furthermore, we will develop an automatic segmentation of 3D images that could improve the quality of our features and to increase the computational cost of the process. By using automatic segmentation of 3D images, we shall also investigate the determination and description of branching structures in greater depth.

Based on the promising initial result of our analysis in 3D, hopefully we could obtain AD images via MRI, therefore applying our feature descriptions for AD. By applying these features to AD, the detection capability of AD could be investigated and provide new knowledge of AD detection in early stages. Equally, our new features are well suited to the study of classifier fusion, with potential improvement in performance by selecting the best set of features for accurate discrimination. We can also improve the classification performance by applying different weights to every feature.

For each feature used in this study, there are several improvements that can be made to increase the feature discrimination capability. The measurement of tortuosity could be improved in many ways, such as the implementation of discrete compactness in the tortuosity measurement. In this study, we had discovered that by using discrete compactness to find the measure of compactness is quite promising. Since the equation employed on the discrete measurement based on square/cube as every images are made of pixels (2D) and voxels (3D), the noise from the measurement was expected to be much lower than other measurement which are based on simple mathematics equation by neglecting the digitisation condition of images in 2D and 3D. In this case, the compactness could become the measure of tortuosity if the diameter of the branches are the same, such as in a skeleton condition. Since discrete compactness is defined by the number of times pixels are adjacent, the higher compactness of the object is influenced by the higher number of times when pixels are adjacent. Hence, it also can be defined to reflect lower tortuosity of the objects.

Another area of improvement could be the ability to extract the branch angle and length to find the appropriate branching structure. The common use of skeletisation is to find their branching structure measurement and can be improved by using another method such as Hough transform to achieve the desired measurement. The Hough transform could improve the branching structure

measurements as the skeletonisation process is prone to noise with high possibility of mislabelling branches which would not occur with the Hough transform.

FDs are considered as one of the most accurate measurement for shape recognition in computer vision and application in medical approach especially in AD analysis. Since the technique has not yet been established in this area, expansion of the method to improve the classification rate is required. The descriptors of the whole vessel in our 3D analysis could be extended to singular vessel analysis. Furthermore, the FDs analysis between AD and other brain diseases could help to define the AD descriptors in medical applications. As the brain is a complex system that has not yet been fully understood, this descriptor could be also applied to other structures in the brain such as the corpus and medulla oblongata.

Furthermore, this study can be extended to analyse the blood vessels in other parts of the human body including the blood vessels in the heart and in the retina to find the similarity and dissimilarity for branches for different parts of the human body. It would be useful to detect AD using the retina as it is easier to analyse and access than the human brain. The application of this study could be extended into different kinds of diseases that affect the brain such as high blood pressure, trauma, diabetes, cancer and other dementia. The discrimination between each disease could be analysed. As such, the new techniques have shown capability for the detection of AD in vitro, and of discriminating between anterior and posterior vasculature and have capability for extension to other application domains.

## Appendix A

### Human tissue images

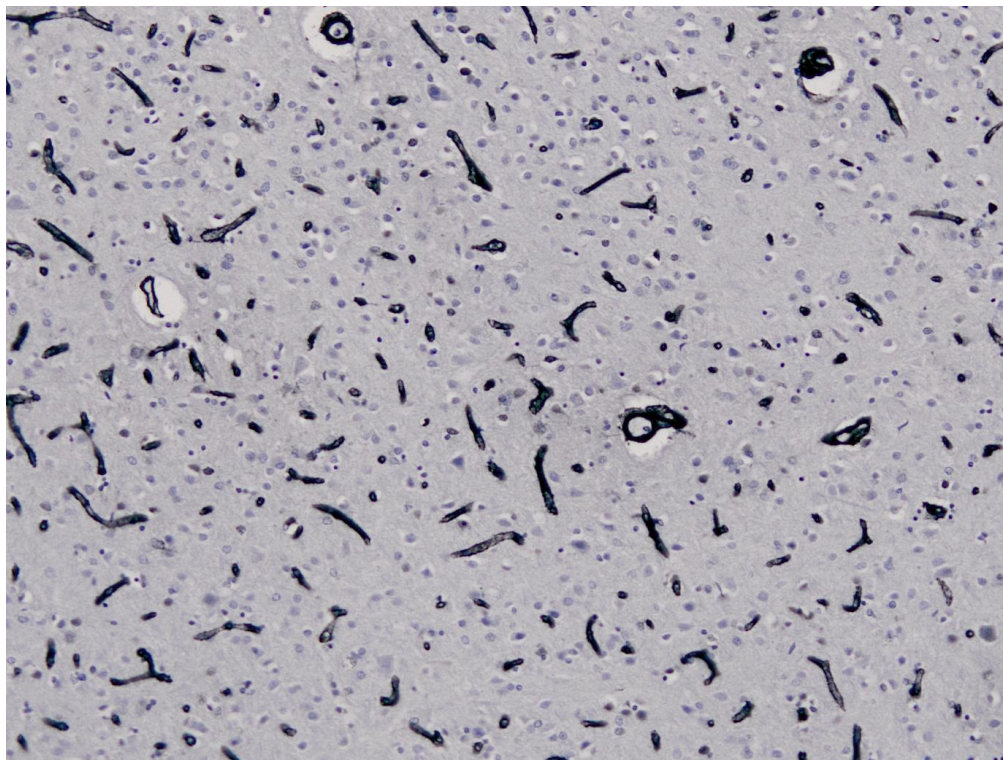


Figure A-1. Human tissue image of AD subject 1



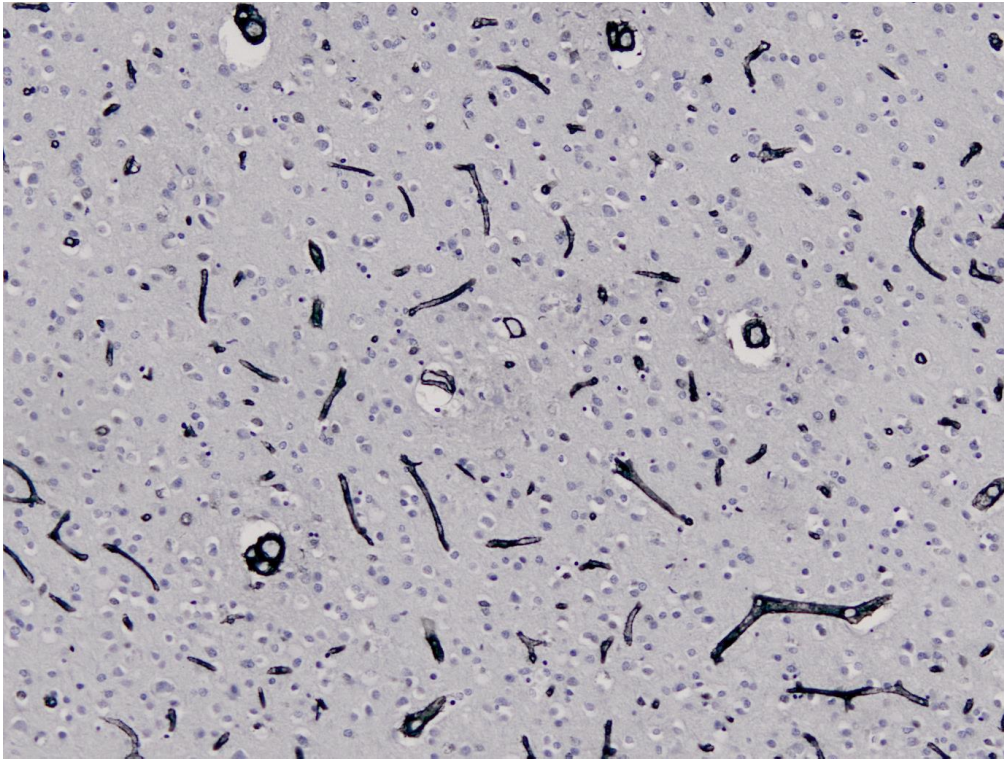


Figure A-2. Human tissue image of AD subject 2

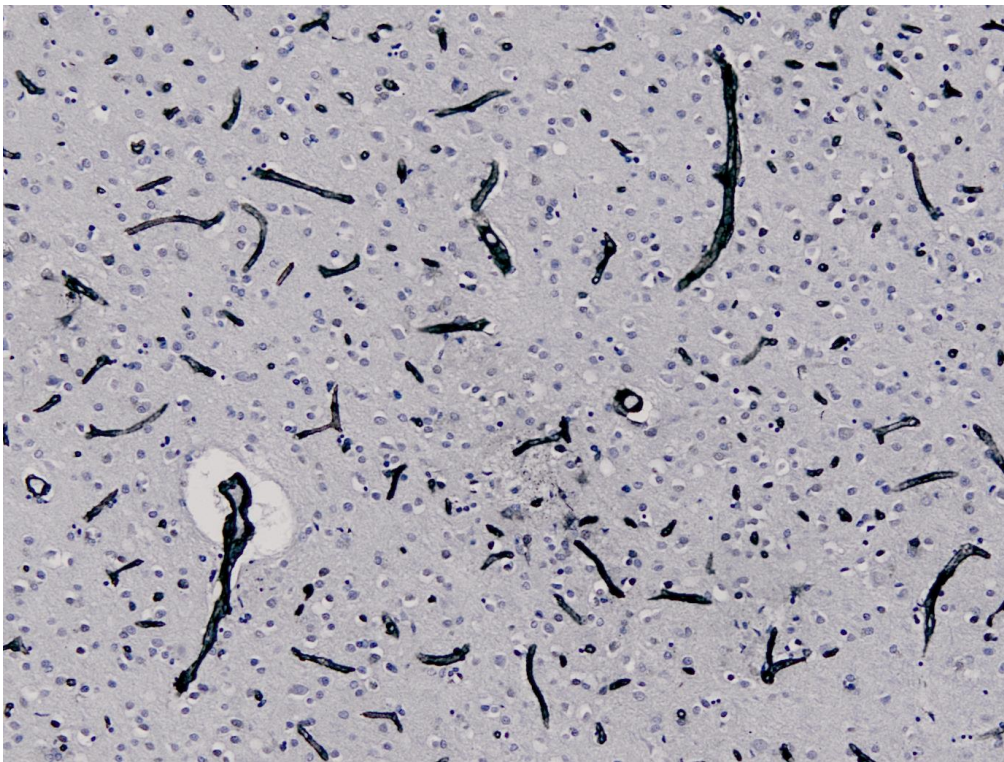


Figure A-3. Human tissue image of AD subject 3



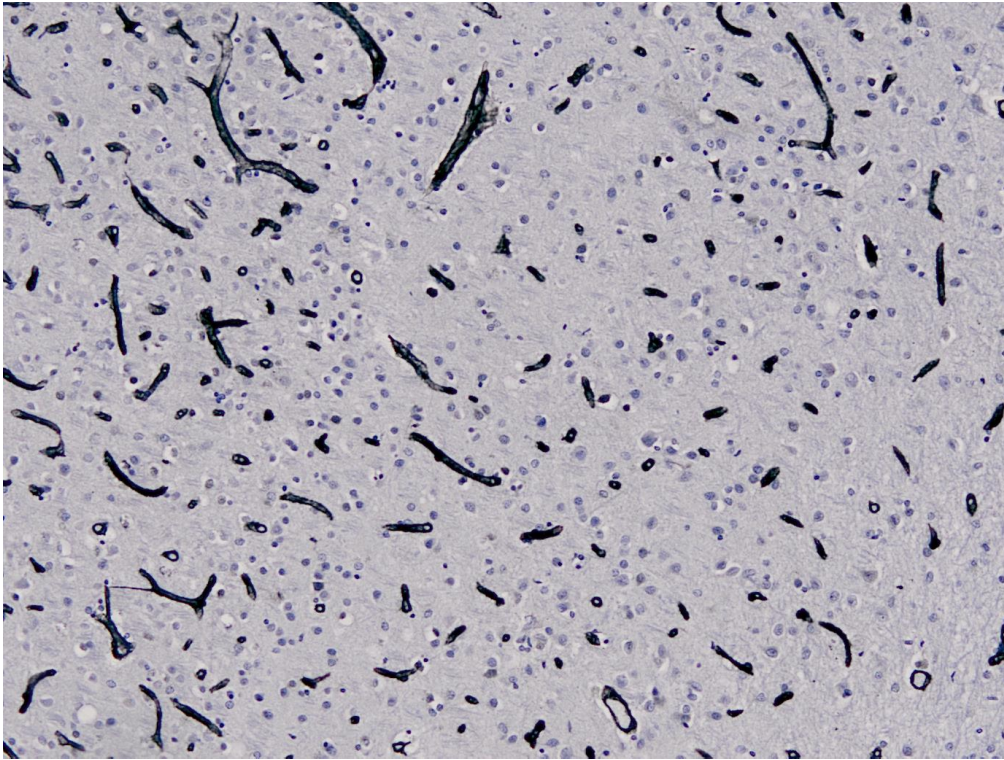


Figure A-4. Human tissue image of AD subject 4

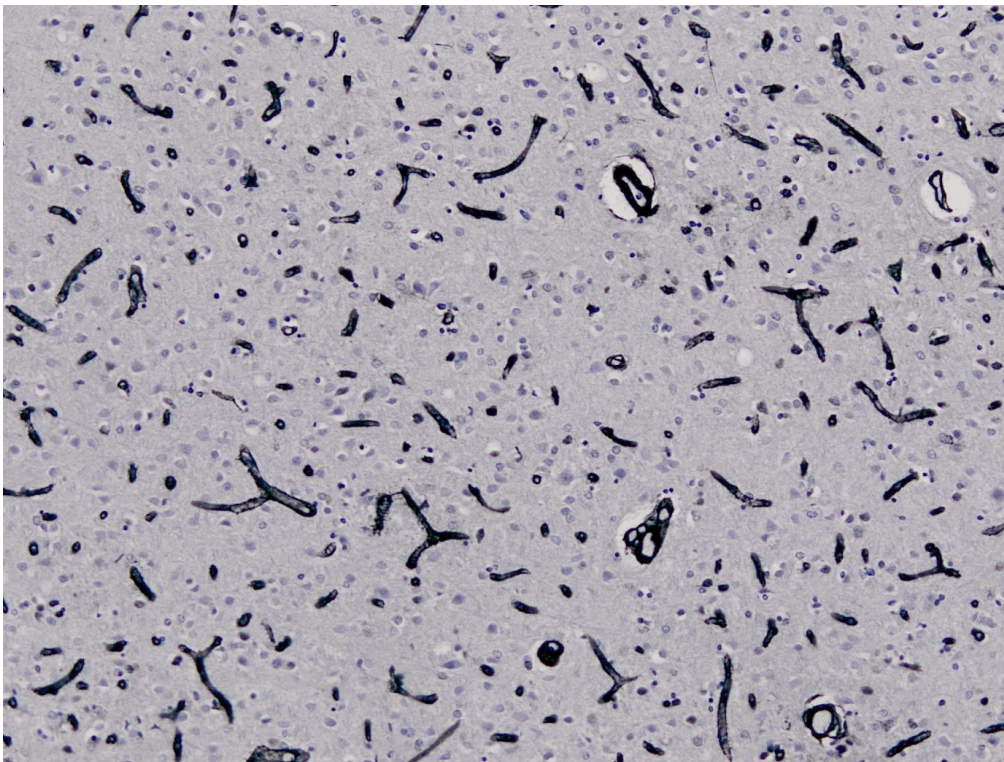


Figure A-5. Human tissue image of AD subject 5



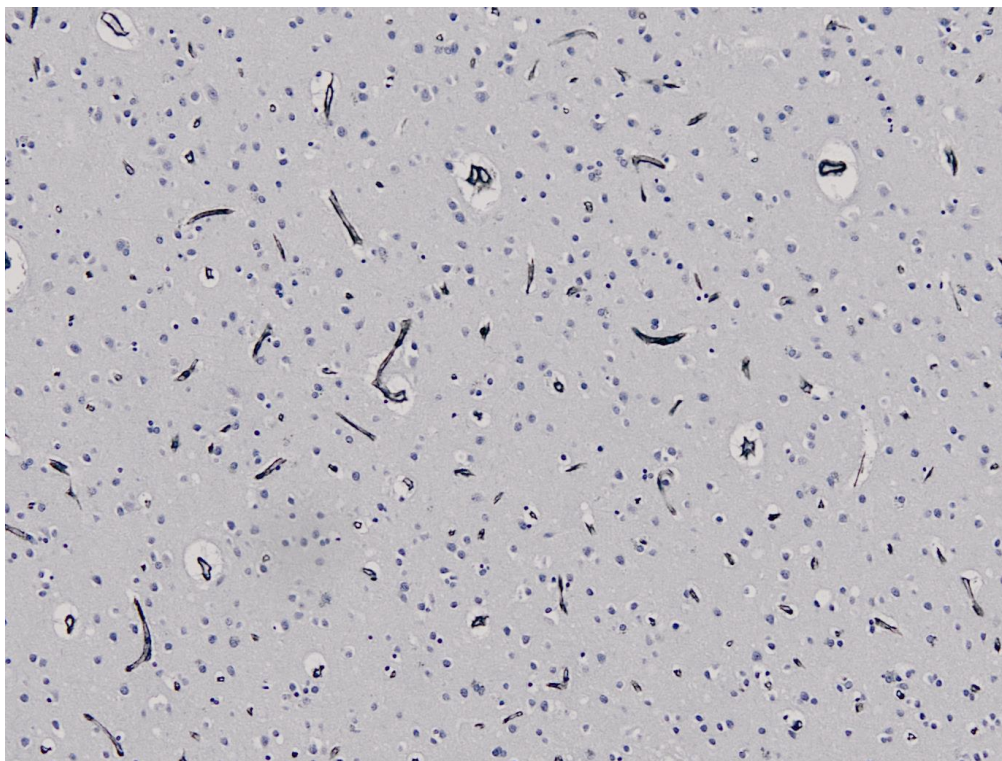


Figure A-6. Human tissue image of Old subject 1

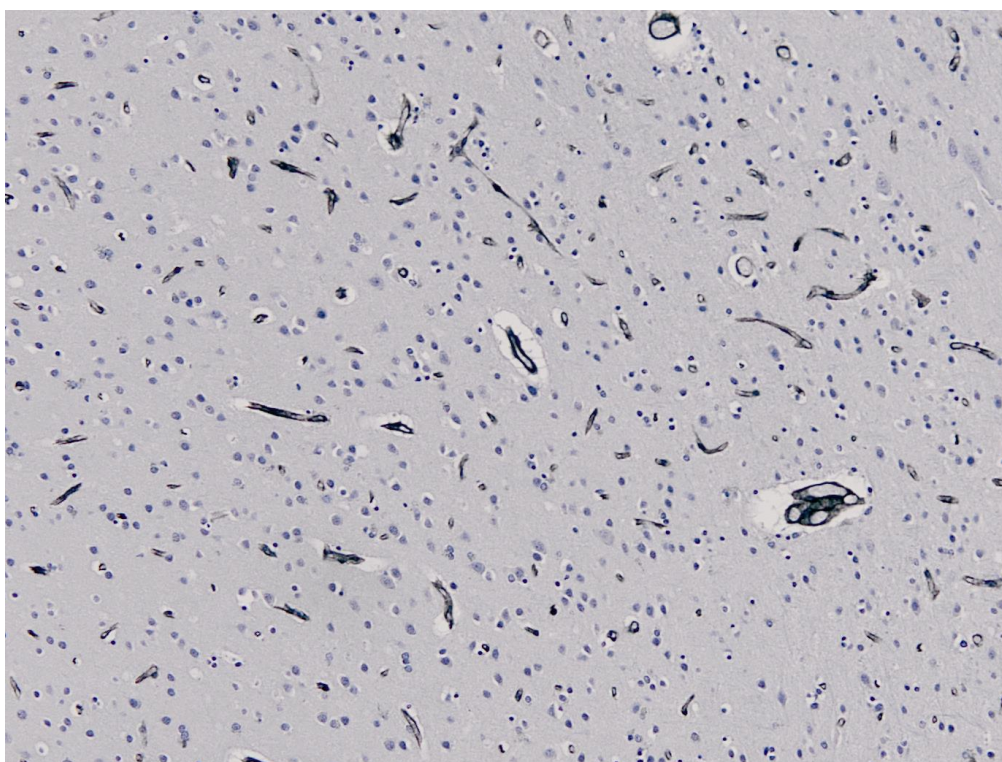


Figure A-7. Human tissue image of Old subject 2



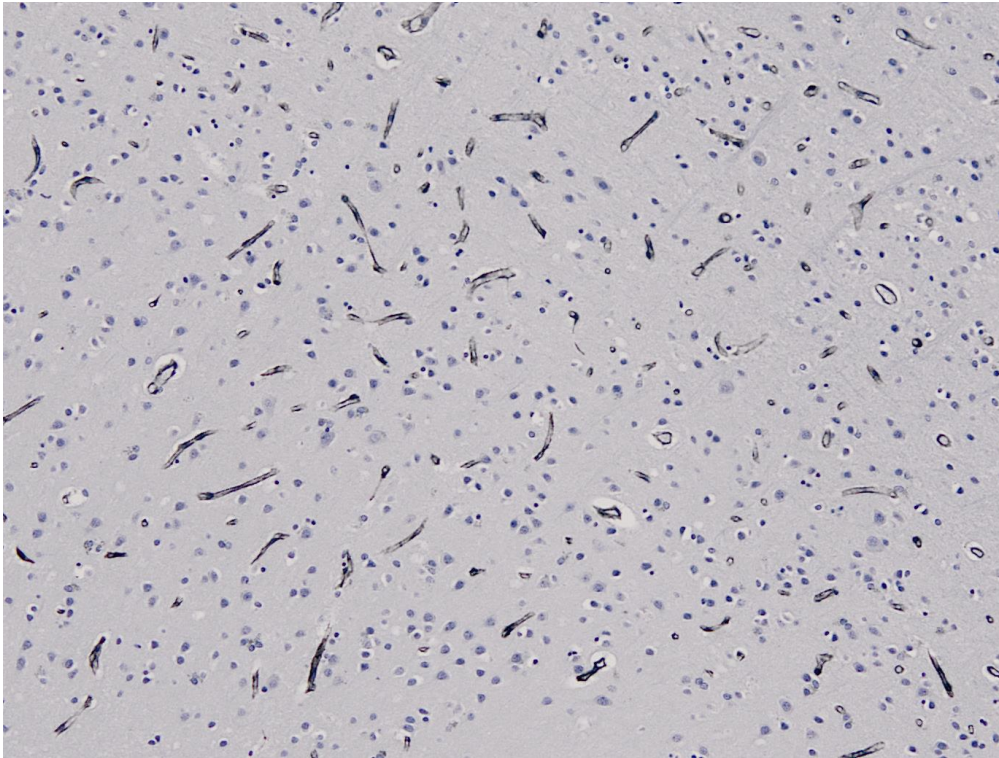


Figure A-8. Human tissue image of Old subject 3

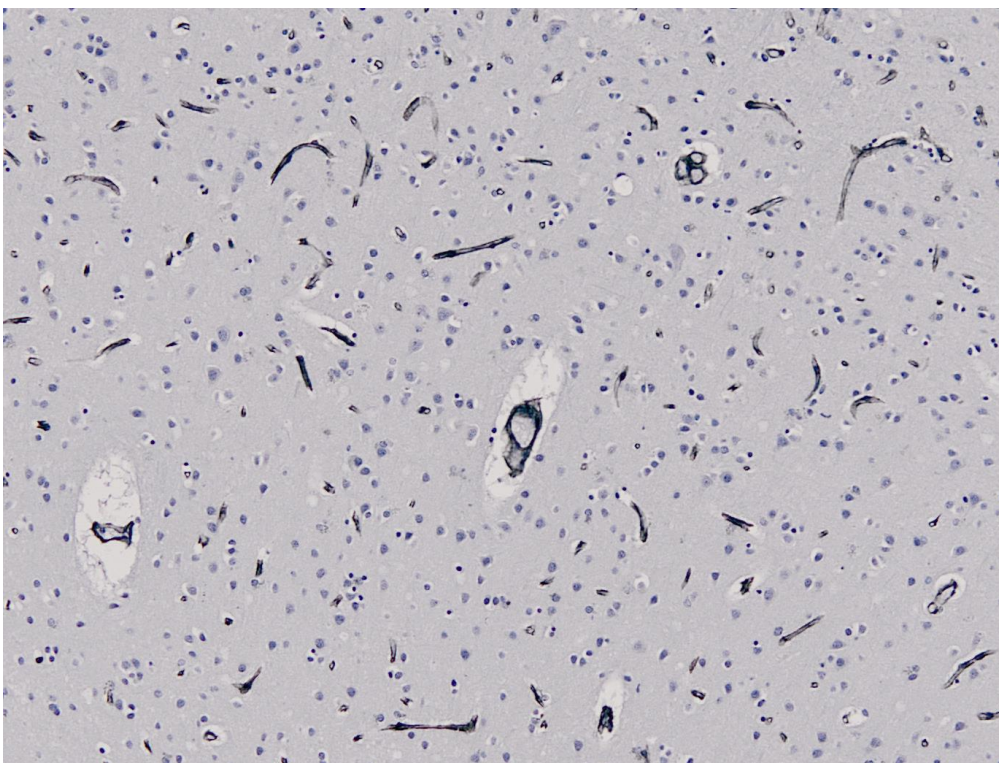


Figure A-9. Human tissue image of Old subject 4

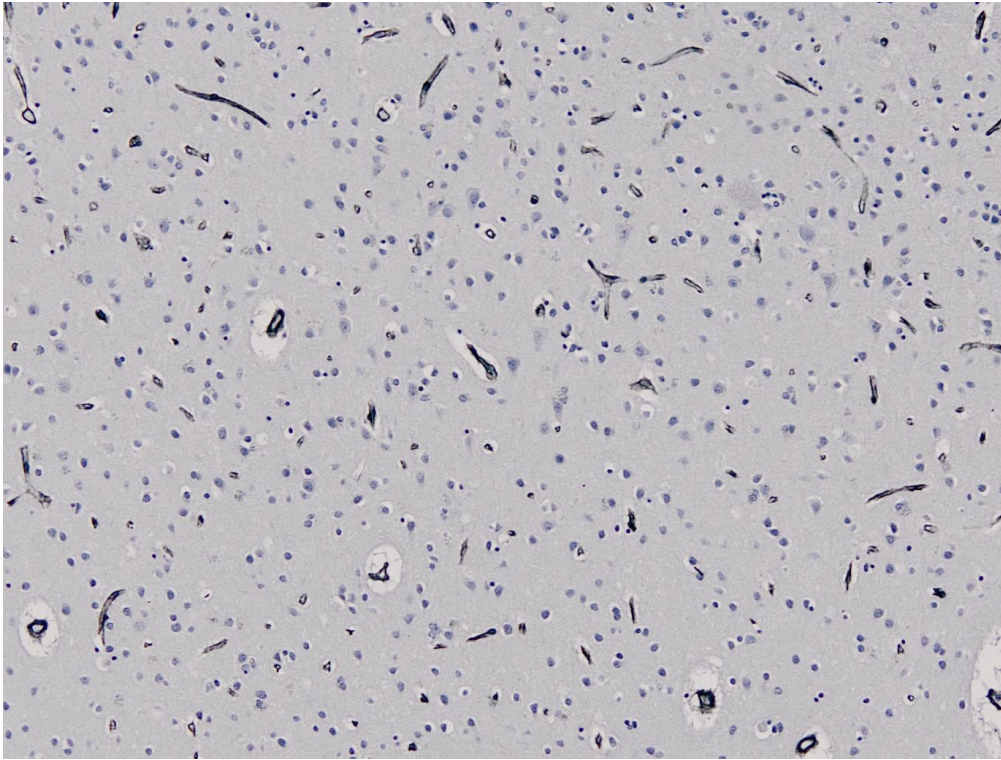


Figure A-10. Human tissue image of Old subject 5



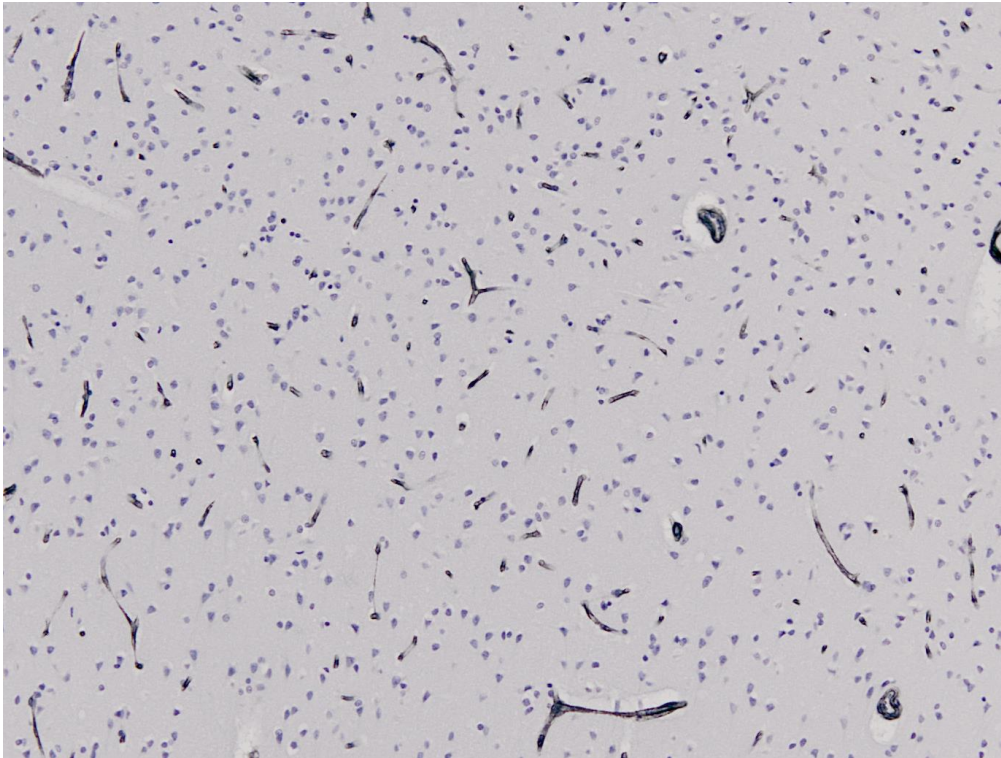


Figure A-11. Human tissue image of Young subject 1

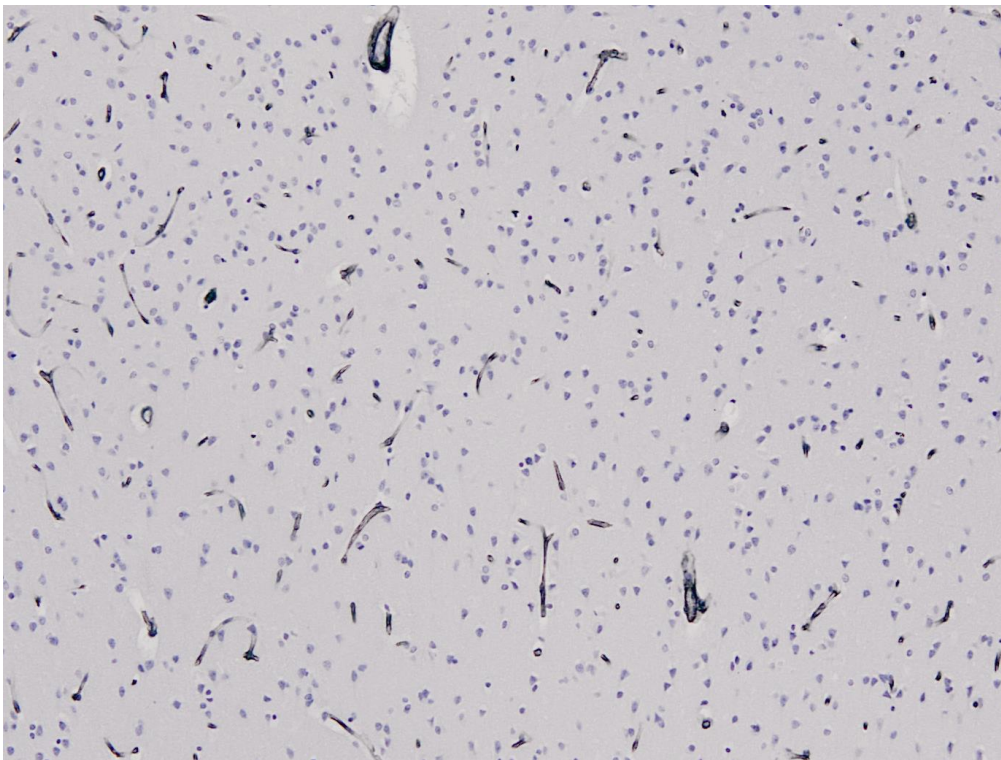


Figure A-12. Human tissue of Young subject 3

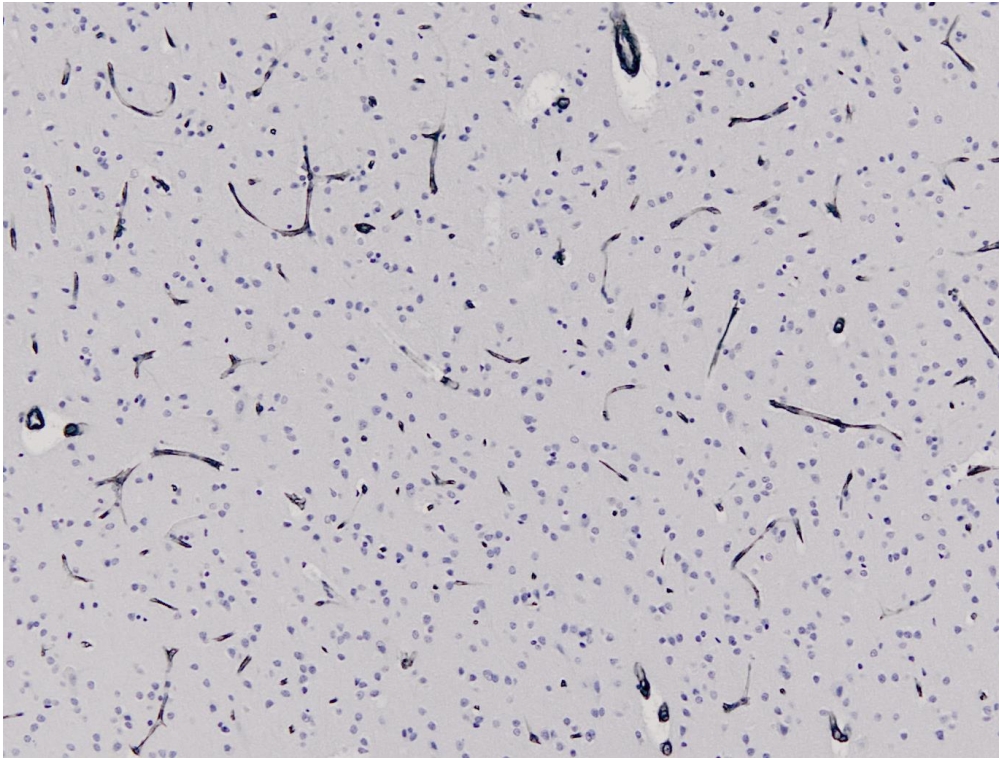


Figure A-13. Human tissue image of Young subject 4

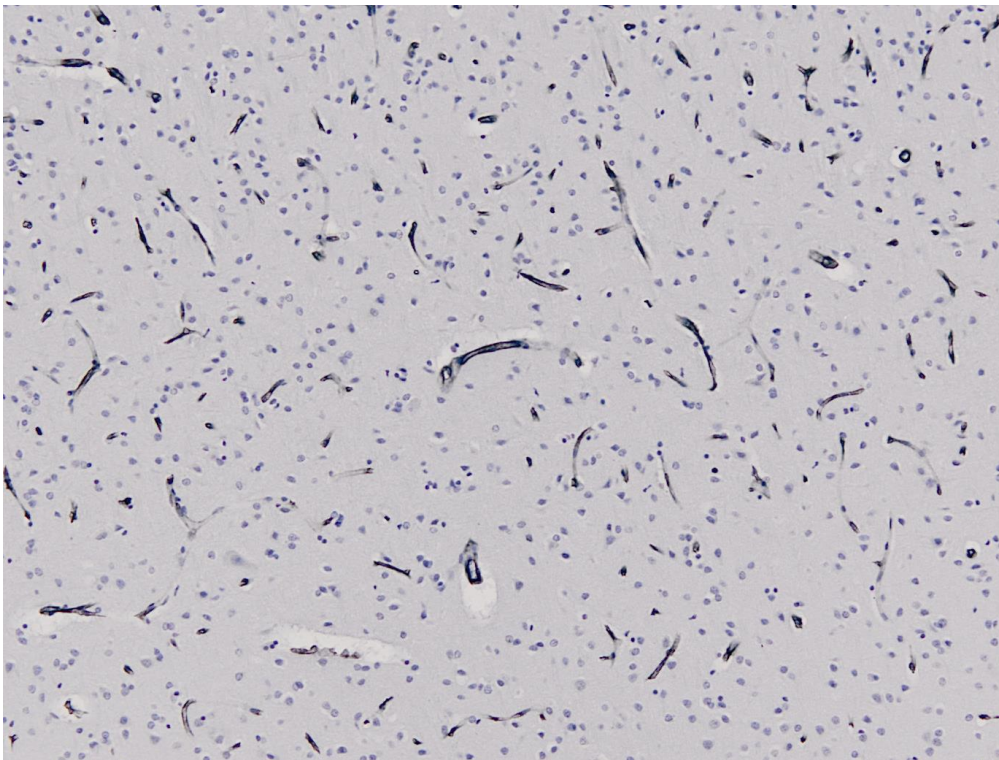


Figure A-14. Human tissue image of Young subject 5



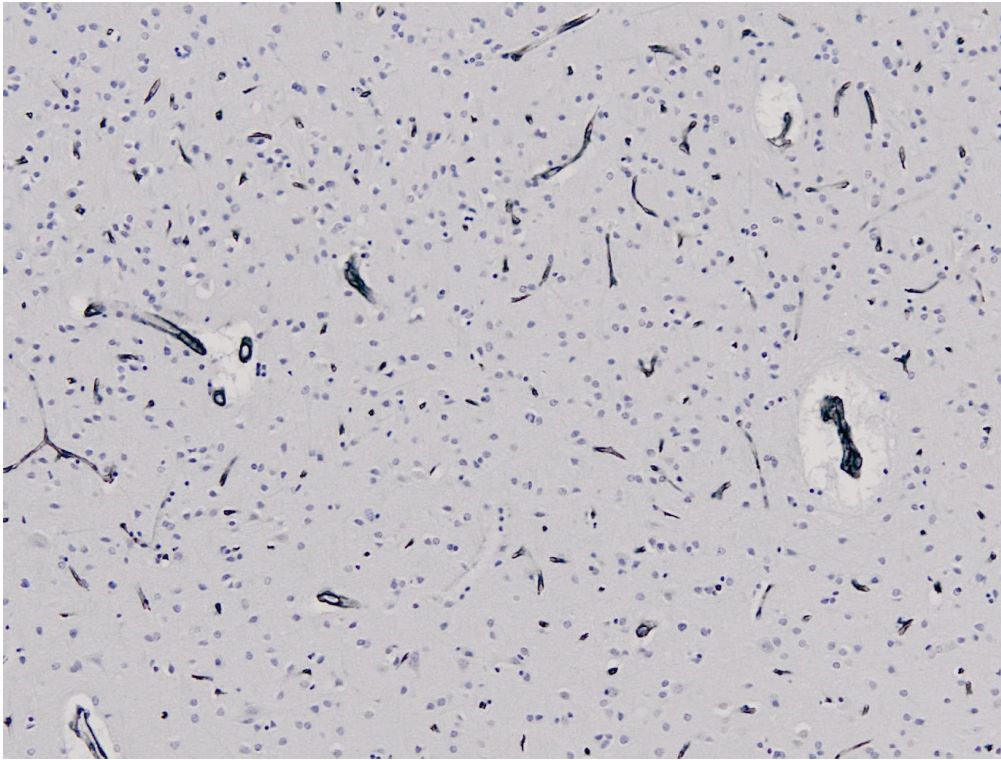


Figure A-15. Human tissue of Young subject 5

## Appendix B

### MRI montage images

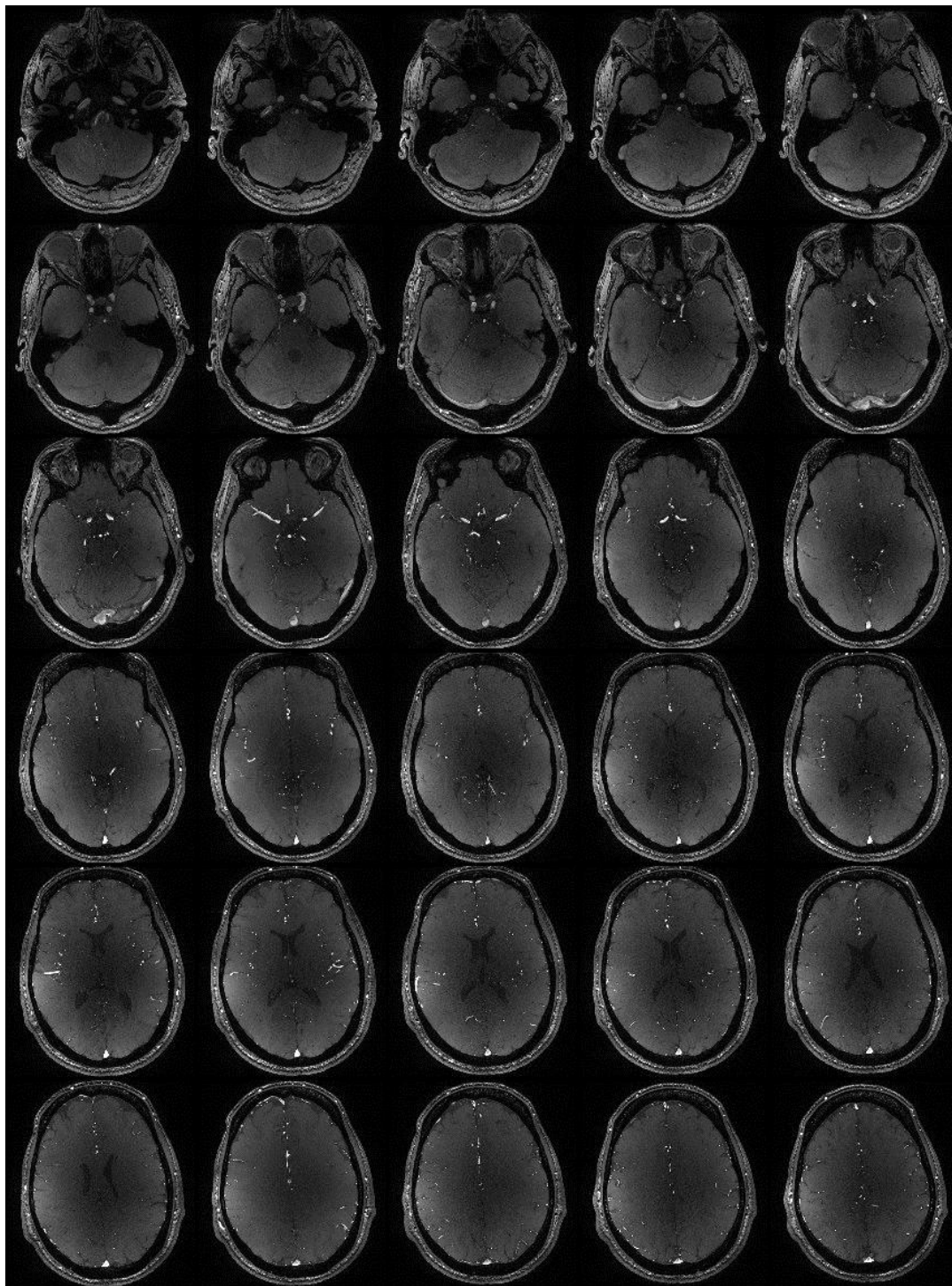


Figure B-1. MRI montage image of normal subject 1

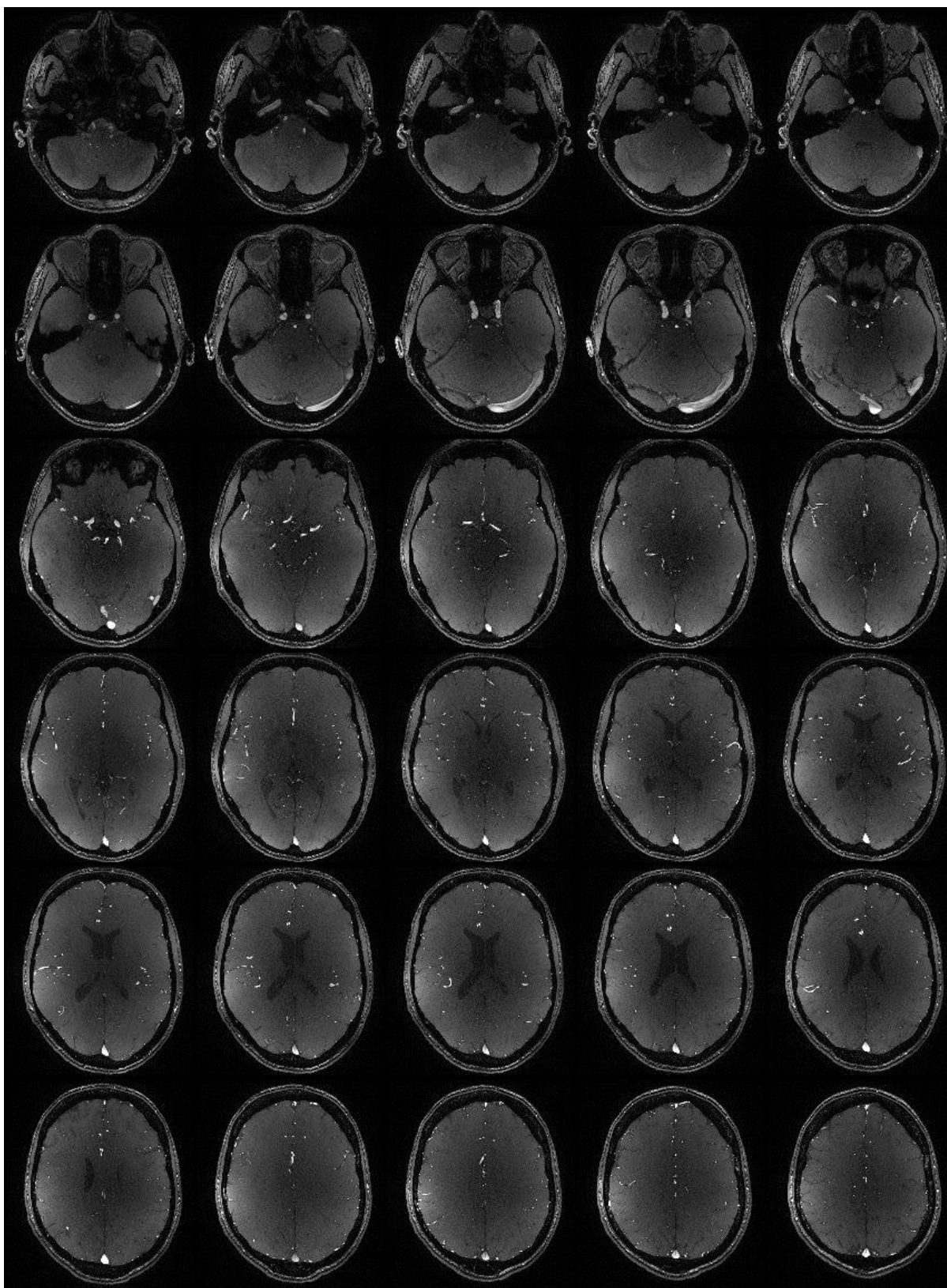


Figure B-2. MRI montage image of normal subject 2



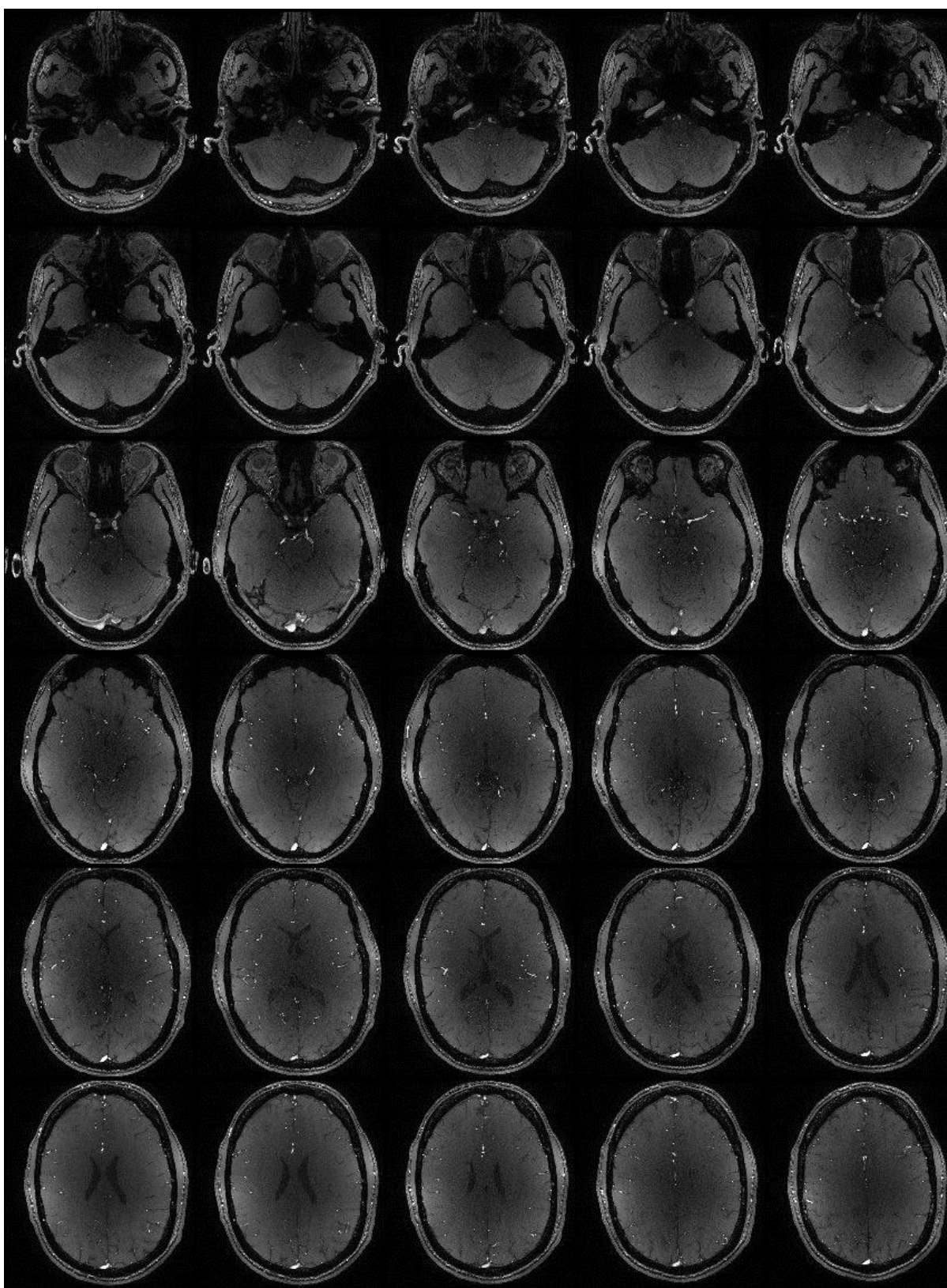


Figure B-3. MRI montage image of normal subject 3



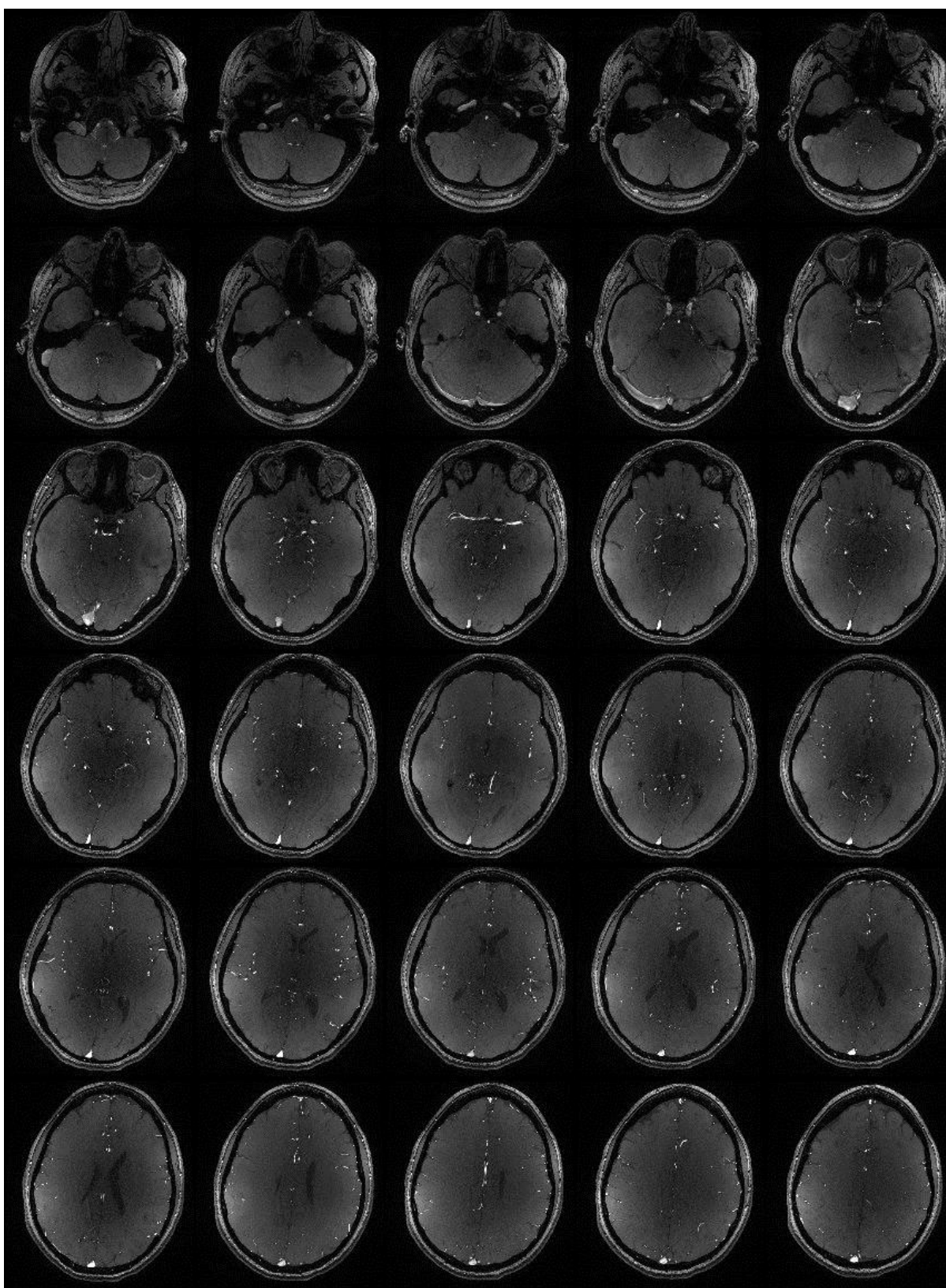


Figure B-4. MRI montage image of normal subject 4

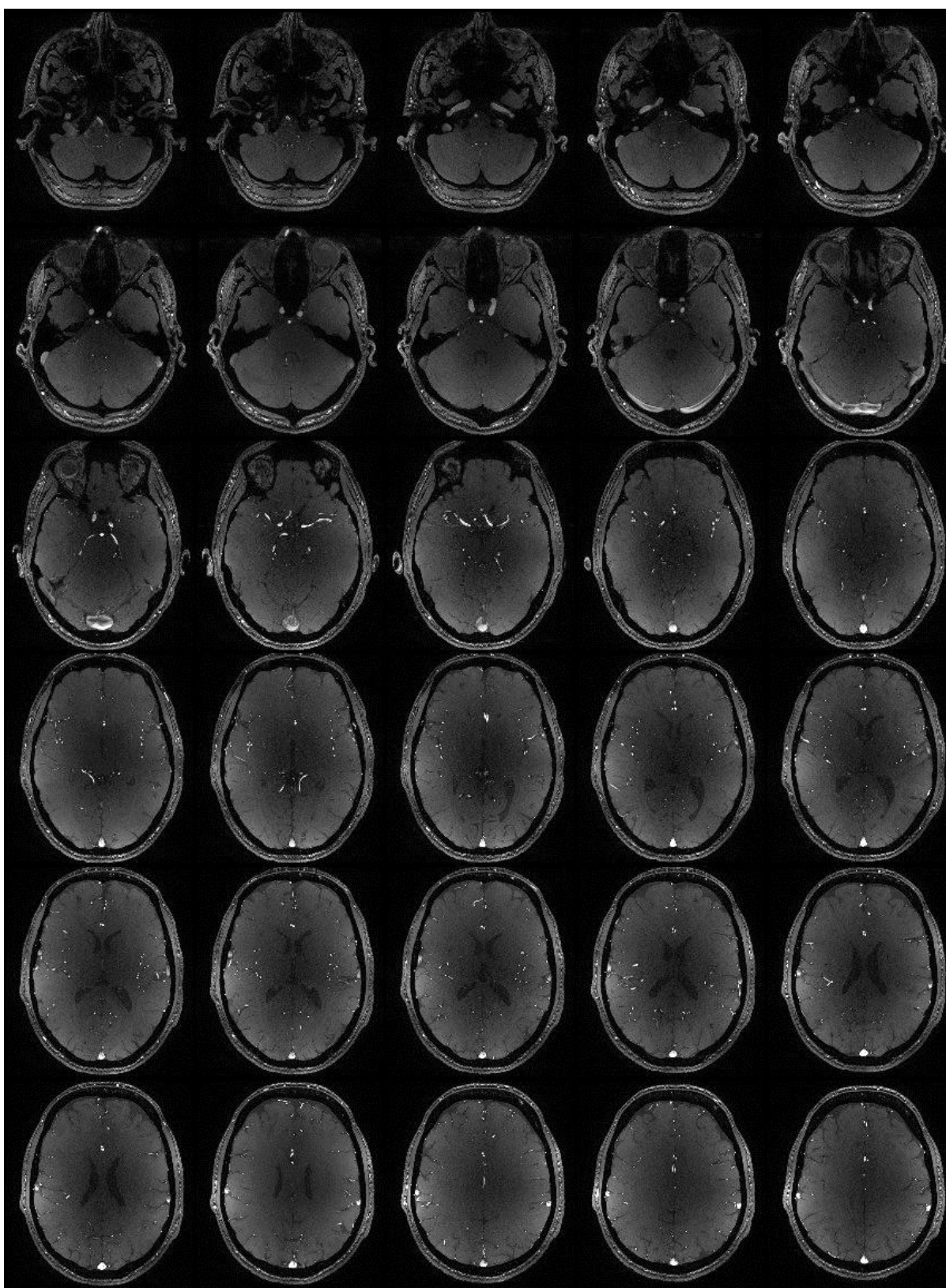


Figure B-5. MRI montage image of normal subject 5

## References

- [1] C. R. Thore, J. A. Anstrom, D. M. Moody, V. R. Challa, M. C. Marion, and W. R. Brown, "Morphometric analysis of arteriolar tortuosity in human cerebral white matter of preterm, young, and aged subjects," *J Neuropathol Exp Neurol*, vol. 66, no. 5, pp. 337-45, May, 2007.
- [2] W. R. Brown, and C. R. Thore, "Review: cerebral microvascular pathology in ageing and neurodegeneration," *Neuropathol Appl Neurobiol*, vol. 37, no. 1, pp. 56-74, Feb, 2011.
- [3] R. N. Kalaria, "Small vessel disease and Alzheimer's dementia: pathological considerations," *Cerebrovasc Dis*, vol. 13 Suppl 2, pp. 48-52, 2002.
- [4] D. M. Moody, W. R. Brown, V. R. Challa, H. S. Ghazi-Birry, and D. M. Reboussin, "Cerebral microvascular alterations in aging, leukoaraiosis, and Alzheimer's disease," *Ann N Y Acad Sci*, vol. 826, pp. 103-16, Sep 26, 1997.
- [5] E. Boscolo, M. Folini, B. Nico, C. Grandi, D. Mangieri, V. Longo, R. Scienza, P. Zampieri, M. T. Conconi, and P. P. Parnigotto, "Beta amyloid angiogenic activity in vitro and in vivo," *International journal of molecular medicine*, vol. 19, no. 4, pp. 581, 2007.
- [6] C. Lemere, J. Blusztajn, H. Yamaguchi, T. Wisniewski, T. Saido, and D. Selkoe, "Sequence of deposition of heterogeneous amyloid beta-peptides and APO E in Down syndrome: implications for initial events in amyloid plaque formation," *Neurobiology of disease*, vol. 3, no. 1, pp. 16, 1996.
- [7] K. G. Mawuenyega, W. Sigurdson, V. Ovod, L. Munsell, T. Kasten, J. C. Morris, K. E. Yarasheski, and R. J. Bateman, "Decreased clearance of CNS  $\beta$ -amyloid in Alzheimer's disease," *Science*, vol. 330, no. 6012, pp. 1774-1774, 2010.
- [8] R. O. Weller, M. Subash, S. D. Preston, I. Mazanti, and R. O. Carare, "Perivascular drainage of amyloid-beta peptides from the brain and its failure in cerebral amyloid angiopathy and Alzheimer's disease," *Brain Pathol*, vol. 18, no. 2, pp. 253-66, Apr, 2008.
- [9] L. Wang, F. Beg, T. Ratnanather, C. Ceritoglu, L. Younes, J. C. Morris, J. G. Csernansky, and M. I. Miller, "Large deformation diffeomorphism and momentum based hippocampal shape discrimination in dementia of the Alzheimer type," *IEEE Trans Med Imaging*, vol. 26, no. 4, pp. 462-70, Apr, 2007.
- [10] P. A. Freeborough, and N. C. Fox, "MR image texture analysis applied to the diagnosis and tracking of Alzheimer's disease," *IEEE Trans Med Imaging*, vol. 17, no. 3, pp. 475-9, Jun, 1998.
- [11] B. Fischl, and A. M. Dale, "Measuring the thickness of the human cerebral cortex from magnetic resonance images," *Proc Natl Acad Sci U S A*, vol. 97, no. 20, pp. 11050-5, Sep 26, 2000.

- [12] G. McKhann, "Clinical diagnosis of Alzheimer's disease : report of the NINCDS-ADRDA Work Group under auspices of Department of Health and Human Services Task Force on Alzheimer's disease," *Neurology*, vol. 34, pp. 939-944, 1984, 1984.
- [13] G. W. Small, P. V. Rabins, P. P. Barry, N. S. Buckholtz, S. T. DeKosky, S. H. Ferris, S. I. Finkel, L. P. Gwyther, Z. S. Khachaturian, B. D. Lebowitz, T. D. McRae, J. C. Morris, F. Oakley, L. S. Schneider, J. E. Streim, T. Sunderland, L. A. Teri, and L. E. Tune, "Diagnosis and treatment of Alzheimer disease and related disorders. Consensus statement of the American Association for Geriatric Psychiatry, the Alzheimer's Association, and the American Geriatrics Society," *JAMA*, vol. 278, no. 16, pp. 1363-71, Oct 22-29, 1997.
- [14] N. C. Berchtold, and C. W. Cotman, "Evolution in the Conceptualization of Dementia and Alzheimer's Disease: Greco-Roman Period to the 1960s," *Neurobiology of Aging*, vol. 19, no. 3, pp. 173-189, 1998.
- [15] G. G. Glenner, "Alzheimer's disease : initial report of the purification and characterization of a novel cerebrovascular amyloid protein," *Biochem Biophys Res Commun*, vol. 120, pp. 885-890, 1984, 1984.
- [16] R. O. Weller, A. Massey, T. A. Newman, M. Hutchings, Y.-M. Kuo, and A. E. Roher, "Cerebral Amyloid Angiopathy: Amyloid  $\beta$  Accumulates in Putative Interstitial Fluid Drainage Pathways in Alzheimer's Disease," *The American Journal of Pathology*, vol. 153, no. 3, pp. 725-733, 1998.
- [17] T. N. Tombaugh, and N. J. McIntyre, "The mini-mental state examination: a comprehensive review," *J Am Geriatr Soc*, vol. 40, no. 9, pp. 922-35, Sep, 1992.
- [18] G. Waldemar, B. Dubois, M. Emre, J. Georges, I. G. McKeith, M. Rossor, P. Scheltens, P. Tariska, and B. Winblad, "Recommendations for the diagnosis and management of Alzheimer's disease and other disorders associated with dementia: EFNS guideline," *European Journal of Neurology*, vol. 14, no. 1, pp. e1-e26, 2007.
- [19] E. Kapaki, G. P. Paraskevas, I. Zalonis, and C. Zournas, "CSF tau protein and beta-amyloid (1-42) in Alzheimer's disease diagnosis: discrimination from normal ageing and other dementias in the Greek population," *Eur J Neurol*, vol. 10, no. 2, pp. 119-28, Mar, 2003.
- [20] G. De Meyer, F. Shapiro, H. Vanderstichele, E. Vanmechelen, S. Engelborghs, P. P. De Deyn, E. Coart, O. Hansson, L. Minthon, H. Zetterberg, K. Blennow, L. Shaw, and J. Q. Trojanowski, "Diagnosis-independent Alzheimer disease biomarker signature in cognitively normal elderly people," *Arch Neurol*, vol. 67, no. 8, pp. 949-56, Aug, 2010.
- [21] H. Rusinek, S. De Santi, D. Frid, W. H. Tsui, C. Y. Tarshish, A. Convit, and M. J. de Leon, "Regional brain atrophy rate predicts future cognitive decline: 6-year longitudinal MR imaging study of normal aging," *Radiology*, vol. 229, no. 3, pp. 691-6, Dec, 2003.
- [22] M. Mapstone, A. K. Cheema, M. S. Fiandaca, X. Zhong, T. R. Mhyre, L. H. MacArthur, W. J. Hall, S. G. Fisher, D. R. Peterson, J. M. Haley, M. D. Nazar, S. A. Rich, D. J. Berlau, C.

- B. Peltz, M. T. Tan, C. H. Kawas, and H. J. Federoff, "Plasma phospholipids identify antecedent memory impairment in older adults," *Nat Med*, vol. 20, no. 4, pp. 415-418, 04//print, 2014.
- [23] C. Cruchaga, John S. K. Kauwe, O. Harari, Sheng C. Jin, Y. Cai, Celeste M. Karch, Bruno A. Benitez, Amanda T. Jeng, T. Skorupa, D. Carrell, S. Bertelsen, M. Bailey, D. McKean, Joshua M. Shulman, Philip L. De Jager, L. Chibnik, David A. Bennett, Steve E. Arnold, D. Harold, R. Sims, A. Gerrish, J. Williams, Vivianne M. Van Deerlin, Virginia M. Y. Lee, Leslie M. Shaw, John Q. Trojanowski, Jonathan L. Haines, R. Mayeux, Margaret A. Pericak-Vance, Lindsay A. Farrer, Gerard D. Schellenberg, Elaine R. Peskind, D. Galasko, Anne M. Fagan, David M. Holtzman, John C. Morris, and Alison M. Goate, "GWAS of Cerebrospinal Fluid Tau Levels Identifies Risk Variants for Alzheimer's Disease," *Neuron*, vol. 78, no. 2, pp. 256-268, 4/24/, 2013.
- [24] K. Blennow, H. Hampel, M. Weiner, and H. Zetterberg, "Cerebrospinal fluid and plasma biomarkers in Alzheimer disease," *Nat Rev Neurol*, vol. 6, no. 3, pp. 131-44, Mar, 2010.
- [25] F. Hassainia, D. Petit, S. Gauthier, and J. Montplaisir, "Topographical study of the heterogeneity of impairments in early Alzheimer's disease patients." pp. 1009-1010 vol.2.
- [26] L. L. Hause, K. C. Ho, and J. Dellis, "Microscopic image analysis in a diagnostic system for Alzheimer's disease." pp. 345-346 vol.2.
- [27] G. T. Bartoo, "Morphological image analysis for studying Alzheimer's disease." pp. 370-371 vol.1.
- [28] X. Zhi-Wen, G. Xiao-Xin, H. Xiao-Ying, and C. Xu, "The blood vessel recognition of ocular fundus." pp. 4493-4498 Vol. 7.
- [29] C. K. Kang, C. A. Park, K. N. Kim, S. M. Hong, C. W. Park, Y. B. Kim, and Z. H. Cho, "Non-invasive visualization of basilar artery perforators with 7T MR angiography," *Journal of Magnetic Resonance Imaging*, vol. 32, no. 3, pp. 544-550, 2010.
- [30] A. Charidimou, Z. Jaunmuktane, J.-C. Baron, M. Burnell, P. Varlet, A. Peeters, J. Xuereb, R. Jäger, S. Brandner, and D. J. Werring, "White matter perivascular spaces An MRI marker in pathology-proven cerebral amyloid angiopathy?," *Neurology*, vol. 82, no. 1, pp. 57-62, 2014.
- [31] R. Hurford, A. Charidimou, Z. Fox, L. Cipolotti, R. Jager, and D. J. Werring, "MRI-visible perivascular spaces: relationship to cognition and small vessel disease MRI markers in ischaemic stroke and TIA," *J Neurol Neurosurg Psychiatry*, vol. 85, no. 5, pp. 522-5, May, 2014.
- [32] N. C. Fox, P. A. Freeborough, and M. N. Rossor, "Visualisation and quantification of rates of atrophy in Alzheimer's disease," *Lancet*, vol. 348, no. 9020, pp. 94-7, Jul 13, 1996.

- [33] J. Attems, "Sporadic cerebral amyloid angiopathy: pathology, clinical implications, and possible pathomechanisms," *Acta Neuropathol*, vol. 110, no. 4, pp. 345-59, Oct, 2005.
- [34] J. Rosand, A. Muzikansky, A. Kumar, J. J. Wisco, E. E. Smith, R. A. Betensky, and S. M. Greenberg, "Spatial clustering of hemorrhages in probable cerebral amyloid angiopathy," *Ann Neurol*, vol. 58, no. 3, pp. 459-62, Sep, 2005.
- [35] M. N. Rossor, N. C. Fox, C. J. Mummery, J. M. Schott, and J. D. Warren, "The diagnosis of young-onset dementia," *Lancet Neurol*, vol. 9, no. 8, pp. 793-806, Aug, 2010.
- [36] S. B. Wesolkowski, "Color image edge detection and segmentation: a comparison of the vector angle and the euclidean distance color similarity measures," University of Waterloo, 1999.
- [37] M. Nixon, and A. S. Aguado, *Feature Extraction & Image Processing for Computer Vision*: Academic Press, 2012.
- [38] R. O. Duda, and P. E. Hart, *Pattern classification and scene analysis*: Wiley New York, 1973.
- [39] R. C. Gonzalez, R. E. Woods, and S. L. Eddins, *Digital image processing using MATLAB*: Gatesmark Publishing Tennessee, 2009.
- [40] F. Y. Shih, *Image processing and pattern recognition: fundamentals and techniques*: John Wiley & Sons, 2010.
- [41] X. Chen, X. Zhou, and S. T. Wong, "Automated segmentation, classification, and tracking of cancer cell nuclei in time-lapse microscopy," *Biomedical Engineering, IEEE Transactions on*, vol. 53, no. 4, pp. 762-766, 2006.
- [42] D. I. Broadhurst, and D. B. Kell, "Statistical strategies for avoiding false discoveries in metabolomics and related experiments," *Metabolomics*, vol. 2, no. 4, pp. 171-196, 2006.
- [43] I. B. M. Corp, "IBM SPSS Statistics for Windows, Version 22.0," IBM Corp, 2013.
- [44] H. Liu, J. Li, and L. Wong, "A comparative study on feature selection and classification methods using gene expression profiles and proteomic patterns," *Genome informatics*, vol. 13, pp. 51-60, 2002.
- [45] G. Chen, T. G. Gharib, C.-C. Huang, D. G. Thomas, K. A. Shedden, J. M. Taylor, S. L. Kardia, D. E. Misek, T. J. Giordano, and M. D. Iannettoni, "Proteomic analysis of lung adenocarcinoma identification of a highly expressed set of proteins in tumors," *Clinical Cancer Research*, vol. 8, no. 7, pp. 2298-2305, 2002.
- [46] K. J. Johnson, and R. E. Synovec, "Pattern recognition of jet fuels: comprehensive GCx GC with ANOVA-based feature selection and principal component analysis," *Chemometrics and Intelligent Laboratory Systems*, vol. 60, no. 1, pp. 225-237, 2002.
- [47] K. M. Pierce, J. L. Hope, K. J. Johnson, B. W. Wright, and R. E. Synovec, "Classification of gasoline data obtained by gas chromatography using a piecewise alignment

- algorithm combined with feature selection and principal component analysis," *Journal of Chromatography A*, vol. 1096, no. 1, pp. 101-110, 2005.
- [48] A. L. Goldberger, L. A. Amaral, J. M. Hausdorff, P. C. Ivanov, C.-K. Peng, and H. E. Stanley, "Fractal dynamics in physiology: alterations with disease and aging," *Proceedings of the National Academy of Sciences*, vol. 99, no. suppl 1, pp. 2466-2472, 2002.
  - [49] G. Kojda, and D. Harrison, "Interactions between NO and reactive oxygen species: pathophysiological importance in atherosclerosis, hypertension, diabetes and heart failure," *Cardiovascular research*, vol. 43, no. 3, pp. 652-671, 1999.
  - [50] P. Baluk, H. Hashizume, and D. M. McDonald, "Cellular abnormalities of blood vessels as targets in cancer," *Current opinion in genetics & development*, vol. 15, no. 1, pp. 102-111, 2005.
  - [51] P. Carmeliet, and R. K. Jain, "Angiogenesis in cancer and other diseases," *nature*, vol. 407, no. 6801, pp. 249-257, 2000.
  - [52] B. V. Zlokovic, "Neurovascular mechanisms of Alzheimer's neurodegeneration," *Trends in neurosciences*, vol. 28, no. 4, pp. 202-208, 2005.
  - [53] C. A. Hawkes, M. Gatherer, M. M. Sharp, A. Dorr, H. M. Yuen, R. Kalaria, R. O. Weller, and R. O. Carare, "Regional differences in the morphological and functional effects of aging on cerebral basement membranes and perivascular drainage of amyloid-beta from the mouse brain," *Aging Cell*, vol. 12, no. 2, pp. 224-36, Apr, 2013.
  - [54] A. Kumar, and K. V. Prathyusha, "Personal authentication using hand vein triangulation and knuckle shape," *Image Processing, IEEE Transactions on*, vol. 18, no. 9, pp. 2127-2136, 2009.
  - [55] D. Guidolin, A. Vacca, G. G. Nussdorfer, and D. Ribatti, "A new image analysis method based on topological and fractal parameters to evaluate the angiostatic activity of docetaxel by using the Matrigel assay in vitro," *Microvascular research*, vol. 67, no. 2, pp. 117-124, 2004.
  - [56] H. Hashizume, P. Baluk, S. Morikawa, J. W. McLean, G. Thurston, S. Roberge, R. K. Jain, and D. M. McDonald, "Openings between defective endothelial cells explain tumor vessel leakiness," *The American journal of pathology*, vol. 156, no. 4, pp. 1363-1380, 2000.
  - [57] P. Sharma, A. Bansal, S. Mathur, S. Wani, R. Cherian, D. McGregor, A. Higbee, S. Hall, and A. Weston, "The utility of a novel narrow band imaging endoscopy system in patients with Barrett's esophagus," *Gastrointestinal endoscopy*, vol. 64, no. 2, pp. 167-175, 2006.
  - [58] B. Wasan, A. Cerutti, S. Ford, and R. Marsh, "Vascular network changes in the retina with age and hypertension," *Journal of hypertension*, vol. 13, no. 12, pp. 1724-1728, 1995.

- [59] M. F. Kiani, and A. G. Hudetz, "Computer simulation of growth of anastomosing microvascular networks," *Journal of theoretical biology*, vol. 150, no. 4, pp. 547-560, 1991.
- [60] E. Bullitt, D. Zeng, G. Gerig, S. Aylward, S. Joshi, J. K. Smith, W. Lin, and M. G. Ewend, "Vessel tortuosity and brain tumor malignancy: a blinded study1," *Academic radiology*, vol. 12, no. 10, pp. 1232-1240, 2005.
- [61] G. aël Chetelat, and J.-C. Baron, "Early diagnosis of Alzheimer's disease: contribution of structural neuroimaging," *Neuroimage*, vol. 18, no. 2, pp. 525-541, 2003.
- [62] P. J. Nestor, P. Scheltens, and J. R. Hodges, "Advances in the early detection of Alzheimer's disease," 2004.
- [63] D. Calvo, M. Ortega, M. G. Penedo, and J. Rouco, "Automatic detection and characterisation of retinal vessel tree bifurcations and crossovers in eye fundus images," *Computer methods and programs in biomedicine*, vol. 103, no. 1, pp. 28-38, 2011.
- [64] T. Lindeberg, *Scale-Space*: Wiley Online Library.
- [65] C. G. Owen, R. S. B. Newsom, A. R. Rudnicka, S. A. Barman, E. G. Woodward, and T. J. Ellis, "Diabetes and the Tortuosity of Vessels of the Bulbar Conjunctiva," *Ophthalmology*, vol. 115, no. 6, pp. e27-e32, 2008.
- [66] J. Kylstra, T. Wierzbicki, M. Wolbarsht, M. Landers, and E. Stefansson, "The relationship between retinal vessel tortuosity, diameter, and transmural pressure," *Graefe's Archive for Clinical and Experimental Ophthalmology*, vol. 224, no. 5, pp. 477-480, 1986.
- [67] W. Lotmar, A. Freiburghaus, and D. Bracher, "Measurement of vessel tortuosity on fundus photographs," *Graefe's Archive for Clinical and Experimental Ophthalmology*, vol. 211, no. 1, pp. 49-57, 1979.
- [68] M. Mächler, "Very smooth nonparametric curve estimation by penalizing change of curvature," 1993.
- [69] Ö. Smedby, N. Högman, S. Nilsson, U. Erikson, A. Olsson, and G. Walldius, "Two-dimensional tortuosity of the superficial femoral artery in early atherosclerosis," *Journal of vascular research*, vol. 30, no. 4, pp. 181-191, 2008.
- [70] I. T. Young, J. E. Walker, and J. E. Bowie, "An analysis technique for biological shape. I," *Information and control*, vol. 25, no. 4, pp. 357-370, 1974.
- [71] A. G. Ghuneim. "Moore-Neighbor Tracing " 1 Nov, 2015; [http://www.imageprocessingplace.com/downloads\\_V3/root\\_downloads/tutorials/contour\\_tracing\\_Abeer\\_George\\_Ghuneim/moore.html](http://www.imageprocessingplace.com/downloads_V3/root_downloads/tutorials/contour_tracing_Abeer_George_Ghuneim/moore.html).
- [72] S.-C. B. Lo, L.-Y. Hsu, M. T. Freedman, Y. M. F. Lure, and H. Zhao, "Classification of lung nodules in diagnostic CT: an approach based on 3D vascular features, nodule density distribution, and shape features." pp. 183-189.



- [73] D. Vukadinovic, T. van Walsum, R. Manniesing, S. Rozie, R. Hameeteman, T. T. De Weert, A. Van der Lugt, and W. J. Niessen, "Segmentation of the outer vessel wall of the common carotid artery in CTA," *Medical Imaging, IEEE Transactions on*, vol. 29, no. 1, pp. 65-76, 2010.
- [74] E. Bribiesca, "An easy measure of compactness for 2D and 3D shapes," *Pattern Recognition*, vol. 41, no. 2, pp. 543-554, 2008.
- [75] C. T. Zahn, and R. Z. Roskies, "Fourier descriptors for plane closed curves," *Computers, IEEE Transactions on*, vol. 100, no. 3, pp. 269-281, 1972.
- [76] G. G. Geary, and J. N. Buchholz, "Selected contribution: effects of aging on cerebrovascular tone and  $[Ca^{2+}]_i$ ," *Journal of Applied Physiology*, vol. 95, no. 4, pp. 1746-1754, 2003.
- [77] G. Keppel, *Design and analysis: A researcher's handbook*, 4th Edition: Prentice-Hall, Inc, 2004.
- [78] N. J. Salkind, *Encyclopedia of research design*: Sage, 2010.
- [79] A. Keable, K. Fenna, H. M. Yuen, D. A. Johnston, N. R. Smyth, C. Smith, R. A.-S. Salman, N. Samarasekera, J. A. Nicoll, and J. Attems, "Deposition of amyloid  $\beta$  in the walls of human leptomeningeal arteries in relation to perivascular drainage pathways in cerebral amyloid angiopathy," *Biochimica et Biophysica Acta (BBA)-Molecular Basis of Disease*, 2015.
- [80] E. I. Altman, "Financial ratios, discriminant analysis and the prediction of corporate bankruptcy," *The journal of finance*, vol. 23, no. 4, pp. 589-609, 1968.
- [81] S. S. Berr, N. S. Hurt, C. R. Ayers, J. W. Snell, and M. B. Merickel, "Assessment of the reliability of the determination of carotid artery lumen sizes by quantitative image processing of magnetic resonance angiograms and images," *Magnetic resonance imaging*, vol. 13, no. 6, pp. 827-835, 1995.
- [82] K. Jellinger, "Alzheimer disease and cerebrovascular pathology: an update," *Journal of neural transmission*, vol. 109, no. 5-6, pp. 813-836, 2002.
- [83] D. R. Thal, E. Capetillo-Zarate, S. Larionov, M. Staufenbiel, S. Zurbuegg, and N. Beckmann, "Capillary cerebral amyloid angiopathy is associated with vessel occlusion and cerebral blood flow disturbances," *Neurobiology of aging*, vol. 30, no. 12, pp. 1936-1948, 2009.
- [84] D. Lesage, E. D. Angelini, I. Bloch, and G. Funka-Lea, "A review of 3D vessel lumen segmentation techniques: Models, features and extraction schemes," *Medical image analysis*, vol. 13, no. 6, pp. 819-845, 2009.
- [85] S. Wörz, and K. Rohr, "Segmentation and quantification of human vessels using a 3-D cylindrical intensity model," *Image Processing, IEEE Transactions on*, vol. 16, no. 8, pp. 1994-2004, 2007.

- [86] A. F. Frangi, W. J. Niessen, K. L. Vincken, and M. A. Viergever, "Multiscale vessel enhancement filtering," *Medical Image Computing and Computer-Assisted Intervention—MICCAI'98*, pp. 130-137: Springer, 1998.
- [87] Y. Sato, S. Nakajima, N. Shiraga, H. Atsumi, S. Yoshida, T. Koller, G. Gerig, and R. Kikinis, "Three-dimensional multi-scale line filter for segmentation and visualization of curvilinear structures in medical images," *Medical image analysis*, vol. 2, no. 2, pp. 143-168, 1998.
- [88] T. M. Koller, G. Gerig, G. Szekely, and D. Dettwiler, "Multiscale detection of curvilinear structures in 2-D and 3-D image data." pp. 864-869.
- [89] K. Krissian, G. Malandain, N. Ayache, R. Vaillant, and Y. Troussset, "Model-based detection of tubular structures in 3D images," *Computer vision and image understanding*, vol. 80, no. 2, pp. 130-171, 2000.
- [90] S. R. Aylward, and E. Bullitt, "Initialization, noise, singularities, and scale in height ridge traversal for tubular object centerline extraction," *Medical Imaging, IEEE Transactions on*, vol. 21, no. 2, pp. 61-75, 2002.
- [91] R. Manniesing, M. A. Viergever, and W. J. Niessen, "Vessel enhancing diffusion: A scale space representation of vessel structures," *Medical image analysis*, vol. 10, no. 6, pp. 815-825, 2006.
- [92] E. Alexandratou, D. Yova, and D. Cokkinos, "Morphometric characteristics of red blood cells as diagnostic factors for coronary artery disease," *Clinical hemorheology and microcirculation*, vol. 21, no. 3-4, pp. 383-388, 1998.
- [93] A. Jain, and D. Zongker, "Feature selection: Evaluation, application, and small sample performance," *Pattern Analysis and Machine Intelligence, IEEE Transactions on*, vol. 19, no. 2, pp. 153-158, 1997.